CHEMISTRY & PHOTOCHEMISTRY OF AIRBORNE INDUSTRIAL DUST: HUMAN HEALTH & ENVIRONMENTAL IMPLICATIONS

by

Milton Chandra Das

Submitted in Partial Fulfillment

of the Requirements for the Degree of

Doctor of Philosophy in Chemistry

New Mexico Institute of Mining and Technology
Socorro, New Mexico
February, 2023

This thesis is dedicated to my late father and to my loving family…

Milton Chandra Das
New Mexico Institute of Mining and Technology
February, 2023

ABSTRACT

Industrial dust is one of the major sources of anthropogenic aerosols in the atmosphere, particularly in the vicinity of any manufacturing site. These particles are known to pose a severe risk to the health of nearby residents and workers. Although inhalation is the primary exposure pathway to dust, the amount of dust that gets into their respiratory system depends significantly on the size of the particles. The deep lung regions can be reached by dust particles with an aerodynamic diameter of less than 4 micrometers, although bigger particles may be filtered in the airway and cleared to the gastrointestinal tract (GIT). However, we only know a little about the impact of inhaled dust on human organs and the gut microbiota despite the critical necessity of this knowledge. In this thesis work, we attempted to address this issue by assessing the toxicity of coal and uranium mine dust based on their capacity to leach metals and non-metals into human body fluids.

Uranium mine dust has been identified as one of the major health hazards that can cause cardiovascular and metabolic problems if inhaled. Prior studies have mostly concentrated on what happens to inhaled dust particles (<4 μm) once they reach the lungs. In this study, we investigated the uranium solubility from airborne dust and sediments in two simulated gastrointestinal fluids; Simulated Gastric Fluid (SGF) and Simulated Intestinal Fluid (SIF). For this purpose, samples were collected from nearby two uranium mines in the Grand Mining District (GMD) of New Mexico. As opposed to sediment samples from the St. Anthony Mine, which favored higher solubility in the SGF solution, Jackpile mine dust samples favored higher solubility in the SIF solution. Our results highlighted that mine dust rich in the minerals andersonite, tyuyamunite, and/or autunite exhibits more uranium dissolution in the SIF solution than in the SGF solution. These conclusions were further confirmed by the computational calculations performed using thermodynamic model PHREEQC. Additionally, we examined the influence of kaolinite and microcline since they were present in several collected samples. Kaolinite enhances mineral dissolution in SIF, except for andersonite, as evidenced by the fact that it lowers the ratio of dissolved uranium in SGF to SIF. For all of the investigated uranium minerals, the ratio of dissolved uranium in SGF to SIF drops with the addition of microcline. Based on computational analysis, the most common oxidation state of dissolved uranium was shown to be U(VI). The results of the experimental observations and the geochemical calculations done with PHREEQC are in agreement. As a result, this study sheds light on the mineralogy-controlled toxicological evaluation of inhaled dust that contains uranium and cleared into the gastrointestinal system.

Exposure to respirable coal mine dust (RCMD) poses a health risk to the mining industry that contributes to several health problems, including coal worker pneumoconiosis (CWP). Given the geographic concentration of coal workers' pneumoconiosis (CWP), it was always assumed that RCMD in the Appalachian region is more harmful than RCMD in other areas. The characteristics of RCMD and their connections to dust toxicity based on their geographic location have not yet been investigated. We gathered samples from the Appalachian and Rocky Mountain regions to assess the toxicity based on metal leeching capability in simulated lung fluids (SLFs). Additionally, diverse RCMD sources that could exist inside the same mine can have unique physicochemical characteristics raising the possibility of various health effects that have not been thoroughly researched. In light of

this, we also look into the toxicity of RCMD from several sources, including coal seam, rock dust, host floor, and host roof from Intra and Inter-mines. In order to uncover any trends associated with geographic regions and/or mine-specific sources, this investigation intends to quantify the metal leaching in the lung fluid and correlate that with the in-vitro immune responses. According to our findings, Si and Al are the most dissolved metals along with trace amounts of other metals, including Fe, Sr, Ba, and Pb. However, no patterns were discovered that would suggest a dependence on geographic location. The floor and roof dust dissolved the most metal, whereas the coal seam and rock dust dissolved the least amount of metal. Results from in-vitro tests indicated that floor and roof dust samples significantly impacted cell viability, indicating increased toxicity. The pro-inflammatory response may influence the development of pneumoconiosis and other lung illnesses in epithelial and macrophage cells.

In addition to having an adverse effect on human health, industrial dust can also have impact on our climate. Atmospheric processing of industrial dust can contribute to the bioavailable Fe production that affecting primary productivity. The majority of previous research has been on Fe-containing mineral dust as a source of dissolved Fe to ocean life. Therefore, in the current work, we investigated coal fly ash (CFA) as a source of bioavailable iron. We conducted dissolution tests in low- and high-flux environments using spectroscopic methods such as infra-red, UV-vis, XRD, mass spectroscopy, etc. The nitric acid dissolution experiments were carried out in atmospherically suitable conditions. Further, having the increased CFA distributions in industrialized areas, engineered nanomaterials may be combined with them. Therefore, we investigated the impact of an engineered nanoparticle, titanium dioxide (TiO_2), on the CFA's ability to leach out the iron. We performed tests by mixing CFA with both rutile and anatase crystal phases. Our results reveal that titanium enhances iron mobility from the CFA, regardless of whether titanium is added externally or present naturally in the sample. This research will therefore provide us with crucial, as of yet unexplored, knowledge on CFA as a source of bioavailable iron.

Overall, the current research work reports the mineralogy-controlled impact of industrial dust on environmental processes and human health. The physicochemical properties of these manufactured particles can be linked to their extent of dissolution and, thus, their influence on biological and ecological systems. The results revealed in this thesis work will be used to develop risk assessment models to identify miners who may eventually develop lung illnesses by better comprehending the consequences of inhaled particles, the consequent cellular toxicity, and long-term health effects. Further, the data reported on coal fly ash mixed with engineered nanoparticles will be used to better understand global iron mobilization and predict biomass production in the ocean.

Keywords: *Uranium toxicity in gastrointestinal tract, mineralogy dependent toxicity of U-dust, respirable coal mine dust toxicity, bioavailable Fe production, atmospheric processing of coal fly ashes, titanium dioxide chemistry, ocean fertilization.*

ACKNOWLEDGMENTS

I want to start by expressing my gratitude to Dr. Gayan Rubasinghege, my academic and research advisor, for accepting me as a graduate student in his group. I'm grateful for all the experiences and learning opportunities that helped me develop into the scientist I am today. His leadership, direction, and the difficulties that pushed me to a level that I am able to complete, have all contributed significantly to my success in graduate school. I appreciate you allowing me to work on multiple projects at once. I also want to express my gratitude for allowing me to work according to my schedules, which allowed me to not only perform fruitful study but also actively participate in our communities. I want to express my sincere gratitude to all the members of my committee, past and present, including Drs. Menake Piyasena, Wenyang Gao, Christian Carrico, Pabitra Choudhury, Pedram Roghanchi, Mahinda Ranasinghe (now at West Virginia State University), Michael Heagy (Rochester Institute of Technology), and retired Dr. Oliver Wingenter, for their support and leadership throughout. I want to express my gratitude to Dr. Pedram Roghanchi individually for allowing me to work on a funded project under his guidance.

Many thanks go to my collaborators. Dr. Jonas Baltrusaitis, I appreciate you giving me the opportunity to collaborate with you on a joint project and for providing the XPS analysis for our samples. I am grateful to Dr. Daniel Cadol from the Earth and Environmental Science department at NMT for providing the uranium dust. Additionally, I want to thank Dr. Richard Reynolds and Mr. Harland Goldstein, our USGS collaborators who provided the coal fly ash samples. I want to thank our collaborator at the Pennsylvania State University Dr. Mohammad Rezaee, and Mr. Mark Hovingh for collecting and providing the coal dust samples. I appreciate Dr. Katherine Zychowski's contribution from the College of Nursing, University of New Mexico, Health Sciences Center for providing the data for the in-vitro analysis for coal dust samples. I appreciate the training on XRD and the knowledge sharing that Dr. Virgil Lueth and Kelsey McNamara provided. I appreciate the New Mexico Bureau of Geology's Ms. Bonnie Frey and Mr. Dustin Baca allowing me to use the ICP-MS, ICP-OES, microwave digestion, and all the supports. Thanks to Dr. Sergei Ivanov at CINT for providing the facility to collect SEM images for our samples.

Many thanks go to my funding agencies without whom none of this research would be possible. The research presented in chapter 3 of this thesis was funded by NIH, grant number P20GM103451, and NM EPSCoR, Award No. IIA-1301346. Research presented in Chapters 4 and 5 of this thesis was funded by the National Institute for Occupational Safety and Health (NIOSH) (contracts #75D30119C06390 & #75D30120R67845). The views, opinions and recommendations expressed herein are solely those of the authors and do not necessarily reflect the views of NIOSH. Mention of trade names, commercial products or organizations does not imply endorsement by the authors nor the funding organization.

Thanks to all the past and present Environmental and Analytical Chemistry Research Group members. My sincere gratitude goes out to Dr. Eshani Hettiarachchi, Dr. Nishanti Ellepola, Dr. Amadini Jayasinghe, Mr. Rifat Khan, Ms. Malsha Indeewari, Mr. Jason Leboeuf, and Ms. Jordyn Wemhoner for all the help you provided me on different

days. Additionally, I want to express my gratitude to Mr. Amrutdyuti Swamy, Dr. Shahriare Hossain, and Dr. Gayatri P. Gautam for their friendship and valuable support.

Thanks to all of my family and friends. I want to thank my wife Dipa Das for bearing with me through all of my struggles, absences, and irrational outbursts. She talked about ideas with me, offered me support, and helped me avoid a few bad decisions. She helped the family for a large portion of my graduate studies. My late father, Mr. Niranjan Chandra Das, who instilled ideals in me and shaped me into a person with a good outlook, has my sincere thanks. Thank you so much, Mom and Sister, for their encouragement and support. Additionally, I want to thank all of my Bangladeshi friends in Socorro, New Mexico, for their love, friendship, and support.

I would also like to thank the Faculty, staff and fellow students of the Department of Chemistry, and New Mexico Tech, for all your support and making my time here, a wonderful and memorable experience. Last but, not least I want to thank New Mexico Tech, specifically, everyone who is working around the clock to make sure our journey is as smooth as possible even in this hard time during COVID 19 pandemic.

.

CONTENTS

LIST OF TABLES

Table Page

LIST OF FIGURES

Figure Page

LIST OF ABBREVIATIONS AND SYMBOLS

AI	Average intake
ALF	Artificial lysosomal fluid
ATCC	American Type Culture Collection
ATR	Attenuated total reflectance
CFA	Coal Fly Ash
CINT	Center for Integrated Nanotechnologies
COPD	Chronic obstructive pulmonary diseases
CWP	Coal workers' pneumoconiosis
CWHSP	Coal Workers' Health Surveillance Program
BET	Brunauer-Emmett-Teller
DDF	Dust-related diffuse fibrosis
DFT	Density functional theory
DMEM	Dulbecco's Modified Eagle's Medium
MMSO	Dimethyl Sulfoxide
EPA	Environmental Protection Agency
FTIR	Fourier transform infra-red
GIT	Gastrointestinal Tract
GMD	Grants Mining District
GS	Gamble solution
HNLC	High nutrient low chlorophyll
ICP-MS	Inductively coupled plasma mass spectrometry
IPA	Isopropyl alcohol
LD_{50}	Lethal Dose to Kill 50% of the Population
N/A	Not available
NIST	National Institute of Standards and Technology
NLDFT	Non-local density functional theory

NMT	New Mexico Tech
PAO	Polyarsine oxide
PBS	Phosphate buffer solution
PEL	Permissible exposure limit
PM	Particulate Mater
PMF	Progressive massive fibrosis
PRP	Pattern recognition receptors
QSDFT	Quenched Solid Density Functional Theory
RCMD	Respirable coal mine dust
RCS	Respirable crystalline silica
RDA	Recommended dietary allowance
S	Surface
SEM	Scanning electron microscopy
SGF	Simulated Gastric Fluid
SGIF	Simulated Gastrointestinal Fluid
SIF	Simulated Intestinal Fluid
SLF	Simulated lung fluid
SRM	Standard Reference Material
TDU	Total dissolved uranium concentration
UV/VIS	Ultra Violet/ Visible Spectroscopy
UG	Underground
UL	Tolerable upper intake levels
USGS	United states geological society
XPS	X-ray photoelectron spectroscopy
XRD	X-ray diffraction

- For all the elements, their standard chemical symbols have used
- For all the chemicals and minerals, their standard formulas have used
- All units used have their standard meaning unless otherwise mentioned

The dissertation is accepted on behalf of the faculty Institute by the following committee:

Gayan Rubasinghege

_____

Academic and Research Advisor

Menake Piyasena

_____

Wenyang Gao

_____

Pabitra Choudhury

_____

Christian Carrico

_____

Pedram Roghanchi

_____

I release this document to the New Mexico Institute of Mining and Technology.

Milton Chandra Das February 10, 2023

_____

CHAPTER 1

INTRODUCTION

Mineral dust is ubiquitous, including in residences, places of business, and the outdoor environment. These particles influence various environmental processes and human health. They also cause expensive concerns with machinery and production methods.[1] Dust is composed of microscopic fragments of solid and dry material. Although dust can be created anywhere, there are three different forms of dust: environmental, residential, and industrial. While there are ways to prevent or reduce household and environmental dust, handling huge industrial dust loads is challenging, has health risks, and can impact the climate.[2-7]

Industrial dust frequently contains significant concentrations of heavy metals such as Al, Si, Cu, Ni, U, V, Pb, and As in urban and mining locations.[8-10] While finer particles (less than 4 μm) enter the deeper lungs, inhaled larger sized particles in the 5 to 10 micrometer range are cleared to the gastrointestinal tract (GIT).[11] If the particles remain as solid matter, they will be expelled from the body in 24 hours.[12] However, the interaction of inhaled particles with physiological fluids in the stomach and lungs causes these heavy metals to seep out, dramatically increasing bio-accessibility. Depending on the chemical make-up of the particulate matter (PM) breathed and the make-up of the physiological fluid they interact with, the solubility of heavy metals inside the human body varies.[13-15] These mobilized heavy metals are known to cause numerous health issues in the human body.[16] Dust sources and the processes that create the dust drives the physicochemical properties of dust such as size, shape, chemical composition, etc., thus having a different impact on human health, not yet explored extensively.

Aside from its effects on human health, industrial dust also has a direct and indirect impact on the worldwide mobilization of Fe, ocean fertilization, and climate. Industrial dust that has been lifted into the atmosphere interacts with atmospheric inorganic and organic acidic gases continuously and is processed by the atmosphere during its lengthy journey before it settles. Industrial dust processing in the atmosphere is crucial because it affects the ocean's input of nutrients and primary productivity. Iron (Fe) is one such nutrient that is limited to most parts of the global ocean due to the basic pH (pH 8.3) of the ocean. During atmospheric processing, chemical and photochemical reactions produce bioavailable dissolved Fe by solid Fe-barring particles hoisted up in the air. Diatoms and

phytoplankton, the primary producers, are thus given the micronutrient Fe they require via the atmospheric processing of dust, which increases their productivity. Because these primary producers are known to be the most significant CO_2 sequester, the atmospheric processing of mineral dust substantially affects climate change.

1.1 Industrial Dust

Industrial dust, commonly referred to as process dust, is produced during the production or manufacturing process. Dust is produced during cutting, drilling, grinding, or sawing.[17-19] Additionally, materials, chemicals, or components utilized in the manufacturing process can cause it to manifest. Metals and chemicals in industrial dust may be toxic if inhaled or come into touch with the skin. In addition, some forms of process dust may be combustible, which, if not handled appropriately, may cause workplace explosions and fire. One of the primary sources of industrial dust is mine dust, and miners are well known for experiencing the worst health effects. Depending on the resources being mined, mine dust contains significant concentrations of heavy metals that, if inhaled, can harm miners.

The mining industry in New Mexico includes the production of coal, gold, silver, copper, lead, uranium, potash, and aggregates.[20] The current study focuses on the effects of inhaled coal and uranium mine dust on human health. High concentrations of heavy metals are present in the respirable portion of mine dust, and when these metals come into contact with bodily fluids, they can become mobilized and available for various chemical reactions inside the body, many of which can be harmful. In addition, the current study assesses coal fly ash's possible role in the global ocean as a source of bioavailable iron and its potential effects on the climate.

1.1.1 Uranium Mine Dust

New Mexico has a rich history of uranium mining.[20] Historically, open pit and underground mining were used to extract uranium in the United States. In traditional mining, uranium ore is extracted from shallow open pits or deep underground shafts. The ore is crushed and sent through a mill, where uranium is extracted and concentrated into "yellowcake"-type uranium oxygen complexes. All these processes can release dust containing uranium. It has been established that the uranium mine dust produced as a result of various mining activities causes various deadly diseases in mine employees. Even though most of the uranium mines in New Mexico are closed or abandoned, the people living near the old mine site continue to experience a wide range of cardiovascular and metabolic diseases.[21-26] The rise in cardiovascular and metabolic diseases in the mining population suggests exposure through a source other than mine activity. According to a number of studies, the depleted uranium in the dust carried by the wind around uranium mines is present in significant amounts and might be dangerous if inhaled.[2] As a result, sediments and dust from places close to two uranium mines in the Grants Mining District (GMD) in New Mexico were gathered for this study.

1.1.2 Coal Mine Dust

A natural byproduct of coal mining, coal mine dust is typically an airborne solid particle with a size range of 1 to 100 μm.[27] Coal mine dust typically results from the breakdown of rocks through collisions, abrasions, cutting, crushing, and explosions, producing irregularly shaped dust particles of diverse sizes.[17-19, 28, 29] Among these, a size fraction smaller than 10 micrometers is respirable and proven to harm the health of mine employees in many ways. Any respirable dust in the mine atmosphere is regarded as respirable coal mine dust (RCMD), to which miners are exposed, according to the United States Mine Safety and Health Administration. According to estimates, between 40 and 95 percent of the respirable coal mine dust (RCMD) in underground coal mines is made entirely of coal, while the remainder is made up of dust from activities such as cutting the roof and floor, using diesel equipment, and rock dusting techniques.[30, 31] Although numerous studies have conclusively shown a connection between RCMD exposure levels and exposure times and the emergence of toxicity, our knowledge of the mechanism underlying the substance's interactions with physiological fluids is still limited.[4, 6, 29, 32-37]. As a result, we examined the physicochemical characteristics of RCMD in the current study in connection to their geographic locations as well as the specific sources of the dust inside the mine, such as the coal seam, rock dust, host floor, and host roof. This investigation will advance our knowledge of the RCMD's toxicological mechanism.

1.1.3 Coal Fly Ash

An inevitable byproduct of coal-fired power plants is coal fly ash. Coal fly ash is made up of particles that are expelled with the flue gases from coal-fired boilers. The size of coal fly ash particles ranges from 0.5 μm to 300 μm, typically spherical. The American Society for Testing and Materials distinguishes between two groups of fly ash. Younger lignite or sub-bituminous coal creates Class C fly ash, but tougher, older bituminous coal often produces Class F fly ash. Compared to Class F fly ash (7% CaO), Class C fly ash typically contains more than 20% lime (CaO). In terms of materials that may be characterized, coal fly ash is one of the most complicated. In diverse ash samples, 316 distinct minerals and 188 distinct mineral classes have been identified.[38-40] Metallic oxides make up the majority of the mixture, and principal oxide contents are often listed in the following order: SiO_2 > Al_2O_3 > Fe_2O_3 > CaO > MgO > K_2O. The environmental impact of some trace components included in fly ash is also a concern.[41-43] Instead of focusing on the leaching and toxicity of trace metals, we assessed coal fly ash as a potential source of bioavailable iron for marine life in this study. Our work focused on coal fly ash samples obtained from US Geological Surveys (USGS); SRM 1633b, SRM 2689, SRM 2690, and SRM 2691.

1.2 Human Health Implications of Industrial Dust

Humans are primarily exposed to industrial dust through inhalation. As was previously indicated, as particle size decreases, airborne particulate matter with a complex chemical makeup becomes more inhalable. Larger inhaled particles can be evacuated to the gastrointestinal tract (GIT), while tiny particles (less than 4 micrometers) enter the deep lung regions.[11] The particles won't cause any harm if they stay solid and are expelled from the body as a result of the body's self-defense process. The interaction of human fluids

with particulate matter, on the other hand, has the potential to leach out heavy metals from the particles, many of which can be quite hazardous. The tiny particles can penetrate deep lung tissue and interact with lung fluids (less than 4 micrometers in size). Larger particles, on the other hand, will enter the gastro-intestinal tract and come into contact with the fluids there.

One such metal is uranium, which has a high level of toxicity when inhaled. The chemical toxicity of this relatively prevalent heavy metal (LD_{50} = 14 mg/kg) is independent of its radioactivity.[44, 45] Uranyl cation (UO_2^{2+}) attaches to DNA in mammalian cells when exposed to depleted uranium, creating a uranium-DNA (U-DNA) adduct that may lead to mutations and a variety of protein synthesis abnormalities, some of which may result in different malignancies.[21-24] Uranium may cause severe oxidative stress and a concurrent decline in the antioxidative capability of lung tissues, according to a study on rat epithelial cells.[22, 25] Another study talks about macrophages dying after being exposed to UO_2^{2+}.[26] Although these studies used uranium in the aqueous phase, additional research has revealed that DNA double-strand breaks may occur in broncho-alveolar lavage cells when exposed to insoluble uranium oxide particles (such as UO_2).[13, 22, 46]

Only a handful of studies have focused on the toxicological implications of inhaled uranium particles that pass through the digestive system. Uranium ingested into the digestive tract can poison the kidneys and cause renal disease.[47] According to a recent study, male and female mice exposed to dissolved uranium through the GI tract experience considerable immunological damage.[48] Another study reports that the chemical speciation of dissolved uranium has little effect on the extent of uranium absorption from the digestive tract.[49] Additionally, multiple earlier studies have linked disruptions of the gut microbiota, which are essential for preserving the health of the systemic immune system exposed to heavy metals [50-53], including uranium.[48] The gut microbiota, on the other hand, may absorb uranium and serve as a barrier between the body and the uranium in the stomach, lessening the overall impact on tissue cells.[54] The conflicting findings in the scholarly literature demand more research on the subject. The fate of solid uranium-containing particles cleared to the human gastrointestinal tract was therefore studied in this work with regard to the mineralogy of uranium and non-uranium minerals identified in the dust.

Inhaling respirable coal mine dust (RCMD) is linked to yet another serious health concern caused by industrial dust. Numerous illnesses can be contracted by coal miners and those who live nearby due to exposure to a high concentration of RCMD. These illnesses can all be fatal in the worst-case scenario, including silicosis, coal workers' pneumoconiosis (CWP), mixed dust pneumoconiosis, dust-related diffuse fibrosis (DDF), progressive massive fibrosis (PMF), emphysema, and chronic bronchitis.[18, 55] Despite significant recent efforts to reduce exposure to RCMD, lung conditions brought on by RCMD continue to pose a significant hazard to the coal mining sector. It was determined that CWP was getting more prevalent and severe towards the beginning of the new millennium.[18, 29, 55] Despite the fact that numerous studies have conclusively shown a connection between RCMD exposure levels and exposure times and the onset of pneumoconiosis, many of these studies also suggest that RCMD toxicity is dependent on a

number of additional physicochemical characteristics in addition to RCMD concentration.[4, 6, 29, 32-37] Studies examining the toxicity of RCMD related to the source are still lacking, even though the individual sources significantly influence the physicochemical characteristics of RCMD created. The underlying causes of the higher occurrence of lung diseases in the particular area, however, can only be better understood by looking into the RCMD features and the amount of toxicity. As a result, in this study we assess the RCMD toxicity with respect to their geographical position as well as specific sources inside the same mine, such as coal seam, host floor, host roof, and rock dust.

1.3 Atmospheric Processing of Industrial Dust: Ocean Fertilization and impact on the Climate

The minerals in industrial dust participate in various heterogeneous reactions with atmospheric gases as they are added into the atmosphere. It forms an aqueous layer, known as the deliquescence layer, by adsorbing the surrounding water molecules onto the surface of the dust particles.[56] This aqueous layer is where many trace gases from the environment can dissolve and generate anions like NO_3^-, SO_4^{2-}, Cl^-, $HCOO^-$, and many more. The adsorption of acidic gases raises the deliquescence layer's acidity to a pH of 1 or 2.[57] These anions subsequently adhere to the surfaces of the metals, creating interfacial complexes that eventually enable the separation of the metals from their oxides. In the deliquescence layer, metals dissolve under acidic circumstances through one of three mechanisms: photo-reductive dissolution, ligand-controlled dissolution, and proton assisted dissolution.[58-60] The mobilized metals in the deliquescence layer subsequently deposit into the ocean surface. In particular, mobilized Fe is the one that satisfies Fe deficiency in global ocean.

Around 95% of all the Fe present in suspended particles comes from lithogenic sources, which account for most of the Fe that is carried through the atmosphere.[61] Therefore, most current research has concentrated on the atmospheric processing of iron-containing mineral dust.[62-65] Alternative sources of Fe, however, come from combustion processes like burning coal, oil, and biomass.[66, 67] Although the amount of Fe from these sources is relatively small, their greater solubility can significantly affect primary production and support the biogeochemical cycle by encouraging greater CO_2 uptake.[5, 68-73] In contrast to the overall Fe emission from mineral dust, which was estimated by Wang et al., (2015) to be 41.0 Tg yr^{-1}, the average Fe emission from combustion sources between 1960 and 2007 was 5.3 Tg yr^{-1}.[74] Additionally, according to their estimate, there is an 8.4 Tg yr^{-1} overall sink for Fe deposition across the world's oceans, with combustion sources accounting for 7% of that amount. The coal combustion process accounts for the majority of the Fe from the combustion sources. As a result, in recent years, numerous research has looked into coal combustion products, or coal fly ash, as potential sources of bioavailable iron for the ocean.[5, 7, 75]

Further, Fe solubility during atmospheric processing is significantly associated with the inherent properties of the Fe-containing particle, including size, shape, specific surface area, iron speciation, and Fe distribution within the particle.[63, 76-81] Additionally, a study revealed that the presence of metal oxides other than those containing iron, such as Al_2O_3, CaO, TiO_2, and others, affects the leaching of iron during atmospheric processing.[82] It has been claimed that the presence of Ti promotes the dissolution of Fe

from mineral dust that contains Fe.[83, 84] While the sources show that CFA particles have a significant likelihood of mixing with TiO_2 (the most prevalent industrial dust) during their time in the environment, the elemental composition also points to a sizable Ti content in the CFA particles.[85-87] Although we predicted that the Fe leaching from CFA would increase in the presence of TiO_2, following the same pattern as mineral dust, it has not yet been verified. Therefore, we specifically investigated Fe leaching and speciation for four standard reference materials for coal fly ash under simulated atmospheric processing in the presence of TiO_2.

The atmospheric processing of coal fly ash contributes relatively little bioavailable Fe globally. However, it is predicted to account for 50% of the Fe deposits in the water surrounding industrialized regions.[88] Additionally, because CFA particles are in a fine mode (<1 μm) in the atmosphere, they can travel a considerable distance before being deposited in the ocean.[89] As was previously mentioned, CFA will eventually create a deliquescence layer during long-range atmospheric transport, making Fe available and resolving the ocean's Fe shortfall. As a result, it will boost primary producer phytoplankton productivity, which is a significant ocean CO_2 scavenger. Further, the albedo effect of dust particles considerably impacts the global radiative budget.[90, 91] Dust particles affect the chemical equilibrium of the atmosphere by acting as carriers for adsorbed species or as reaction sites.[92-94] Overall, industrial dust processing by the atmosphere, mainly coal fly ash, has a considerable impact on our climate, and adding this to atmospheric models would increase predictability.

1.4 Synopsis of Dissertation Chapter

Collecting field samples, analyzing them in the lab, and performing computer calculations using model systems are all part of the study and understanding of the effects of industrial dust. In conjunction with laboratory investigations, the physicochemical characteristics of the samples provide insights into understanding the impact of industrial dust on human health and the environment. The results from the laboratory tests and the collection of field samples were utilized to establish a model system or to build one that already existed to better understand the impact of industrial dust.

Investigations into how industrial dust interacts with specific bodily fluids and ambient gases have utilized a variety of experimental methodologies. ATR-FTIR is used to determine the surface functional group. The determination of particle size and shape using scanning electron microscopy (SEM) and the detection of mineralogy using X-ray diffraction are also included. Dissolution experiments and ICP-MS analysis were used to determine the chemical composition as well as the concentration of bio-leached metals. Few other complimentary characterization techniques have been utilized in addition to the above. Chapter 2 provides a detailed description of the experimental and theoretical techniques that were employed for the research included in this thesis.

In Chapter 3, the ability of two distinct gastrointestinal fluids, SGF and SIF, to absorb uranium from uranium-containing dust is assessed in order to determine their toxicity. Two samples were collected from St. Anthony and three from the Jackpile mine in New Mexico's Grants mining district. The collected dust samples were characterized to determine their particle sizes, shapes, and compositions. Then the dust samples were

allowed to dissolve in simulated gastrointestinal fluids and the dissolved U concentrations were assessed using ICP-MS. Uranium in dust dissolved depending on the mineralogy, pH, and composition of the fluid. Additionally, to study the mineralogy dependent uranium solubility, geochemical calculations using the PHREEQC 3.3.8 model and updated MINTEQ database were combined with experimental results. The information in this chapter offers significant new understandings on the radiation-independent toxicity of solid phase uranium. It demonstrates the urgent necessity for site-specific toxicological studies as opposed to superficial generalist assessments.

Chapter 4 reports the dependency of RCMD properties and toxicity based on their geographical location. Two samples from the Rocky mountain regions and three samples from Appalachian mountain regions were collected, prepared, and evaluated to determine their size, shapes, and compositions. The degree of toxicity of the dust samples were determined by dissolution experiments in artificial lysosomal fluid (ALF) and gamble solution (GS), which replicate the fluid in macrophages and the interstitial lung environment, respectively. The dissolved metal concentrations were determined using ICP-MS and correlated to their physicochemical properties. This chapter also includes the in-vitro cytokine responses for relevant cell types followed by dust exposure. The data reported in this chapter provides better understanding on the RCMD characteristics and their relation to the site specific toxicity.

As a continuous interest, a range of sources, including coal seams, rock dust, host floors, and host roofs from intra- and inter-mines, were used to examine the properties and toxicity of RCMD in Chapter 5. This study aims to measure the metal leaching from RCMD that was gathered from 11 different sources in the lung fluid and link it with the in-vitro immune responses. In order to do such, dissolution tests were carried out utilizing two simulated lung fluids: GS and artificial lysosomal fluid (ALF). The immunological responses and cell viability were examined in in-vitro tests utilizing the appropriate cell lines. The result reported in this chapter sheds light on the site specific physicochemical properties and their varying toxicological impact, and demonstrates the importance of having a risk assessment model incorporating these findings.

In addition to being hazardous when inhaled, Fe-containing PM suspended in the air considerably impacts the amount of bioavailable Fe entering the world's oceans, which in turn impacts the climate. We discussed coal fly ash (CFA) as a source of bioavailable iron in Chapter 6. Nitric acid dissolution tests were conducted in atmospherically appropriate circumstances, and then the amounts of dissolved Fe were examined using a spectroscopic approach. We also investigated the influence of various crystal phases of titanium dioxide (TiO_2), rutile and anatase, affected the CFA's ability to leach iron. Our results demonstrated that titanium improves iron mobility from samples when titanium is introduced externally or already present in the sample. Thus, this work provides essential yet undiscovered information about CFA as a source of bioavailable iron.

Chapter 7 summarizes the key findings of the current study, and provides future directions to achieve long term research goal. Important concepts that will improve our understanding of the earth system are highlighted. These concepts include potential heterogeneous chemistry and photochemistry of the atmosphere as well as the health effects of breathed industrial dust.

CHAPTER 2

EXPERIMENTAL AND COMPUTATIONAL METHODS

We utilized a variety of experimental methodologies and techniques as well as computational modeling tools to examine the effects of industrial dust particles on human health and the environment. This chapter discusses these methods as well as supplementary characterization methods.

2.1 Experimental Methods

2.1.1 Physical & Chemical Characterization

2.1.1.1 Scanning Electron Microscopy

Scanning electron microscopy (SEM) (a Nova Nano SEM 450 equipment) was used to collect images for the particles. A transfer pipet was used to distribute particles on a carbon tape affixed to the aluminum stub after being suspended in isopropyl alcohol. Stubs that have been prepared were air-dried and then coated with platinum (Pt) using a sputtering process. The particle size and shape distributions were determined by analyzing about 500 particles using the ImageJ software package.

2.1.1.2 X-ray Diffraction Spectroscopy

X-ray diffraction spectroscopy was used to analyze the mineralogy of the materials using a PANalytical X'Pert Pro diffractometer (PANalytical B.V., Almelo, The Netherlands). A 40-minute scan was utilized to gather the spectra from a Cu Kα source in the 2θ range from 5˚ to 70˚. The divergence slit was fixed at 0.25˚. Using the HighScore Plus software (Malvern Panalytical Ltd., Malvern, UK), the raw data were compared to the mineral dataset.

Pre-concentration was done when the number of crystals was less than 1%, specifically for the samples of uranium dust. The materials were first sieved through a 500 μm US standard sieve to eliminate debris. The trace minerals were covered on the quartz grains and collected by using gentle scratching with a porcelain pestle. Additional sifting was done utilizing US standard sieves of 120 μm, 45 μm, and 20 μm. XRD was used to examine the collected finest fraction. The spectra were then matched to those of frequent main and minor minerals that are known to exist in New Mexico.

2.1.1.3 Brunauer-Emmett-Teller (BET) Theorem

The sample-specific surface area of the dust sample was determined using a Quantachrome Autosorb AS-1 instrument using the Brunauer-Emmette-Teller theorem. The surface area of the dust samples was obtained using a 7-point N_2-adsorption isotherm following an overnight outgassing at 150˚C according to equation 2.1.

$$\frac{1}{W\left((P_0/P)-1\right)} = \frac{1}{W_m C} + \frac{C-1}{W_m C}\left(\frac{P}{P_0}\right) \qquad 2.1$$

Where W is the weight of adsorbed gas at specific relative pressure, P/P_0 indicates the relative pressure, and W_m is the weight of adsorbed gases that forms a monolayer. In this equation, C is the BET constant, which is correlated with the strength of the interactions between the adsorbent and adsorbate.

2.1.1.4 Fourier Transform Infra-red (FTIR) Spectroscopy

Nicolet iS50 series FTIR (Thermo Scientific™, Waltham, Massachusetts, USA) with Ge-ATR crystal was used to acquire FTIR spectra of dust samples. A 2 mL centrifuge tube was used to prepare the sample. About 10 mg of the dust was utilized in the sample preparation, which was done in 1 mL of isopropyl alcohol (IPA). Prior to transferring the sample suspension in the IPA to the ATR crystal and subsequent air drying, the sample suspension was sonicated for 20 minutes. The ATR crystal acquired a thin layer of dust as a result. FTIR spectra were collected using 250 scans with 4 cm^{-1} resolutions. The spectra were then processed against the bare crystal; only the processed spectra are reported here.

2.1.1.5 Microwave Digestion

The elemental composition of metals in the dust samples was obtained using an inductively coupled plasma mass spectroscopy (ICP-MS, Agilent 7900) following the SK-PE-017 method. It's a microwave-based acid digestion method for coal samples comprising two steps. In the first step, about 200 mg of the dust samples was weighed and added to individual digestion tubes, followed by addition of 10 mL of concentrated nitric acid. The microwave program we used was a 10-minute ramp to 190˚C and held the temperature for 15 minutes with a 1200 W system power. In the second step, we added 2 mL of concentrated trace metal grade hydrofluoric acid, followed by a microwave program with a 20-minute ramp to 230˚C, and held it for the next 15 minutes. A standard reference material CLB-1 from the USGS was used with each batch as a quality control for the digestion method.[95] The digested samples were filtered and diluted to analyze using the ICP-MS.

2.1.2 Metal Leaching Experiment – Batch Reactor

Dissolution studies employing batch reactor systems were conducted to simulate the metal leaching from dust particles in various fluid conditions. The dissolution tests were conducted in a custom dark room under both dark and light conditions, while light conditions were reproduced with a solar simulator (150 W Xe lamp, Newport Corp Sol1A ABB). The batch reactor was made with a capacity of 100 mL and a removable airtight lid with a quartz window (12.5 cm^2) that allowed light to enter during solar experimentation.

A schematic of the batch reactor is shown in the **Figure 2. 1**. A 20 mg of dust loading was applied to 100 mL of the dissolution medium. The media was purged with O_2 to create an oxygenated environment of lung or with N_2 to create a deoxygenated atmosphere for atmospheric processing. Depending on the type of experiment, a heated water jacket was used to keep the temperature consistent during the dissolution experiment. Using a magnetic stirrer, the suspension was constantly stirred. Depending on the type of experiment, a sample aliquot of 1.5 mL was collected at regular intervals for up to 24 hours or 48 hours. In preparation for further examination, the collected samples were centrifuged, filtered through a 0.2 μm disk filter, and then stored. For uranium and coal dust, the dissolved metal concentrations were measured using ICP-MS, and the dissolved iron was measured using the 1, 10-Phynanthroline method for coal fly ash.[96] Each of the dissolution experiment was done in triplicate, and the average dissolution with standard error was reported.

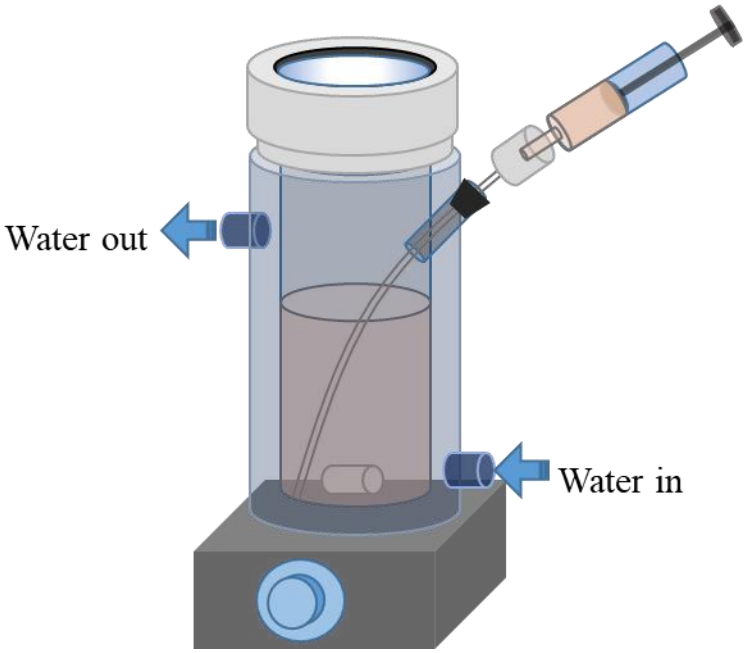

Figure 2. 1: Schematic diagram of a custom build batch reactor

2.1.3 Quantitative Determination of Uranium & Other Metals - ICP-MS

The concentration of dissolved metals was measured using an Agilent 7900 Inductively Coupled Plasma Mass Spectrometer (ICP-MS). The aqueous sample was first introduced into the nebulizer in ICP-MS, where it was turned into an aerosol. After being nebulized, the sample entered the plasma torch, where it was broken down into atoms and ionized. The non-ionized atoms were separated as the stream of ions went through magnetic lenses and were then channeled to the quadruple chamber. Particles were suspended in a magnetic field in the quadrupole chamber. The ions were subsequently accelerated at various speeds depending on their mass-to-charge ratio using certain magnetic field oscillations. Thus the electromagnetic field was then used to sort and detect elements based on their mass-to-charge ratio. The ICP-MS is designed to count the atoms in the sample being analyzed and then determine the concentration of each element in that

sample using the sample's volume and dilution factor. Prior to the examination of the sample, the instrument was always calibrated using user-prepared calibration standards. To counteract potential matrix effects of the medium, all samples and standards were created using bodily fluids that were five times diluted. A second internal standard and USGS standard reference materials for ICP-MS were used to evaluate the calibration's veracity. Every ten samples, a set of calibration standards and a blank sample were introduced in order to ensure instrument functionality and offer real-time monitoring.

2.1.4 Quantitative Determination of Iron - UV-Vis

Dissolved iron, both Fe(II) and total Fe, was quantitatively determined for coal fly ash samples in HNO_3 media. The 1,10-phenanthroline method, explained in this section, was applied for that objective.[96] Two portions of the collected samples from the batch reactor, each containing 0.5 mL, were placed in a 2 mL centrifuge tube. With the aid of 20 μL of concentrated hydrochloric acid, both portions were acidified. The total Fe was determined using one portion, while the Fe(II) was determined using the other. Following the acidification, 10 μL of hydroxylamine hydrochloride ($NH_2OH.HCl$), a reductant, was added to one portion to reduce any possible Fe^{3+} in the media and convert all dissolved iron to Fe^{2+} for the total iron determination. For Fe(II) determination in the presence of Fe(III), 25 μL of complexing agent NH_4F was added, which formed complexes with only Fe(III). NH_4F was added to act as a masking agent for the Fe(III) and make it unavailable for the subsequent reaction with 1, 10-phenanthroline. In the next step, 100 μL of 1, 10-phenanthroline, and 100 μL of ammonium acetate buffer were added to the mixture. After 20 minutes in a dark environment, the reaction mixture was examined for the presence of Fe(II) or total Fe using a UV-Vis analyzer to determine the absorbance at 510 nm. The instrument calibration was done using known concentration of iron.

2.2 Computational Methods

2.2.1 PHREEQC 3.3.8 Geochemical Modeling

To better comprehend the influence of mineralogy on elemental speciation and saturation for batch reactions, we employed PHREEQC 3.3.8 geochemical modeling. It is a computer-based program created in the C programming language. The acronym PHREEQC stands for pH Redox Equilibrium in C language. The program is made to perform various equilibrium calculations in aqueous media, including reversible and irreversible processes, interactions between aqueous media and gases and minerals, gas-solid contacts, surface complexation, and solid-solution interactions. Additionally, it has the ability to compute mole transfer processes, temperature- and pressure-controlled reactions, and kinetically-driven reactions. Within a given compositional uncertainty, PHREEQC's inverse modeling mode identifies the minerals and gases that are responsible for certain compositional differences.

PHREEQC processes make use of chemical equations as well as known thermodynamic and kinetic factors. The major database for this investigation was the built-in MINTEQ database, which had been modified to include the components of fluids and dust. When a new species was introduced, its molecular weight, chemical formula, and associated chemical processes with equilibrium constant were also introduced.

Additionally, the volume and pH of the solution, temperature, pressure, mineralogy of dust, and surface characteristics of minerals were incorporated as suitable in the model inputs. The calculations were carried out in batches. The Appendix contains the PHREEQC input files that were used in this study.

2.2.2 Quenched Solid Density Functional Theory (QSDFT)

When standard macroscopic theories cannot adequately explain the filling of micropores and narrow mesopores, the density functional theory of molecular simulation and molecular dynamics offers a far more realistic approach. As a result, pore size distribution can be estimated more precisely using DFT calculations based on molecular-level interaction. Furthermore, the local fluid structure close to the pores is accurately described by the non-local density functional theory (NLDFT), which was created based on the intermolecular interactions of fluid-fluid and solid-fluid. It is possible to explain the relationship between experimental isotherms on a porous solid and isotherms derived by these microscopic methods in terms of a generalized adsorption isotherm.

$$N(P/P_0) = \int_{W_{MIN}}^{W_{MAX}} N(P/P_0), W) f(W) dW \qquad 2.2$$

Where

$N(P/P_0)$ = Experimental adsorption isotherm data

W = Pore width

$N(P/P_0, W)$ = Isotherm on a single pore of width W

f(W) = Pore size distribution function

The generalized adsorption isotherm reflects the assumption that the total isotherm consists of a number of individual single-pore isotherms multiplied by the relative distribution. Pore size distribution is then derived by solving this generalized adsorption isotherm equation. However, it does not explain the effect of surface roughness and heterogeneity.

In the current work, Quenched Solid Density Functional Theory (QSDFT), a modified NLDFT that takes the effects of surface roughness and heterogeneity into account, was used in place of regular NLDFT because coal dust samples are known for their surface roughness and structural disorder. The pore size study using the Quantachrome QSDFT method enables the estimation of pore size distributions based on the slit pore model.

CHAPTER 3 [1]

THE FATE OF INHALED URANIUM-CONTAINING PARTICLES UPON CLEARANCE TO GASTROINTESTINAL TRACT

3.1 Abstract

Uranium-bearing respirable dust can cause various health problems, such as cardiovascular and neurological disorders, cancers, immunosuppression, and autoimmunity. Exposure to elevated levels of uranium is linked to many such health conditions in Navajo Nation residents in northwestern New Mexico. Most studies have focused on the fate of inhaled dust particles (<4 mm) in the lungs. However, larger-sized inhaled particles (10–20 mm) can be cleared to the human gastrointestinal tract (GIT), thereby enabling them to interact with stomach and intestinal fluids. Despite the vital importance of understanding the fate of uranium-bearing solids entering the human GIT and their impact on body tissues, cells, and gut microbiota, our understanding remains limited. This study investigated uranium solubility from dust and sediment samples collected near two uranium mines in the Grants Mining District in New Mexico in two simulated gastrointestinal fluids representing fasting conditions in the GIT: Simulated Gastric Fluid (SGF) and Simulated Intestinal Fluid (SIF). The dissolution of uranium from dust depends on its mineralogy, fluid pH, and composition. The dust samples from the Jackpile mine favored higher solubility in the SIF solution, whereas the sediment samples from the St. Anthony Mine favored higher solubility in the SGF solution. Further, geochemical calculations performed with the PHREEQC modeling program suggested that samples rich in the minerals andersonite, tyuyamunite, and/or autunite have higher uranium dissolution in the SIF solution than in the SGF solution. We also tested the effect of added kaolinite and microcline, which are both present in some samples. The ratio of dissolved uranium in SGF relative to SIF decreases with the addition of kaolinite for all mineral phases but andersonite. With the addition of microcline, the ratio of dissolved uranium in SGF relative to SIF decreases for all the tested uranium minerals. The most prevalent oxidation state of dissolved uranium was computationally determined as +6, U(VI). The geochemical calculations made with PHREEQC agree with the experimentally observed results. Therefore, this study gives insight into the mineralogy-controlled toxicological assessment of uranium-containing inhaled dust cleared to the gastrointestinal tract.

[1] Chapter is reprinted/adopted from authors own published work "E. Hettiarachchi, M. Das, D. Cadol, B. A. Frey and G. Rubasinghege, The Fate of Inhaled Uranium-Containing Particles Upon Clearance to Gastrointestinal Tract. **Environ. Sci.: Processes Impacts**, **2022**, 24, 1257 – 1266" does not require specific permission for reprint in the dissertation.

3.2 Environmental Significance

In places where uranium mining occurred, the windblown dust contains a significantly higher quantity of uranium than the background levels. Many studies are focused on understanding the fate of this uranium in human lungs once inhaled. However, the relatively larger-sized inhaled particles clear into the human digestive system. Here, we focus on understanding the fate of uranium in inhaled dust in the simulated human stomach and intestine. We report that the uranium leaching in the stomach is primarily dependent on the mineralogy of dust inhaled. Therefore, we state that the toxicological studies of inhaled uranium should be site-specific. Furthermore, the dust mineralogy and body conditions should be considered when assessing their toxicology.

3.3 Introduction

Uranium is the heaviest naturally occurring metal and is radioactive.[45] Being a heavy metal, its chemical toxicity is independent of the radioactivity related toxicity and thus cannot be overlooked.[47] The established maximum U contamination level in drinking water is 30 ppb.[48] Exposure to higher contamination levels can cause cardiovascular and neurological disorders, cancers, immunosuppression, and autoimmunity.[48, 97-99] During exposure to depleted uranium, uranyl cation (UO_2^{2+}) binds to DNA in mammalian cells, forming a uranium-DNA (U-DNA) adduct that could cause mutations, thereby triggering a range of protein synthesis errors, some of which may lead to various cancers.[21-24] A study on rat epithelial cells showed that uranium might induce significant oxidative stress and a concomitant decrease in the anti-oxidative potential of lung tissues.[22-25] Another study discusses the death of macrophages when exposed to UO_2^{2+}.[26] While these studies were conducted with aqueous phase uranium, others have reported that insoluble uranium oxide particles (e.g., UO_2) may cause the breakdown of DNA double strands in broncho-alveolar lavage cells.[13, 22, 46] A recent study showed that exposure to mine-site derived particulate matter (PM) containing uranium-containing particles exacerbates neurological and pulmonary inflammatory outcomes in an autoimmune mouse model.[100] One sample site used in the study, St. Anthony mine, New Mexico, was also used as a study site for our current study.

Several studies suggest that humans are primarily exposed to uranium through inhalation.[11, 12, 44] Airborne particulate matter with a complex chemical composition becomes more inhalable as particle size decreases. While smaller particles (< ~4 μm) reach the deep lung environments, particulate matter of larger sizes (10 μm – 100 μm) can be cleared into the gastrointestinal tract (GIT).[11, 12, 101] Furthermore, the number of particles cleared from the nose to the GIT can be as high as 50% of the deposit.[102, 103] The GIT is a critical organ with high absorbance capacity that is comprised of multiple tissues that are home to diverse and abundant essential immune cells and microbiota.[12, 48] Therefore, studies are required to investigate the exposure and toxicity of uranium in the GIT following clearance from the inhalation route.[11, 104] Although the absorption of solid uranium species in the GI tract is relatively poor, the efficiency increases with the increased solubility.[47] On average, 1–5 μg of uranium are ingested daily through food and water consumption, whereas only 0.5 – 5% of the uranium ingested is usually absorbed.[47, 49] Human daily doses are two to three times higher in contaminated areas

such as those near mine sites.[47] In the current study, the leaching capacity of uranium from inhaled dust that may be cleared to the gastrointestinal tract is investigated using two different simulated gastrointestinal fluids. The two fluids are simulated gastric fluid (SGF) and simulated intestinal fluid (SIF). They simulate the stomach environment and the human intestine conditions, respectively, in the fasted state.[105] The compositions of these fluids are provided in the **Table 3.1**.

Toxicity studies on inhaled uranium cleared to the digestive tract are relatively scarce. However, uranium entering the digestive tract can damage the kidneys, causing toxicity.[47, 106, 107] A recent study reported that exposure to dissolved uranium through the GI tract causes significant immunotoxicity among male and female mice.[48] Another study concluded that the absorption of uranium by the digestive tract does not significantly influence the chemical speciation of dissolved uranium.[49] Further, numerous previous studies have linked heavy metal exposure[50-53], including uranium[48], to disruptions of the gut microbiota that are crucial for maintaining systemic immune health. On the other hand, Cleveland et al. suggested that the gut microbiota may take up uranium and act as a barrier between the body and the uranium in the stomach, thereby reducing the overall impact of uranium on tissue cells.[54] The contrasting conclusions within the scientific literature call for further studies on the topic.

In recent decades, a notable increase in cardiovascular and metabolic diseases in the Navajo population residing close to the Grants Mining District (GMD), New Mexico, has been observed, with only limited investigations into possible contributions from environmental contaminants, in particular uranium and vanadium.[108] In a previous study, we investigated uranium exposure via dust inhalation and subsequent dissolution in simulated human lung environments in relation to the source of the dust.[2] In this study, we employed similar methods in understanding the fate of solid uranium-bearing particles cleared to the human gastrointestinal tract. This is further focuses on the mineralogy of uranium and major non-uranium minerals present in the dust collected near mine sites in the GMD. In addition to laboratory simulations, a geochemical modeling software program, PHREEQC 3.3.8, was used to further investigate the effect of mineralogy on the dissolution of uranium in these simulated fluids.[109, 110] By the combined results of laboratory studies and computational-geochemical studies, we report that the mineralogy of uranium-bearing dust impacts the extent of dissolution of uranium in these simulated body conditions. Further, we report that a synergistic impact of multi-mineral composition plays a vital role in uranium mobilization in the solutions, thus, attributing solubility and toxicity trends to a single mineral phase can cause errors in toxicity assessments. However, it is important to mention that the toxicity of undissolved particulate matter has not taken into account in this study.

3.4 Materials and Methods

3.4.1 Dust and Sediment Sample Collection

Dust and sediments were collected from four sites near Jackpile and St. Anthony mines, within ~5 km of communities in the GMD, New Mexico. Rock and sediment samples were collected from an un-reclaimed open pit at St. Anthony mine (35.1562 N latitude, 107.2940 W longitude) during the summer of 2017. Passive dust collectors (Big

Spring Number Eight dust flux samplers), installed 0.25 m above the ground surface, collected samples from November 2016 to August 2017 at three locations near the mines: site M, within a reclaimed pit at Jackpile mine (35.1240 N, 107.3705 W); site K, 3 km downwind of both reclaimed and un-reclaimed mine pits (35.1298 N, 107.2929 W); and site L, 4 km downwind (35.1259 N, 107.2859 W). (**Figure 3.1**) The collected samples from dust sites M, K, and L, and from the St. Anthony mine were sieved with a 500 µm US standard sieve to remove any organic debris before use in dissolution studies. Sieved samples of the size fraction less than 20 µm were used for dissolution studies in Simulated Gastrointestinal Fluids (SGIF).

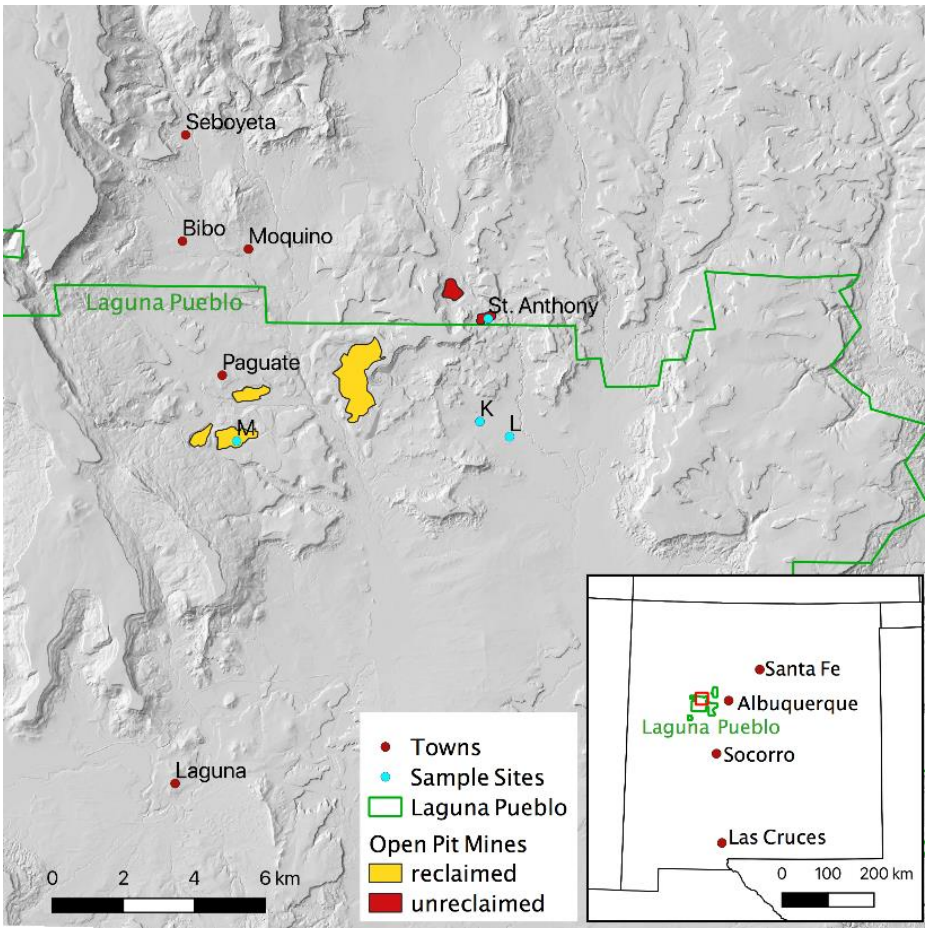

Figure 3. 1: A map of the sampling area.

3.4.2 Standards & Chemicals

All chemicals were reagent grade or better and used as received. A standard sample of U_3O_8 from the National Bureau of Standards (NIST, Assay 99.9%) was used as a proxy in this study. All the solutions and the media were prepared in purified water (18.2 MΩ, Milli-Q-A10).

Table 3. 1: The compositions of the Simulated Gastrointestinal Fluids[105]

	SGF	SIF
Sodium taurocholate (mM)	0.08	3
Lecithin (mM)	0.02	0.2
Pepsin (mg/mL)	0.1	-
Sodium chloride (mM)	34.2	68.62
Maleic acid (mM)	-	19.12
Sodium hydroxide	-	34.8
pH	1.6	6.5

The following chemicals were used to prepare simulated gastrointestinal fluids according to the composition described in Marques et al., 2011.[105] The chemicals are sodium taurocholate ($C_{26}H_{44}NNaO_7S$, Beantown Chemicals, 97%), lecithin ($C_{42}H_{80}NO_8P$, VWR Chemicals, High purity grade), pepsin (VWR Chemicals, Biotechnology grade), maleic acid ($C_4H_4O_4$, TCI, +99.0%), sodium chloride (NaCl, Acros, +99%), sodium hydroxide (NaOH, VWR International, 97%), and hydrochloric acid (HCl, VWR International, ACS grade/36.5-38.0%).

3.4.3 Characterization of Dust Samples

The surface areas of samples were measured in a seven-point N2-Brunauer-Emmet-Teller (BET) isotherm using a Quantachrome Autosorb-1 surface area analyzer. Samples were outgassed overnight (~24 h) at a temperature of 105°C prior to the BET analysis. The particle size of the sieved samples was measured using SEM images. (**Figure 3.2** and **Figure 3.3**) To determine the elemental concentrations of each dust sample, an acid digestion procedure was followed. A 0.2 ± 0.01 g subsample was weighed from each sample and placed in an individual digestion tube. Before analysis, samples were sieved through a 500 μm sieve to remove organic debris. A 3 mL of trace-metal-grade hydrofluoric acid and 9 mL of trace-metal-grade nitric acid were added to each digestion tube, and each tube was capped and placed in a holder. A preset microwave routine (Milestone EthosUP) included a 25-minute ramp to 180°C, after which the oven held that temperature for 10 minutes, consistent with the EPA 3052b digestion method.[111] Major, minor, and trace elements were quantified using inductively coupled plasma-mass spectroscopy (ICP-MS, Agilent 7900).

X-ray diffraction (XRD) analyses of dust samples were performed in a Pananalytical X'Pert Pro Diffractometer equipped with a copper source. Due to the total %U of these samples being lower than 1% (the usual detection limit of the XRD analysis), a pre-concentration procedure was carried out. Briefly, the dust samples were first sieved

through a 500 μm US standard sieve to remove debris. The uranium minerals in these samples are coatings around the quartz grains. Therefore, the particles were lightly scratched using a porcelain pestle to scrape out the uranium minerals while sieving. Additional sieving was carried out using 120 μm, 45 μm, and 20 μm US standard sieves. The finest fraction collected was analyzed with XRD. Then, the spectra were compared with 15 different common uranium minerals in New Mexico along with common major minerals (i.e., quartz, kaolinite, microcline, dolomite, calcite, and rutile). The presence of uranium minerals was confirmed only when their intensities and d-spacing were matched with respective standard patterns with at least five major peaks. Additional information on this method is provided in our previous study.[2]

3.4.4 Dissolution of Uranium in Simulated Gastrointestinal Fluids

Dissolution studies were carried out in a custom-built glass reactor inside a dark room to measure the total dissolved uranium concentration (TDU). The capacity of the reaction vessel was 100 mL with a removable airtight top. The sample loading was 20 mg in 100 mL of the simulated fluids. During the reaction, the temperature was maintained at 37˚C using a heated water jacket, and the reaction mixture was in continuous agitation by using a magnetic stirrer at 1000 rpm. The sample aliquot of ~2 mL was collected periodically using a disposable syringe connected to a 12 cm Teflon tubing. The collected samples were centrifuged and filtered via 0.2 μm syringe filters before analyzing them with ICP-MS to avoid solid carryovers. All dissolution studies were performed in triplicate, and mean TDUs have been reported with the standard deviation. The pH of the media was measured before and after each dissolution experiment.

3.4.5 Detection of Uranyl Cation Formation

A Uranyl-Curcumin-Triton-X System was prepared according to the method described by Zhu et al.[112] A 3% Triton-X 100 solution was combined with natural pigment curcumin as the fluorescence probe for the uranyl cation detection. The calibration standards were prepared using 400 μM stock uranyl acetate solution prepared in SGF and SIF matrices. Extended information on this method is provided in our previous study.[2] However, the UV-VIS absorption of two stock solutions made on SGIFs (Simulated Gastro Intestinal fluid) was compared with a MilliQ water-based stock solution using Evolution 200 UV-Vis Spectrometer to confirm that there was no significant interference from the matrix.

3.4.6 Geochemical Modeling

PHREEQC 3.3.8 with a modified MINTEQ database was employed in geochemical modeling.[109] In the database, taurocholate is represented by taurine and pepsin as glycine in order to incorporate essential thermodynamic parameters. The maximum dissolved uranium concentration at equilibrium in an oxidizing atmosphere in the two simulated gastrointestinal fluids was calculated for identified uranium minerals and total

site mineralogy. These model calculations were singular, and no replicates were conducted. Further, changes in uranium solubility in the presence of kaolinite or microcline for each uranium mineral were investigated. Kaolinite was detected as a major mineral in all tested samples, whereas microcline was detected in all samples except the St. Anthony sediment sample. For individual uranium minerals, excess of the mineral in 100mL of the gastrointestinal fluids in oxidized conditions at 37°C was considered. For simulations with the site mineralogy, molar ratios of minerals were selected based on the XRD peak intensities. The SGF and SIF input files are provided in Appendix.

3.5 Results and Discussion

3.5.1 Particle Characterization

The particles used in this study were sieved prior to use. The particle sizes were analyzed from SEM images with the software package ImageJ. The average particle sizes were 9.32 ± 4.54, 15.97 ± 7.8, 10.21 ± 5.10, 12.72 ± 7.05, and 3.64 ± 2.49 μm in diameter for the samples from Site K dust, Site L dust, Site M dust, St. Anthony sediment, and St. Anthony rock respectively. The SEM images and their respective particle-size distributions are reported in the **Figure 3.2** and **Figure 3.3**. The sieving was conducted softly, and mild physical abrasion was employed. The measured surface areas and %U of each dust sample after sieving are provided in **Table 3.2.** All but the St. Anthony samples contain less than 0.40% total uranium. St. Anthony sediment and rock samples contain 0.87% and 4.42% U, respectively. As revealed from XRD analysis (**Table 3.3**), the uranium mineralogy of these samples is a combination of commonly found uranium minerals in the area.[2, 113]

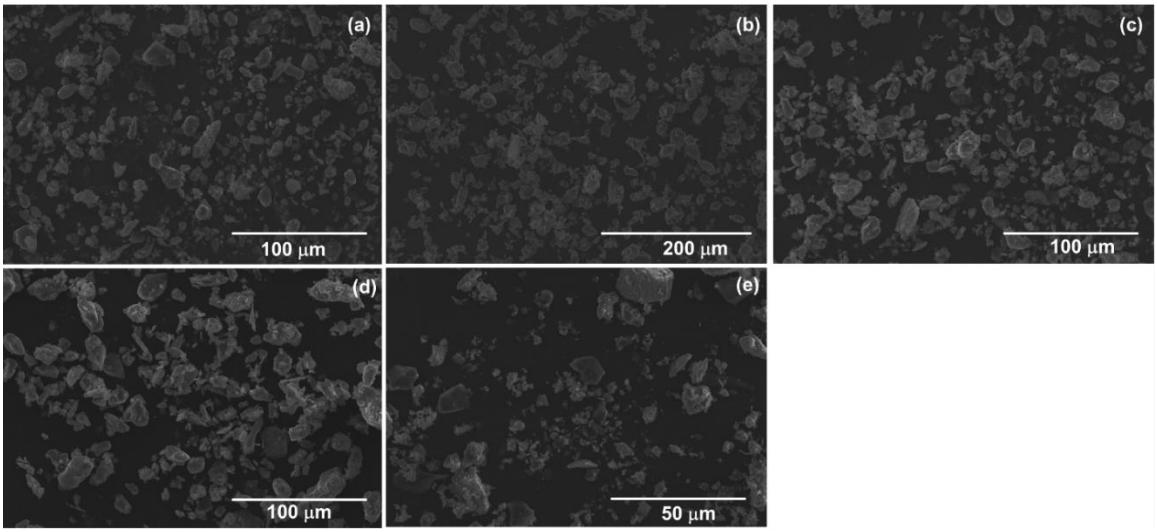

Figure 3. 2: SEM images of the samples from (a) Site K (b) Site L (c) Site M (d) St. Anthony Mine sediment, and (e) St. Anthony rock

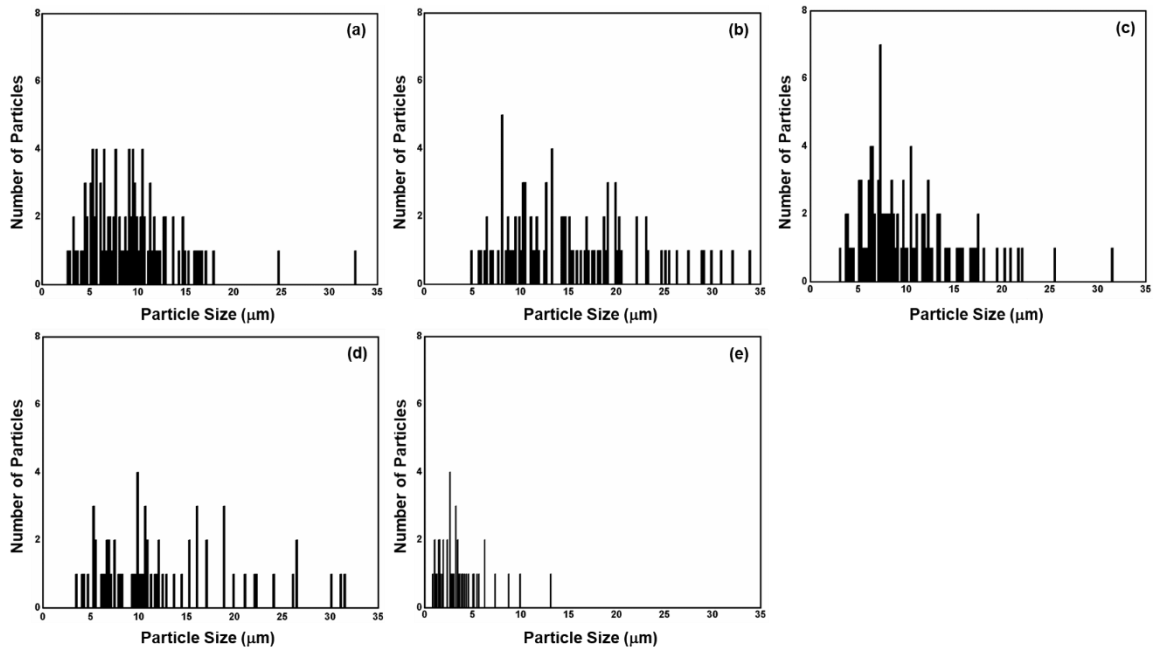

Figure 3. 3: Particle-size distribution of the samples from (a) Site K (b) Site L (c) Site M (d) St. Anthony sediments, and (e) St. Anthony rock

3.5.2 Dissolution of Uranium in Simulated Gastrointestinal Fluids

Inhalation of airborne dust particles poses a great health risk to humans, as these dust particles often contain toxic heavy metals.[114] While the finer fraction of these particles reaches the deeper lung and interacts with human lung fluids, the larger particles may clear to the human digestive system.[11] Once cleared to the human digestive system, these dust particles are likely to interact with fluids in the stomach and intestine.[12, 115, 116] Although, in human body conditions, materials in the stomach first interact with gastric fluids, and the undigested remainder passes to the human intestine, in our bench experiments, a fresh sample was used each time for the two different gastrointestinal fluids. This was to keep the experiments simple enough to understand the uranium leaching capacity and possible mechanisms. In the fasted state, the stomach contains about 40 mL of capacity.[105] The 20 mg of dust used in 100 mL in our experiments roughly converts to 8 mg of dust exposure within 24 hours.

Table 3. 2: Surface area analysis and the %U analysis of the uranium-containing samples.

Sample	**Source of the samples**	**7 points N2 BET surface area (m2/g)**	**%U**
U3O8	National Bureau of Standards	0.46±0.04	85
St. Anthony sediment	St. Anthony Mine	1.61±0.08	0.87
St. Anthony rock	St. Anthony Mine	134.15±1.58	4.42
Site K dust	Jackpile Mine	31.85±0.41	0.38
Site L dust	Jackpile Mine	38.85±1.10	0.12
Site M dust	Jackpile Mine	36.26±1.46	0.10

Table 3. 3: Identified minerals in the samples with XRD analysis. √ Indicates they were identified

Sample	**Chemical Formula**	**St. Anthony sediment**	**St. Anthony Rock**	**Site K**	**Site L**	**Site M**
		Major Minerals				
Quartz	SiO2	√	√	√	√	√
Dolomite	CaCO3.MgCO3	√	--	√	√	√
Microcline	KAlSi3O8	--	√	√	√	√
Kaolinite	Al2Si2O5(OH)4	√	√	√	√	√
Rutile	TiO2	√	--	--	--	--
		Trace Uranium Minerals				
Uraninite	UO2	√	--	√	√	√
Coffinite	U(SiO4)1−x(OH)4x	√	√	--	√	--
Andersonite	Na2Ca(UO2)(CO3)3 · 6H2O	--	√	√	--	--
Torbernite	Cu(UO2)2(PO4)2 • 12H2O	--	√	--	√	√
Tyuyamunite	Ca(UO2)2V2O8·(5-8)H2O	--	--	√	√	√
Carnotite	K2(UO2)2(VO4)2·3H2O	--	√	√	--	--
Uranophane	(Ca(UO2)2(SiO3OH)2·5H2O)	√	√	√	√	--
Schoephite	(UO2)8O2(OH)12•12(H2O)	√	--	--	--	--
Autunite	Ca(UO2)2(PO4)2·10–12H2O	√	√	√	√	√

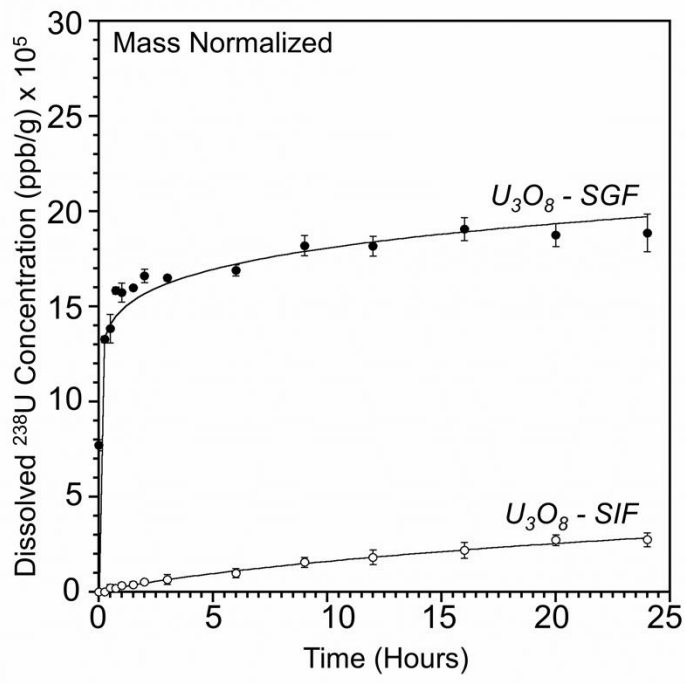

Figure 3. 4: The mass normalized dissolution of uranium from U_3O_8 in SGF (closed marker) and SIF (open marker)

The leaching of uranium in the two simulated gastrointestinal fluids was first investigated with the NIST U_3O_8 standard reported in the **Figure 3.4**. The obtained dissolution of U in simulated gastric fluid (SGF) is (18.87 ± 0.99) x 10^5 ppb/g, whereas that of SIF was (2.75 ± 0.36) x 10^5 ppb/g. The average rate of dissolution of U was calculated using the data collected within the first hour of reaction. They are 15.7 x 10^5±0.5 x 10^5 μg $L^{-1}g^{-1}$ h^{-1} and 5.2 x 10^4 ± 0.8 x 10^4 μg $L^{-1}g^{-1}h^{-1}$, respectively, for SGF and SIF solutions **(Table 3.4)**. The higher dissolution of uranium in the SGF solution than in the SIF solution was expected because the pH of the SGF solution (1.6) is lower than that of SIF solution (6.5). Minerals become more soluble in acidic environments than in basic environments because of the proton-promoted mechanism.[117, 118] However, pH plays a vital role in uranium complexation and in speciation and precipitation reactions, therefore, depending on the sample/fluid composition, the solubility trends can be different.[118-120]

Table 3. 4: The average rates of U dissolution and the %U dissolved upon 24-hour exposure.

Sample	Averaged rates of U dissolution for 1st 1 hours ($\mu g\ L^{-1} g^{-1}\ h^{-1}$)		%U dissolved upon 24-hour exposure	
	SGF	**SIF**	**SGF**	**SIF**
U_3O_8	$(15.7\pm0.5) \times 10^5$	$(5.2\pm0.8) \times 10^4$	22.19	3.24
St Anthony Sediments	$(36.0\pm0.8) \times 10^2$	415.5±35.4	6.38	1.52
St Anthony Rocks	$(2.0\pm0.4) \times 10^5$	$(1.4\pm0.2) \times 10^4$	90.63	20.84
Site K	27.4±2.8	312.1±60.2	0.16	2.79
Site L	15.8±1.6	29.9±3.3	0.51	0.58
Site M	57.0±0.9	40.8±2.4	1.15	2.19

In the next step, the uranium dissolution capacity from the five different natural dust and sediment samples was investigated. **Figure 3.5** represents the mass normalized dissolutions of U from different sample sites in both SGF and SIF fluids. The dissolution of uranium by each fluid varies for each sample site, and it varies between the two fluids for a given site. The rate of uranium dissolution in SGF follows as St. A. R> St. A. S> Site M> Site K> Site L, whereas for SIF, St. A. R> St. A. S> Site K> Site M> Site L. These differences in dissolution within the same fluid can arise for several reasons such as particle sizes, surface area, available %U in particles, and their mineralogy. In an attempt to eliminate the impacts from surface area and particle sizes, the observed extent of dissolutions was normalized to their specific surface area (**Figure 3.6**). However, the observed trends remained the same.

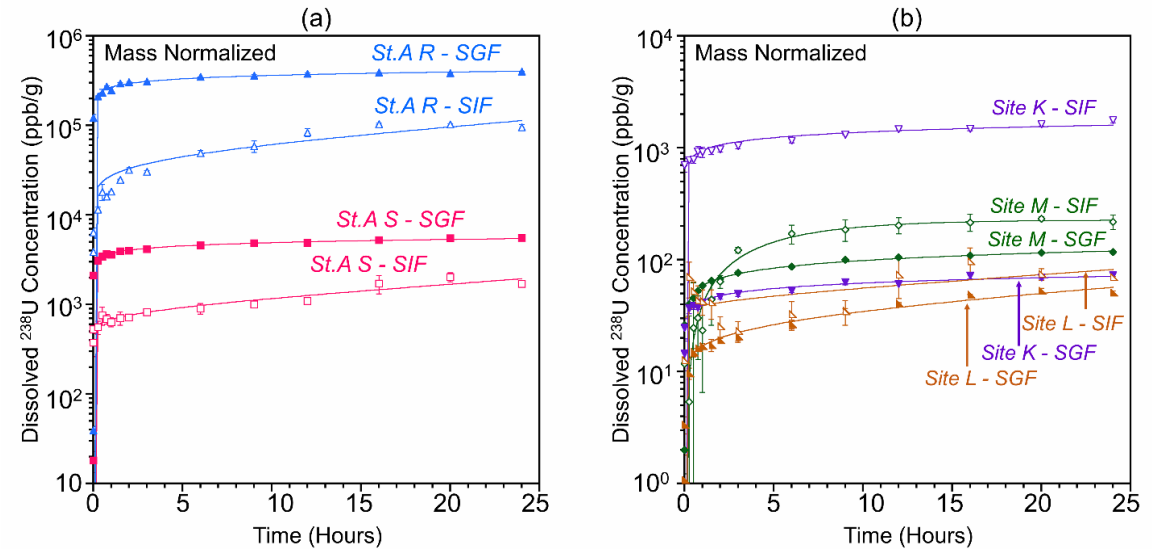

Figure 3. 5: The mass normalized dissolutions of uranium from natural dust and sediment samples in SGF (closed markers) and SIF (open markers).

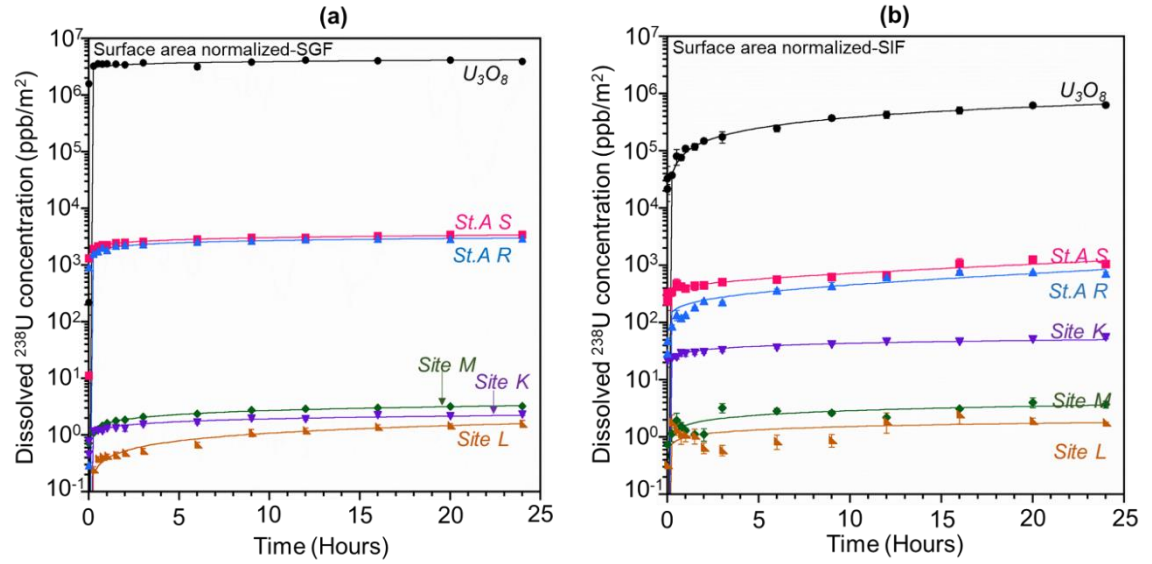

Figure 3. 6: The surface-area-normalized dissolutions of uranium from natural dust and sediment samples in (a) SGF solution and (b) SIF solution.

Therefore, the extent of dissolution was further normalized to the total uranium present in each sample (**Figure 3.7**). Following these normalizations, the extent of U dissolution in both fluids was still significantly different and can be attributed to factors such as compositional and mineralogical differences in these dust and sediment samples. The %U dissolved in SGF solution after exposure are 6.38%, 90.63%, 0.16%, 0.51%, and 1.15% for St. A. sediment, St. A. rock, Sites K, L, and M, respectively, whereas those in SIF solution are 1.52%, 20.84%, 2.79%, 0.58%, and 2.19%, respectively (**Table 3.4**). The rate of uranium dissolution as calculated from the first hour shows higher initial rates in

the SGF solution than SIF solution for St. A. R., St. A. S., and Site M, whereas Sites K and L have higher initial rates of U dissolution in SIF solution than SGF solution (**Table 3.4**).

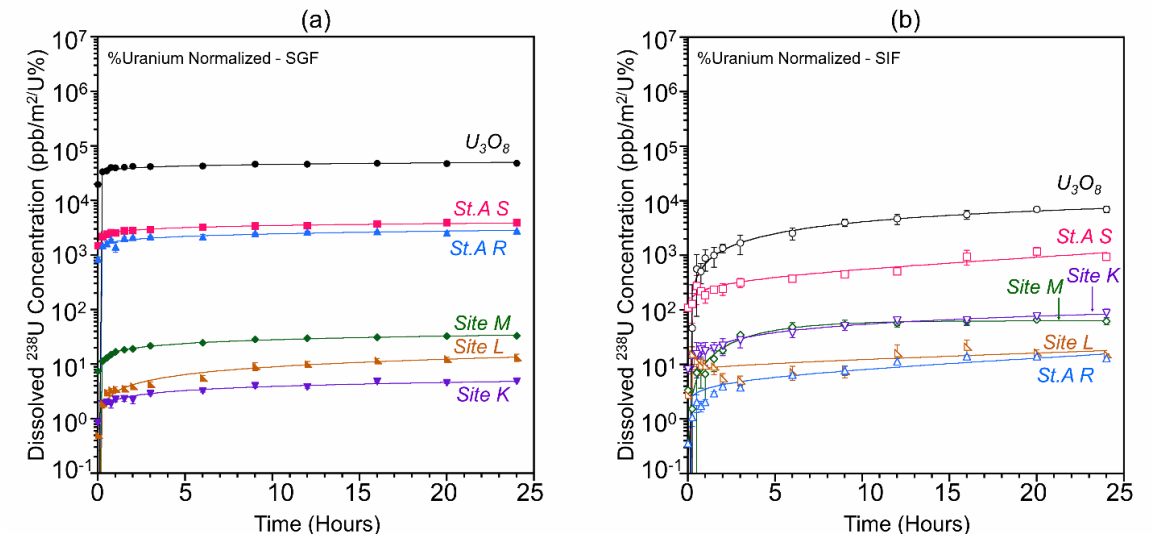

Figure 3. 7: The %U normalized dissolutions of uranium from U_3O_8 and natural dust and sediment samples in (a) SGF (closed markers) and (b) SIF (open markers).

Furthermore, unlike for U_3O_8, the samples from sites K, L, and M dissolved more uranium in the SIF solution than SGF solution. However, the samples from the St. Anthony mine (sediment and rock samples) dissolved more in SGF solution than in SIF solution, similar to U_3O_8. The ratio of dissolved U in SGF to SIF was calculated and added to the **Table 3.5**. The samples from the St. Anthony mine also showed similar dissolution trends to U_3O_8 in previous studies with simulated lung fluids.[2] The post-pH analysis added to **Table 3.6** revealed that the changes in the pH after the reaction were slight, and it was attributed to the differences in the amount of dolomite present.

Table 3. 5: The ratio of %U normalized dissolved U in SGF to SIF after 24 hours of dissolution experiment.

Sample	Dissolution ratio after 24 hours SGF/SIF
U3O8	6.85
St.A. S	4.20
St.A. R	4.35
Site K	0.06
Site L	0.88
Site M	0.53

Table 3. 6: Final pH (after 24 hours passed) of the dust-treated SGIF Solutions. The initial pH of the SGF solution is 1.60 and that of the SIF solution is 6.50.

Sample	**Final pH**	
	SGF	SIF
U3O8	1.46 ± 0.05	6.42 ± 0.09
STAS	1.89 ± 0.06	6.02 ± 0.16
STAR	1.63 ± 0.05	5.93 ± 0.16
Site K	1.63 ± 0.04	6.28 ± 0.04
Site L	1.69 ± 0.06	6.12 ± 0.07
Site M	1.68 ± 0.09	6.23 ± 0.09

Many studies suggest that the dissolved uranium in the gastrointestinal tract can cause immune suppressions and can be linked to the autoimmunity, cardiovascular, and neurological disorders and cancers observed among the populations living in the vicinity of uranium mines.[48, 98, 99, 121] Therefore, the dust-treated GIT solutions were analyzed for dissolved uranium speciation. The colorimetric analysis of the Uranyl-Curcumin-Triton-X System was used to qualitatively determine (orange coloration) the presence of the uranyl cation (UO_2^{2+}). The dust- and sediment-treated SGIF did not develop a strong orange coloration, which would indicate the presence of UO_2^{2+}. This differs from our previous studies in simulated lung fluids where the uranyl cation was calorimetrically detected.[2] This is likely because of smaller quantities of dust in SGIF solutions which was not enough to show a visible color development. Therefore, to confirm the presence of uranyl cation in dust-treated SGIF solutions, a higher quantity of dust (~50 mg in 3 mL of fluid) was treated for 24 hours using the same dissolution conditions, and the uranyl cation was identified as a dissolved uranium species (**Table 3.7 and Figure 3.8**). **Figure 3.9** indicates no matrix effect from the media. Therefore, uranium constituents on inhaled dust particles may react with gastrointestinal fluids upon entering the digestive tract and form uranyl cation and other complex dissolved uranium species.

Table 3. 7: Masses of natural dust and sediment samples used in uranyl cation detection.

Samples	Amount in 3 mL of SGF (mg)	Amount in 3 mL of SIF (mg)
U3O8	50.21	50.16
St. Anthony Sediments	50.22	50.89
St. Anthony Rock	50.53	50.51
Site K	50.15	51.17
Site L	47.19	50.09
Site M	50.13	50.67

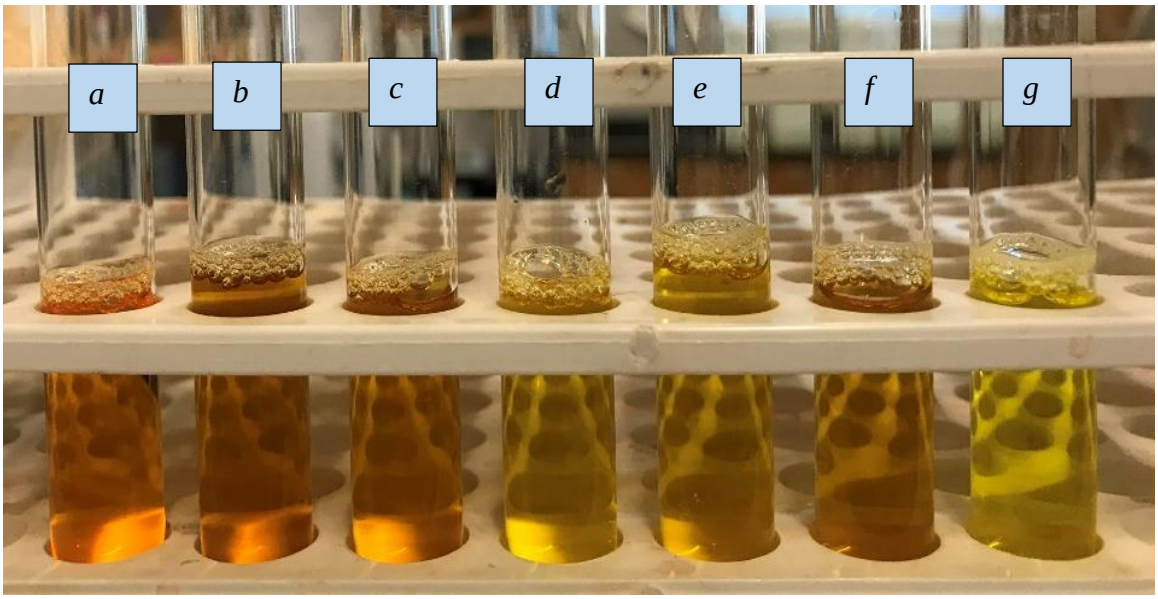

Figure 3. 8: Orange coloration for Uranyl-Curcumin-Triton-X experiment for (a) U_3O_8, (b) St. Anthony sediment, (c) St. Anthony rock, (d) Site K, (e) Site L, and (f) Site M, while (g) is the Blank**.**

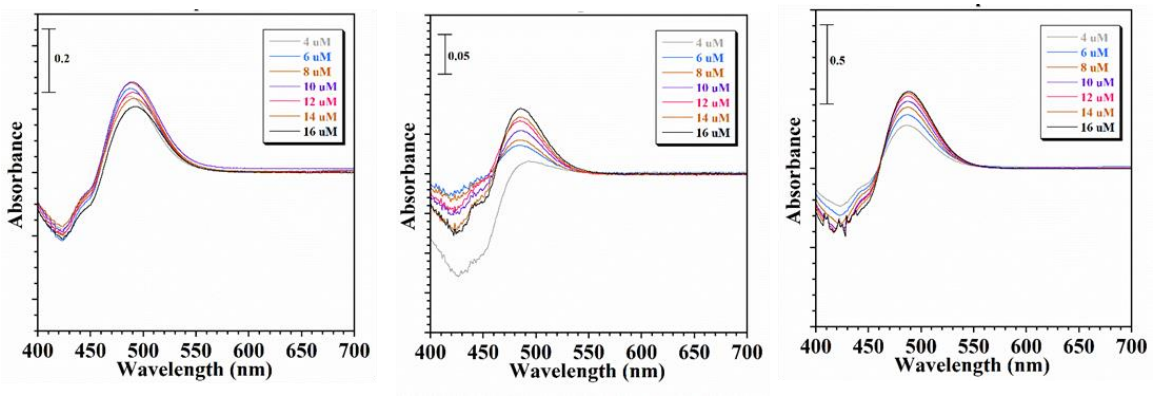

Figure 3. 9: UV-VIS scanned spectra of uranyl-curcumin-Triton-x system in (a) SGF, (b) SIF, & (c) water.

3.5.3 Computational Calculations of Uranium Solubility in Simulated Gastrointestinal Fluids and Impact of Particle Mineralogy

To better understand the impact of mineralogy on the U dissolution process in the SGIF, a series of computational calculations were conducted to determine the dissolved U constituents. **Figure 3.10** indicates the ratio of the calculated equilibrium U concentrations for each natural sample in SGF and SIF solutions. Similar to bench experiments, the computational calculations suggest that both St. A Rock and St. A Sediment samples are more soluble in the SGF solution than in the SIF solution. In contrast, samples from Sites K, L, and M are more soluble in the SIF solution than in the SGF solution. These concentrations are St. A. Rock (5.8130×10^{-1} M), St. A. Sediment (4.3100×10^{-3} M), Site L (9.2700×10^{-4} M), Site M (7.3000×10^{-4} M), and Site K (7.0000×10^{-4} M) for the SGF solution. The concentrations for the SIF solution are St. A. Rock (5.5430×10^{-1} M), St. A. Sediment (9.0000×10^{-4} M), Site M (7.4000×10^{-3} M), Site K (4.0000×10^{-3} M), and Site L (7.5000×10^{-3} M). Further, the speciation analysis suggests that practically all dissolved uranium is in the U(VI) oxidation state and represents a mixture of various aqueous uranyl complexes such as uranyl carbonate (e.g., $[UO_2(CO_3)_3]^{4-}$ or $[UO_2(CO_3)_2]^{2-}$) or uranyl phosphate (e.g., $[UO_2(HPO_4)_2]^{2-}$) complexes. Deposited uranium or solid uranium has shown affinity toward carbonate and bicarbonate in different environments.[122] The carbonates in this reaction can be derived from either dolomite or andersonite in the samples. In contrast, phosphate can be derived from uranium-phosphate minerals such as autunite or torbernite, as well as from the lecithin in the reaction medium. The concentration of phosphate can control the speciation of dissolved uranium.[118] Therefore, it is recommended to consider phosphate mineralogy and speciation in future solid-uranium inhalation and digestion studies. Additionally, both SGF and SIF solutions, when reacted with St. A. R., contained $[(UO_2)_2(OH)_2]^{2+}$ as another major dissolved uranium species. All solutions contained un-complexed UO_2^{2+} and $[UO_2H_3SiO_4]^{+}$ as minor components.

After modeling the experimentally observed SGF/SIF ratio of dissolved uranium concentrations, we calculated the uranium solubility for each mineral phase to understand their behavior in the simulated gastrointestinal fluids. All uranium minerals tested except andersonite favored higher dissolution in SGF over SIF solutions. The calculated

concentrations in mol/dm^3 for SGF vs. SIF solutions are autunite (2.00 x 10^{-2}, 5.53 x 10^{-4}), torbernite (2.00 x 10^{-2}, 2.29 x 10^{-4}), uranophane (1.91 x 10^{-2}, 5.93 x 10^{-6}), U_3O_8 (1.44 x 10^{-2}, 8.61 x 10^{-6}), schoepite (1.00 x 10^{-2}, 1.93 x 10^{-5}), andersonite (6.76 x 10^{-3}, 9.87 x 10^{-3}), tyuyamunite (6.18 x 10^{-3}, 7.49 x 10^{-6}), carnotite (4.70 x 10^{-3}, 8.51 x 10^{-6}), coffinite (1.99 x 10^{-9}, 1.88 x 10^{-11}), and uraninite (1.99 x 10^{-9}, 1.89 x 10^{-11}). As revealed from the calculations, coffinite and uraninite are extremely insoluble in the tested conditions. Further, the lower dissolutions observed in the SIF solution than in the SGF solution are clear evidence that experimentally observed dissolution trends are an outcome of combined sample mineralogy rather than the singular impact of one mineral. The speciation analysis suggested that un-complexed UO_2^{2+} is the primary dissolved uranium species when carbonate and phosphate sources are missing.

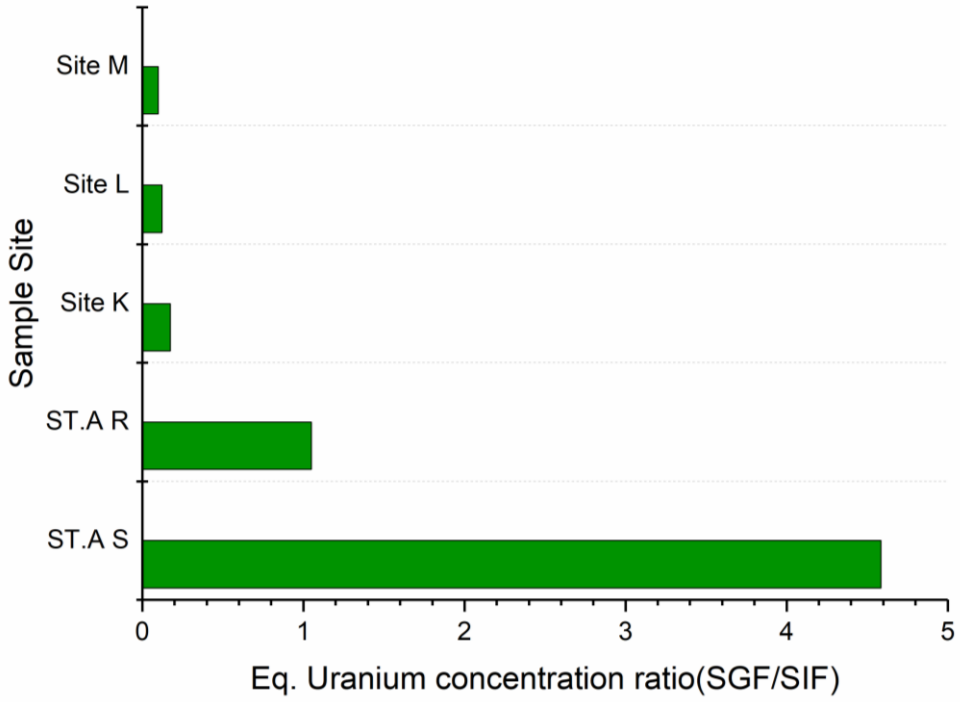

Figure 3. 10: SGF/ SIF ratio of calculated equilibrium U concentrations.

As kaolinite was identified in all the analyzed dust and sediment samples, each single-phase uranium mineral was combined with 1.000 mol of kaolinite, and dissolved uranium concentrations were recalculated. Kaolinite ($Al_2Si_2O_5(OH)_4$) is a naturally occurring common clay mineral, a 1:1 layered aluminosilicate structure consisting of alternating silica and alumina sheets.[123, 124] In aqueous solutions, kaolinite surface hydroxylates and participates in surface reactions.[125] Upon adding kaolinite, the SGF/SIF ratio was decreased for all the minerals (**Figure 3.11 & Table 3.8**) except andersonite. Further, these data implied that the presence of kaolinite could significantly change the extent of uranium dissolution from these minerals inside the human gastrointestinal tract. Then, a similar recalculation was conducted for each uranium mineral mixing with 1.000 mol of microcline. Which is a potassium-rich alkali feldspar mineral ($KAlSi_3O_8$) identified in all the samples except the St. Anthony sediment sample. The addition of microcline decreased the SGF/SIF ratio for all tested minerals. Further, the

SGF/SIF ratio dropped below 1 for torbernite, coffinite, and uraninite mixtures with microcline, showing the presence of microcline greatly favors higher solubility in SIF solution. Overall, non-U-minerals such as kaolinite and microcline can impact the dissolution of uranium minerals in simulated gastrointestinal fluids.

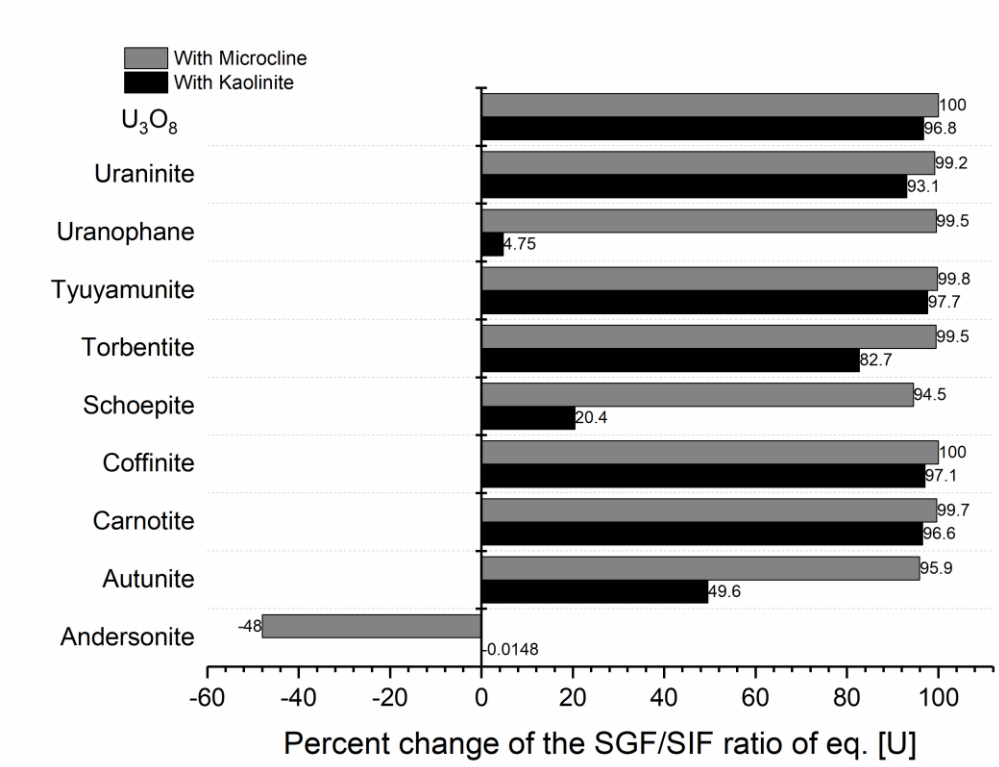

Figure 3. 11: Percent changes of single-phase uranium solubility ratios of SGF/SIF as a function of either kaolinite or microcline. The positive numbers indicate a decrease in concentration, while the negative numbers indicate an increase in concentration.

Table 3. 8: Calculated equilibrium U concentrations

Dissolved [U]/ M									
	Without Kaolinite			With Kaolinite			With Microcline		
Mineral	SGF	SIF	SGF/SIF	SGF	SIF	SGF/SIF	SGF	SIF	SGF/SIF
Andersonite	6.76E-03	9.87E-03	0.68	6.76E-03	9.87E-03	0.68	1.00E-02	9.87E-03	1.01
Autunite	2.00E-02	5.53E-04	36.17	1.02E-02	5.58E-04	18.23	8.04E-04	5.43E-04	1.48
Carnotite	4.70E-03	8.51E-06	552.50	1.67E-04	8.89E-06	18.97	2.08E-06	1.12E-06	1.86
Coffinite	1.99E-09	1.88E-11	106.35	5.84E-11	1.87E-11	3.12	1.62E-11	2.46E-09	6.6E-03
Schoepite	1.00E-02	1.93E-05	518.14	9.99E-03	2.42E-05	412.42	2.44E-04	8.65E-06	28.26
Torbentite	2.00E-02	2.29E-04	87.41	3.48E-03	2.30E-04	15.10	2.61E-04	5.99E-04	0.43
Tyuyamunite	6.18E-03	7.49E-06	824.70	1.52E-04	7.96E-06	19.06	1.75E-06	1.10E-06	1.60
Uranophane	1.91E-02	5.93E-06	3216.34	1.91E-02	6.22E-06	3063.69	9.24E-05	6.22E-06	14.86
U3O8	1.44E-02	8.61E-06	1676.54	1.05E-03	9.08E-06	115.22	9.57E-06	7.32E-07	13.079
Uraninite	1.99E-09	1.89E-11	105.39	5.84E-11	1.72E-11	3.40	1.62E-11	2.46E-09	6.6E-03
	For Natural dust and sediment samples								
STAS	4.31E-03	9.41E-04	4.585371	--	--	--	--	--	--
STAR	5.81E-01	5.54E-01	1.04871	--	--	--	--	--	--
SiteK	6.95E-04	3.98E-03	0.174768	--	--	--	--	--	--
SiteL	9.24E-04	7.52E-03	0.123179	--	--	--	--	--	--
SiteM	7.29E-04	7.37E-03	0.098955	--	--	--	--	--	--

Figure 3.12 and **Figure 3.13** represents the dissolved uranium ratio in each fluid with and without kaolinite or microcline. The solubility of uranium in the SGF solution from all the tested minerals, except for andersonite and uranophane, decreases upon adding kaolinite. In contrast, with the addition of microcline, the uranium solubility decreases for all minerals except andersonite. The solubility of andersonite and uranophane in the SGF solution was not affected by the addition of kaolinite. The decrease in solubility could be due to the ability of hydroxyl groups in surfaces to react with protons in the acidic SGF solution and the ability of metal centers to interact with anions, thereby effectively decreasing the proton-promoted uranium dissolution. However, the solubility of andersonite, a uranium carbonate mineral, in the SGF solution was increased with the addition of microcline.

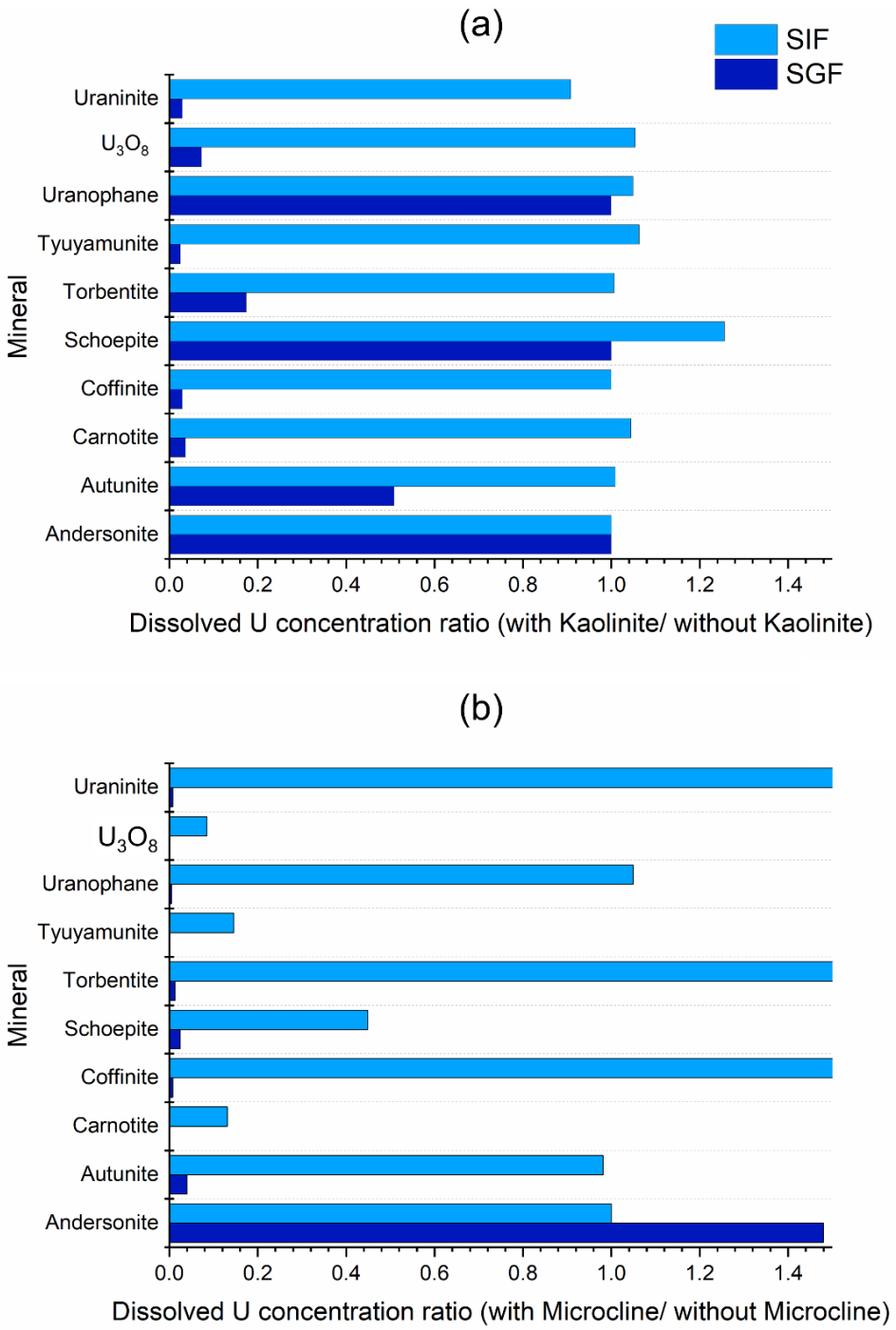

Figure 3. 12: Dissolved U concentration ratios for each mineral in each SGIF. (a) The ratio of U dissolution when kaolinite is present to the U dissolution when kaolinite is not present (b) The ratio of U dissolution when microcline is present to the U dissolution when microcline is not present.

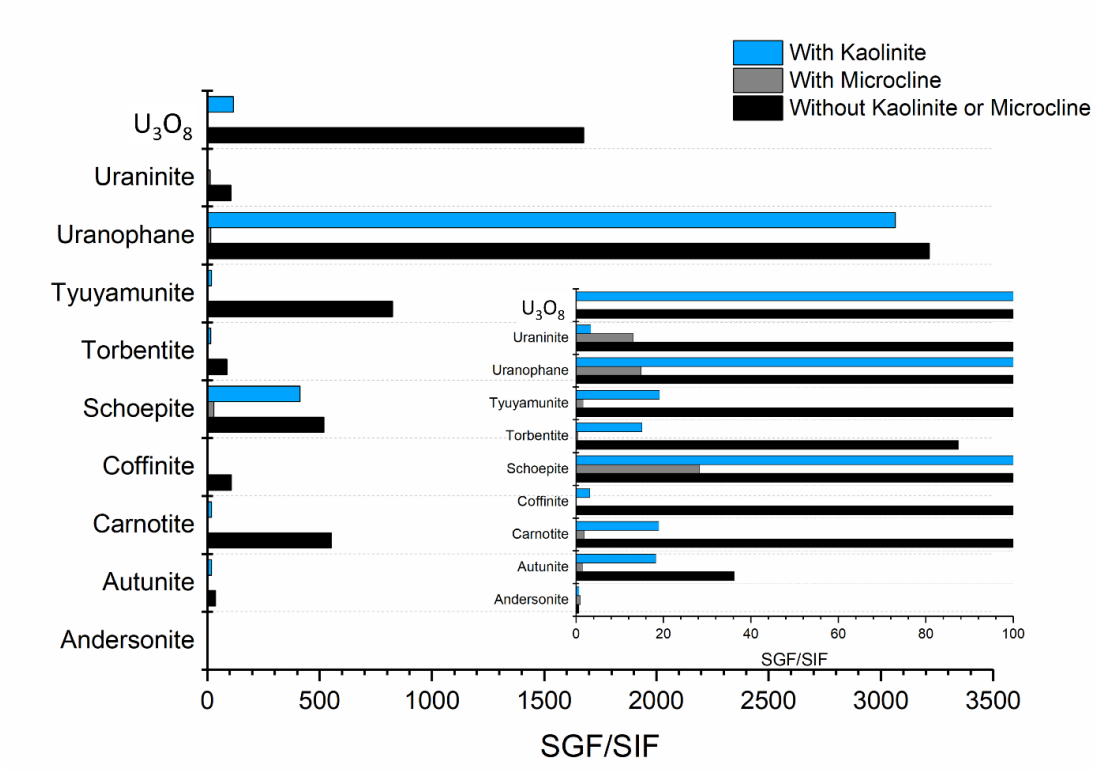

Figure 3. 13: Single-phase uranium solubility ratio of SGF/SIF (a) with and without kaolinite (b) percent decrease in SGF/SIF ratio as a f(Kaolinite).

Unlike in the highly acidic SGF solution (pH = 1.6), the uranium solubility in the SIF solution (pH = 6.5) showed mixed trends with the addition of either kaolinite or microcline. While andersonite solubility was not affected by the presence of kaolinite, the uranium solubility of both uraninite and coffinite decreased in the SIF solution. All the other tested minerals showed enhancements in uranium solubility. The dissolved uranium concentrations in SIF solutions were increased for coffinite, torbernite, uranophane, and uraninite in the presence of microcline, whereas all other minerals except andersonite showed a decrease in dissolved uranium concentration. The calculated trends imply that the pH and composition of the solution, along with the mineralogy of particles, affect uranium dissolution. It is important to note that in the current study, the impact of kaolinite or microcline on uranium dissolution is evident when the kaolinite to uranium mineral ratio (microcline to uranium mineral ratio) is 1.000:0.001. This ratio was used to simulate the presence of excess kaolinite or microcline in the system. Therefore, it is possible that uranium solubility can further change by varying the ratio of these minerals. Additionally, the higher uranium solubility in SIF solution for the samples from sites K, L, and M than in SGF solution may be attributed to certain mineralogical and compositional features observed, such as the presence of tyuyamunite and a higher percentage of autunite. Further,

the variable quantities of torbernite and carnotite in these samples can play a role in enhanced U leaching in SIF solution.

3.6 Conclusion

In the current study, the solubility of uranium from relatively larger-sized inhaled particles in human gastrointestinal tract conditions was investigated using simulated gastric and intestinal fluids in the fasted state. The uranium from these dust and sediment samples collected near Jackpile and St. Anthony mines in NM might solubilize in human gut conditions, potentially leading to subsequent absorption. The samples from the sites St. A. (sediment and rock) are more soluble in human stomach-like conditions (as simulated by SGF), whereas samples from sites K, L, and M are more soluble in human intestine-like conditions (as simulated by SIF). Further, through experimentally obtained mineralogical information and computational geochemical calculations, we reported that these solubility differences are partly due to the mineralogical differences. The combined mineralogy and the presence of non-uranium minerals (kaolinite and microcline) influence the extent of uranium dissolution from these minerals. The most prevalent oxidation state of dissolved uranium was computationally determined as +6. Therefore, we report that the solubility of solid uranium in the human digestive tract after inhalation is possible and that the extent of uranium concentration and its speciation depends on site-specific mineralogy. Thus, these factors should be weighed in the toxicological assessments. Further, considering the scarcity of studies on the impact of dissolved uranium on gut microbiota, the authors suggest furthering research to understand how human gut microbiota will interact with the uranium contained in inhaled dust.

3.7 Acknowledgment

Research reported in this publication was partially supported by an Institutional Development Award (IDeA) from the National Institute of General Medical Sciences of the National Institutes of Health under grant number P20GM103451 and NM EPSCoR under the National Science Foundation/EPSCoR Award No. IIA-1301346. The authors would also like to thank https://smart.servier.com/ for granting permission to use their human body images in the graphical abstract at no cost.

Permission

Reprinted (adopted) and does not require specific permission for reprint in the dissertation.

E. HETTIARACHCHI, M. DAS, D. CADOL, B. A. FREY AND G. RUBASINGHEGE, THE FATE OF INHALED URANIUM-CONTAINING PARTICLES UPON CLEARANCE TO GASTROINTESTINAL TRACT. ***Environ. Sci.: Processes Impacts*****, 2022**, 24, 1257 – 1266.

CHAPTER 4 [2]

CHARACTERIZATION AND TOXICITY ANALYSIS OF LAB-CREATED RESPIRABLE COAL MINE DUST FROM THE APPALACHIANS AND ROCKY MOUNTAINS REGIONS

4.1 Abstract

Coal mine workers are continuously exposed to respirable coal mine dust (RCMD) in workplaces, causing severe lung diseases. RCMD characteristics and their relations with dust toxicity need further research to understand the adverse exposure effects of RCMD. The geographic clustering of coal workers' pneumoconiosis (CWP) suggests that RCMD in the Appalachian region may exhibit more toxicity than in other geographic regions, such as the Rocky Mountains. This study investigates the RCMD characteristics and toxicity based on geographic location. Dissolution experiments in simulated lung fluids (SLFs) and in vitro responses were conducted to determine the toxicity level of samples collected from five mines in the Rocky Mountains and Appalachian regions. Dust characteristics were investigated using Fourier-transform infrared spectroscopy, scanning electron microscopy, the BET method, total microwave digestion, X-ray diffraction, and X-ray photoelectron spectroscopy. Inductively coupled plasma mass spectrometry was conducted to determine the concentration of metals dissolved in the SLFs. Finer particle sizes and higher mineral and elemental contents were found in samples from the Appalachian regions. Si, Al, Fe, Cu, Sr, and Pb were found in dissolution experiments, but no trends were found indicating higher dissolutions in the Appalachian region. In vitro studies indicated a proinflammatory response in epithelial and macrophage cells, suggesting their possible participation in pneumoconiosis and lung disease development.

4.2 Introduction

Respirable coal mine dust (RCMD) refers to the mixture of airborne particles present in the air of surface and underground coal mines coming from different sources, such as rock breakage, intake air, rock dusting, diesel equipment, and any activity involving abrasion.[29, 126, 127] These particles are small enough to reach the deepest region of the human lungs, causing damage to the lung tissues.[18, 126, 128, 129] Several researchers have described RCMD as those particles that are smaller than 10 μm and/or with a mean

[2] Chapter is reprinted/adopted from authors own published work "Salinas, V.; Das, M.; Jacquez, Q.; Camacho, A.; Zychowski, K.; Hovingh, M.; Medina, A.; Rubasinghege, G.; Rezaee, M.; Baltrusaitis, J.; Fairley, N.; Roghanchi, P. Characterization and Toxicity Analysis of Lab-Created Respirable Coal Mine Dust from The Appalachians and Rocky Mountains Regions. **Minerals, 2022**, 12, 898" does not require specific permission for reprint in the dissertation.

particle size of 4 μm (aerodynamic diameter) [18, 35, 126, 128] but some others restrict the respirable fraction only to the one smaller than 4 μm.[127, 129]

Coal mine workers are frequently at risk for RCMD inhalation. A portion of dust may be retained by the mask (if appropriately worn) and in the upper part of the respiratory system. Large particles may be eliminated via mucociliary clearance.[130] Smaller particles penetrate deep into the lungs and are deposited in the alveolar region. A portion of the inhaled particles stay in the alveoli since the body's defense mechanisms cannot expel them.[2, 35] Long-term exposure to RCMD can lead to pulmonary diseases such as coal workers' pneumoconiosis (CWP), mixed dust pneumoconiosis, dust-related diffuse fibrosis (DDF), progressive massive fibrosis (PMF), emphysema, chronic bronchitis, and silicosis. All these diseases are irreversible and may result in serious lung injuries and death.[18]

During the last decades, tremendous efforts have been made to reduce miners' exposure to RCMD. However, lung diseases caused by RCMD still remain a significant concern in the coal mining industry. In the early 2000s, an increase in the prevalence and severity of CWP, especially in central Appalachia, was observed.[18, 29, 55] The data indicated that coal miners in the Appalachia and Interior regions are at a higher risk of CWP prevalence in comparison with the Western region.[126]

The number of CWP cases in the US by state and county (from 1986 to 2018) shows hot spot areas in the Appalachian region, with a higher number of cases in West Virginia, Kentucky, Virginia, and Pennsylvania.[126] Additionally, an analysis of the chest radiographs of underground coal miners reported from 1996 to 2002 found CWP in 3% of the miners evaluated. From the miners that showed CWP, 35.4% presented rapidly progressive CWP, and 14.8% evidenced PMF. Furthermore, a proportion between 61.5% and 80% of evaluated miners with rapidly progressive CWP was found in different counties in West Virginia, Kentucky, Virginia, and Pennsylvania, suggesting a cluster along the Appalachian region.[131] Similar observations that suggest a higher incidence of lung diseases in the Appalachian region have been obtained by NIOSH when examining chest radiographs from the Coal Workers' Health Surveillance Program (CWHSP).[18]

A study by Rahimi et al. investigated the geographic location of an underground mine as a contributing factor in RCMD and respirable crystalline silica (RCS) concentrations.[132] The study used the Mine Safety and Health Administration (MSHA) database between 1989 and 2018, dividing the data into Appalachia, Interior, and Western regions. This study determined that geographic location contributes to RCMD concentrations in underground mines (Interior vs. Western) and RCS concentrations in surface and underground mines (Appalachia vs. Western). Further research into the key differences in coal dust characteristics from different regions was recommended.[132]

The higher rates of CWP cases in the Appalachian region have been linked to the thinner seams usually found in the mines from this region.[29, 133] Several studies have demonstrated a substantially higher RCS content in dust samples from thin coal seam mines as a result of host rock cutting during coal extraction.[29, 126]. Silica was classified as a "Class I Human Carcinogen" by the International Agency for Research on Cancer and has

been pointed to as the main cause of silicosis.[18, 55] Long-term exposure to RCS is also known to cause chronic obstructive pulmonary disease (COPD) and lung cancer.[134]

Although several studies have focused on the RCMD characterization,[29, 35-37] investigation of the toxicity of RCMD based on the elements and their influence on the inflammatory response of the lungs remains scarce. However, investigation of RCMD characteristics and the level of toxicity will significantly help to better understand the true reasons for the higher prevalence of lung diseases in the Appalachian region.

This study aims to characterize and analyze the toxicity of dust particles from different regions in the US. The samples for this study were collected from five mines located in the Appalachian region, the area of interest, and in the Rocky Mountains, a different basin and coal occurrence zone in the US. This was to have two regions for comparison. The toxicity analysis of dust particles was conducted based on the elements that dissolve in simulated lung fluids (SLF) and the inflammatory response they produce. For this purpose, dissolution experiments in simulated lung fluids (SLF) and in vitro responses were conducted. The characterization of dust samples was performed using Fourier transform infrared spectroscopy (FTIR), a scanning electron microscope (SEM), the BET method, microwave total digestion, X-ray diffraction (XRD), and X-ray photoelectron spectroscopy (XPS) to obtain the functional groups, particle size distribution, specific surface area, elemental content, mineral composition, and surface composition of the samples, respectively. The dissolution experiment exposed dust samples to two SLFs (Gamble's solution and artificial lysosomal fluid), and the concentrations of the metals dissolved after 24 h were obtained using inductively coupled plasma mass spectrometry (ICP-MS). For in vitro responses, HL-60, A549, and THP-1 cells were exposed to different concentrations of RCMD to evaluate the change in protein expression. Results were analyzed to find trends related to the geographic location to link dust samples' characteristics and toxicity to the higher incidence of lung diseases in the Appalachian region.

4.3 Materials and Methods

4.3.1 Bulk Sample Collection and Preparation

Bulk samples used in this study were collected from 5 mines: 3 mines from the Appalachian region and 2 from the Rocky Mountains. The purpose of bulk sample collection was to create a representative collection of materials in a mine that are aerosolized and subsequently inhaled by the miner during their shift. Samples were collected from the coal seam of the working face in order to collect material that closely matches the excavated coal rock.

Mines 1 and 2 correspond to the samples collected from the Western regions, and Mines 3, 4, and 5 to the ones collected from the Appalachian region. It is essential to mention that Mine 1 is a surface mine; the rest are from the underground room and pillar mines. The descriptions of the mines' location, type, and methods are shown in **Table 4.1**.

Table 4. 1: Overall information of the samples collected for this research.

Region	Mine ID	Type	Mining Method	Coal Rank	Seam Height	Ash (%)	Volatile Matter (%)	Sulfur (%)
Rocky Mountains	Mine 1	S *	Open cut	Sub-bituminous	Low seam	16.90	32.00	1.08
	Mine 2	UG **	Room and pillar	Bituminous	High seam	11.64	33.39	0.55
Appalachians	Mine 3	UG	Room and pillar	Sub-bituminous	Low seam	5.85	16.26	1.07
	Mine 4	UG	Room and pillar	Sub-bituminous	Low seam	11.28	15.43	1.17
	Mine 5	UG	Room and pillar	Bituminous	High seam	N/A ***	N/A	N/A

* S: Surface; ** UG: Underground; *** N/A: Not available.

For the sample preparation, the bulk sample size was initially reduced with a jaw crusher or mortar and pestle, depending on the initial size of the sample, until reaching 100%, passing the U.S.A. standard sieve No. 6 (3.35 mm, ASTM E11). The resulting sample was ground with a 755RMV jar mill of 9.5 inches in diameter and 8.5 in height, using media of zirconia 1/2"×1/2" radius end cylinder, magnesia stabilized. First, the material was ground for 6 h, and sieved using the U.S.A. standard sieve No. 120 (opening of 125 µm) to remove the big particles that the mill could not reduce. Then, the material passing the sieve was ground for 6 more hours. To obtain a larger fraction of particles smaller than 10 µm, the material was ground additionally with a RETSCH XRD-Mill McCrone, which preserves the structure of the coal samples in the reduction process. The grinding was conducted for 5 min in a 4-step process, loading only 2 mL of sample per round, and using agate as media. Finally, the samples less than 10 µm fraction (mass mean aerodynamic diameter) were separated using a next-generation cascade impactor (NGI, model 170 NGI, MSP Corporation, Shoreview, MN, USA) with an attached aerolizer and gravimetric stages. Dust samples were weighed and loaded into hydroxypropyl methylcellulose capsules and drawn through an induction port using a pump Copley Scientific (Copley Scientific, Nottingham, UK) operated at a flow rate of 60 L/min for 4 s. The fractions less than 10 µm were collected from multiple stages and used for further studies.

4.4 Dust Characterization

Several characterization techniques were used to study the initial conditions and different characteristics of the dust particles, such as particle size distribution, specific surface area, functional groups, and mineral, elemental, and surface composition. Later, results were compared to observe if they were any differences or trends among the different regions studied.

4.4.1 SEM

A NOVA-Nano-SEM-450 from the Center for Integrated Nanotechnologies (CINT) was used to collect SEM images to verify the particle size from the previous

separation and to obtain the particle size distribution in the samples. The images were analyzed for particle size using the software package ImageJ. An average of 80 particles were measured in width and length to plot histograms of the particle sizes for both dimensions. Particulate matter (PM) fractions were calculated using the width of the particles.

4.4.2 XRD

A PANalytical X'Pert Pro diffractometer (PANalytical B.V., Almelo, The Netherlands), equipped with a Cu Kα source and a fixed divergence silt of 0.25°, was used to determine the mineral components in the samples. The analyses were conducted in a 40 min program with a continuous scan of 0.008° step size, operating at 45 kV and 40 mA, with a 2θ scan range from 5° to 70° and a scanning time of 40 s/step. Raw data were analyzed with HighScore Plus software (Malvern Panalytical Ltd., Malvern, UK) with a minimum significance of 2 and restricted to the dataset of minerals.

4.4.3 Total Microwave Digestion

A high-performance microwave system from Milestone (model ETHOS UP, Shelton, CT, USA), was used for the total digestion. The system is equipped with infrared and direct contactless temperature sensors and two 950-Watt magnetrons for a total power of 1900 W, which can operate up to 230 °C and 100 bar. TFM vessels with highly resistant PEEK shields were used in a SK-15 rotor. The method used to digest the coal samples was the SK-PE-017, suggested by the manufacturer, which consisted in a two-step digestion for up to 200 mg of sample. The first step used 10 mL of HNO_3 with a program of 190 °C and 800 W/1200 W of power (for 3 or less vessels/4–8 vessels), using 10 min to reach the temperature and 15 min of standing time. The second step used 2 mL of HF with a program of 230 °C using 20 min to reach the temperature and 15 min of standing time. For both steps, 800 W was used when operating with 3 or less vessels and 1200 W when operating 4–8 vessels. The standard reference material (SRM) CLB-1 from the USGS was used for quality control.[95] After digestion, the resulting solution was filtered and dissolved with RO water up to complete 50 mL of solution. Finally, elemental content was measured with an inductively coupled plasma mass spectrometer (ICP-MS), using a 1:10 dilution.

ICP-MS used was an Agilent Technologies model 7900. For the samples from the microwave digestion, an HF-resistant set-up was used, equipped with a sapphire torch, a PFA spray chamber capable of cooling down up to 2 °C, and a PFA Scott-type concentric nebulizer. The following 29 elements were analyzed with the method: Li, Be, Mg, Al, Si, K, Ca, Ti, V, Cr, Mn, Fe, Co, Ni, Cu, Zn, As, Se, Sr, Mo, Ag, Cd, Sn, Sb, Ba, Tl, Pb, Th, and U. Limit of detection of the method for Mg, K, Ca, and Fe was around 100 ppb, for Mo 2 ppb, and for the rest of the elements 1 ppb.

4.4.4 BET

The surface area and the micro-pore of the dust samples were analyzed in a 92 points (52 points N_2 adsorption and 40 points desorption) Brunauer–Emmet–Teller (BET) isotherm using a Quantachrome Autosorb-1 instrument. Samples were outgassed for over 24 h at 150 °C before the analysis. The surface area was obtained using 7 N_2 adsorption

points from the linear region of the isotherm. The pore size analysis was performed using Quenched Solid Density Functional Theory (QSDFT), which considers the surface roughness and heterogeneity and offers a reliable pore size analysis for any unknown carbon sample.

4.4.5 XPS

X-ray photoelectron spectroscopy (XPS) data were recorded using SPECS instrument (SPECS, Berlin, Germany) equipped with Phoibos 1D-DLD hemispherical electron energy analyzer, and 0.3 mm entrance aperture, XR50MF aluminum K-α X-ray source operating at 100 W with m-FOCUS 600 X-ray monochromator, and in ultra-high vacuum (UHV) mode. Survey spectra were acquired using 100 eV pass energy, while high-resolution scans were acquired using pass energy of 20 eV. Low-energy electrons were used to neutralize the charge. Data processing was performed using CasaXPS software.[135] Charge calibration was performed using a 284.4 eV graphitic peak.[136] C1s spectrum peak fitted with synthetic components based on the literature data.[137] Elemental quantification was performed using relative sensitivity factors of 2.93 for O1s, and 1.0 for C1s with correction for the instrument transmission/escape depth applied.

4.4.6 FTIR

FTIR spectra of the dust samples were collected using a Nicolet iS50 series FTIR (Thermo Scientific™, Waltham, MA, USA) equipped with Ge-ATR crystal. The sample was prepared in a small centrifuge tube. Approximately 10 mg of coal dust was sonicated for 20 min in 1 mL of isopropyl alcohol (IPA) and transferred to the ATR crystal, followed by air drying, which left a thin layer of dust on the ATR crystal. Collected spectra were processed against the spectra of bare crystal, and only the processed spectra were reported. For each sample, FTIR analysis was performed for the parent dust sample before any dissolution experiment as well as after the dissolution in both GS and ALF. For this purpose, we recollected undissolved dust after the dissolution experiment using filtration and a hot plate to dry it.

4.5 Toxicity Analysis

The toxicity of dust samples was assessed throughout dissolution experiments to determine the metals dissolving in SLF and in vitro analysis to examine the inflammatory response.

4.5.1 Dissolution Experiment

Dissolution experiments in SLFs were carried out to analyze the elements that dissolved from the dust samples and were in contact with the SLF for 24 h. Gamble's solution (GS) and artificial lysosomal fluids (ALF) were used as simulated lung fluids following the preparation shown in **Table 4.2**.[2, 138] GS simulated the pulmonary surfactants secreted by cells in the interstices of the lungs, and ALF simulates the acid fluid in macrophages that are in charge of trap and eliminating foreign bodies.[130] To simulate body conditions, experiments were run in a dark room, double jacketed bottles were used to circulate water at 37 °C and keep the temperature constant, and the SLF were oxygenated for 5 min at a rate of 5 L/min before starting the experiments. Constant stirring at 1000 rpm

was provided during the experiments. Triplicates were conducted for each sample in each SLF. Totals of 100 mL of SLF and 20 mg of coal sample were used in each trial. Sample aliquots of 1.5 mL were collected from the bottles before adding the coal to the SLF, and right after adding the coal to set the 0 h. Then, samples were collected at 1 h, 3 h, 6 h, 9 h, 12 h, 18 h, and 24 h. After collection, SLF samples were centrifuged, filtered, and stored in a freezer until analyzed. The same ICP-MS with a standard set-up was used to determine the elemental content in the SLF dissolution. The standard set-up used a quartz torch, quartz spray chamber, and borosilicate glass Scott-type concentric nebulizer.

Table 4. 2: Composition of the SLFs used

Composition	Gamble Solution (GS) g/L	Artificial Lysosomal Fluid (ALF) g/L
NaCl	6.779	3.21
Na_2HPO_4	-	0.071
$NaHCO_3$	2.268	-
Sodium citrate dehydrate	0.055	0.077
NH_4Cl	0.535	-
Glycine	0.375	0.059
NaH_2PO_4	1.872	-
L-Cysteine	0.121	-
NaOH	-	6
Citric acid	-	20.8
$CaCl_2.2H_2O$	0.026	0.128
Na_2SO_4	-	0.039
$MgCl_2.6H_2O$	-	0.05
Disodium tartrate	-	0.09
Sodium lactate	-	0.085
Sodium pyruvate	-	0.172

4.5.2 In Vitro Analysis

The first step consisted of the cell culture. THP-1(monocytic/macrophage), HL-60 (neutrophilic), and A549 (lung epithelial) cells (ATCC, Manassas, VA, USA) were incubated at 37˚C in complete media according to the manufacturer's instructions. Cells were monitored for confluence and appropriately passaged periodically. THP-1 and HL-60 cells were seeded (2.0×10^5 cells per well) in 24 well plates and were then differentiated

using 1.25% DMSO in media over the course of 5 days. A549 cells were similarly seeded at 2.0×10^5 cells per well and did not require differentiation.

For PM in vitro exposures, HL-60 cells were treated with a low (5 µg/mL), medium (10 µg/mL), and high (20 µg/mL) concentration of previously fractionated PM10. A549 and THP-1 cells were exposed to a low (10 µg/mL) and high (100 µg/mL) concentration of PM_{10}. Each of these cell lines was exposed to PM_{10} for 4 h, and each PM treatment was run in either duplicate or triplicate technical replicates. Supernatants were then collected for further analysis.

Proinflammatory Panel 1 (Human) Kit V-Plex (K15049D-1, Meso Scale Diagnostics, Rockville, MD, USA) was used to assess cytokine expression in the HL-60 and A549 cells from PM_{10} exposures. The following cytokines were evaluated for HL-60 and A549 cells: IFN-γ, IL-1β, IL-2, IL-4, IL-6, IL-8, IL-10, IL-12p70, IL-13, and TNF-α. Cytokine Panel 1 (Human) Kit V-Plex (K15050D-1, Meso Scale Diagnostics, Rockville, MD, USA) was used to assess cytokine expression, including GM-CSF, IL-1α, IL-5, IL-7, IL-12/IL-23p40, IL-15, IL-16, IL-17A, TNF-β, and VEGF-A in THP-1 cells. Meso Scale plates were run according to the manufacturer's instructions. Briefly, the supernatant was collected and pipetted onto plates. These plates were incubated with gentle shaking for 2 h at room temperature. Plates were washed three times with buffer solution. Detection antibodies were added to the wells and reacted at room temperature for 1 h. Read buffer was added to each well, and plates were analyzed on a Meso Scale Discovery QuickPlex SQ instrument (Meso Scale Diagnostics, Rockville, MD, USA). Discovery Workbench software was used to calculate cytokine concentrations based on each cytokine standard curve. The following equation evaluated change in protein expression: Log = exposed cell concentration/control and plotted according to each dust sample.

4.6 Results and Discussion

4.6.1 Particle Size Distribution

From the SEM analysis, it was verified that all samples were under 10 µm. Only a few particles were outside the range, representing its maximum 1% of the total number of particles analyzed. Histograms with particle size distribution were built by the number of particles. **Table 4.3** shows the information obtained from the SEM analysis, including the mean width and length of the particles, and the percentage fraction of the particulate matter (PM) less than 1 µm (PM_1), 2.5 µm ($PM_{2.5}$), 4 µm (PM_4), and 10 µm (PM_{10}).

Table 4. 3: Mean width and length of the particles and percentages of different particle fractions.

Mine ID	Mean Width (µm)	Mean Length (µm)	PM_1 (%)	$PM_{2.5}$ (%)	PM_4 (%)	PM_{10} (%)
Mine 1	3.86 ± 1.62	6.03 ± 2.80	0	18	58	100
Mine 2	3.81 ± 2.06	5.70 ± 3.20	0	28	62	99
Mine 3	3.15 ± 1.76	4.82 ± 2.26	0	39	83	99
Mine 4	3.24 ± 2.00	5.07 ± 3.10	4	44	73	99
Mine 5	2.95 ± 1.65	4.43 ± 2.11	7	46	77	100

Sub-micron and supra-micron fractions were extracted from the particle size information. It was observed that the majority of the particles were in supra-micron size. Only Mine 4 and Mine 5 had sub-micron particles, representing the 4% and 7% of the particles counted, respectively. However, it is essential to mention that with the resolution of the images obtained, it was difficult to measure individual particles less than 1 µm or differentiate them from the structural layers in the coal, which may have led to an underestimating of the sub-micron fraction.

Mines from the Appalachian region had both a mean width and length smaller than samples from the Rocky Mountains, which were approximately 20% coarser. Considering that all the samples were prepared in the same way, the differences in the particle size distributions are attributed to the specific characteristics of each sample, such as the hardness and mineral contents. Additionally, significant differences in the percentages of PM_4 and $PM_{2.5}$ were found, indicating that the overall samples from the Appalachian region contain a higher number of finer particles.

Angular edges may considerably influence the interaction of the particles with lung tissue, increasing inflammation.[126] In the images (**Figure 4.1**), even if the particle shape was not extensively analyzed, it can be observed that overall, particles are not entirely sharp. The samples from the different mines all showed a transitional particle shape, according to the qualitative shape classification used by Sellaro, et al., 2015, which are particles in-between an angular and a rounded shape.[35] All samples were prepared following the same procedure, which may have provided similar particle shapes within the mines. In addition, the extensive hours of grinding may have rounded the edges of the particles, which is not necessarily the particle shape produced by the specific equipment and methods used in each mine. Since there are no significant differences in the particle shapes between mines and these ones, they may not be representative, and they were not considered as an influential factor for this study.

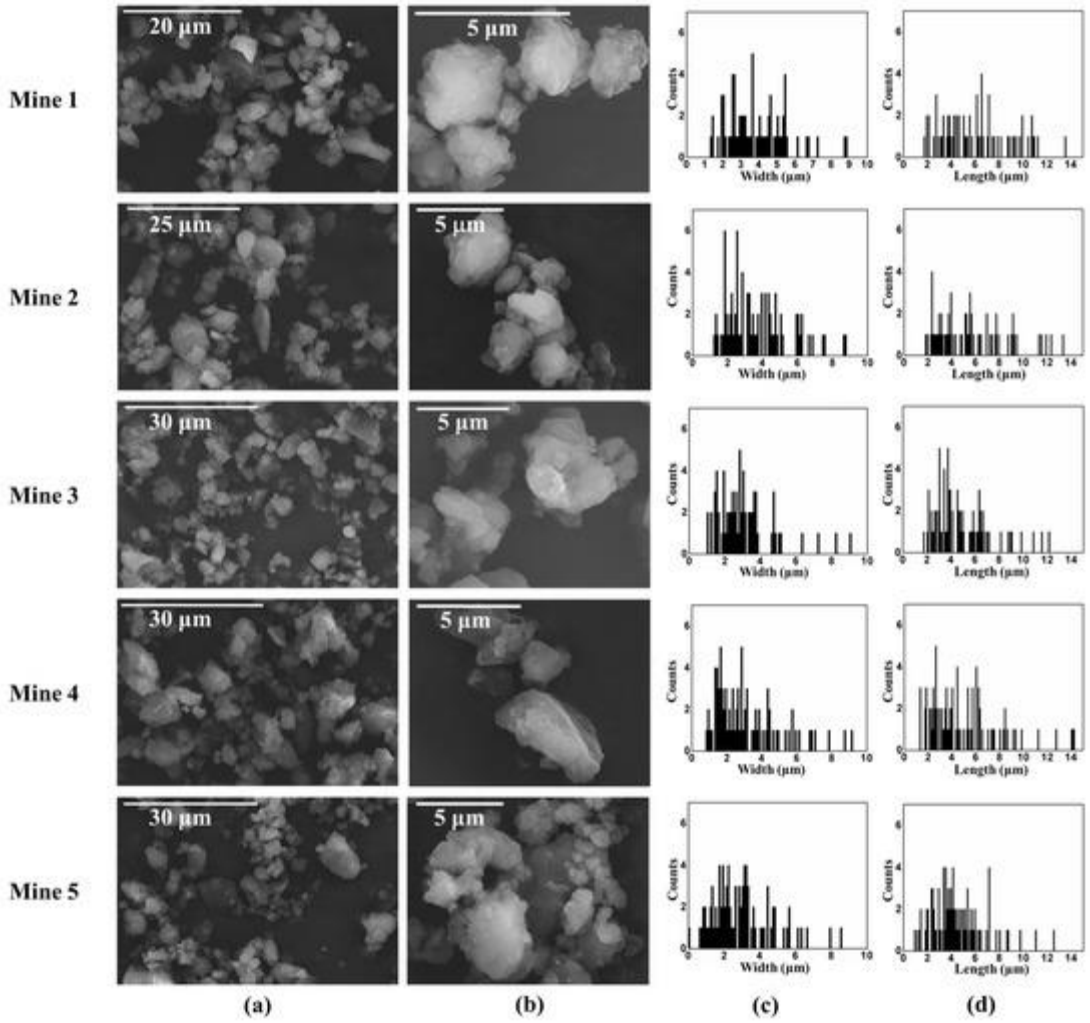

Figure 4. 1: SEM results from the 5 mines. (**a**) SEM images. (**b**) Zoomed-in SEM images. (**c**) Particle size distribution based on width. (**d**) Particle size distribution based on length.

4.6.2 Mineral Composition

The mineral phases present in the coal samples are reported in **Table 4.4**. The XRD patterns obtained (**Figure 4.1**) showed that the five mines studied have in common the presence of quartz and kaolinite, as expected. Additionally, in all the samples except for Mine 5, pyrite was observed. These three minerals showed to be the main mineral components in the coal samples. It also observed small peaks for siderite and calcite in Mine 4 and Mine 5, respectively. The limitation of the method is that it is difficult to state the exact amount of each mineral, but relative abundances can be compared.

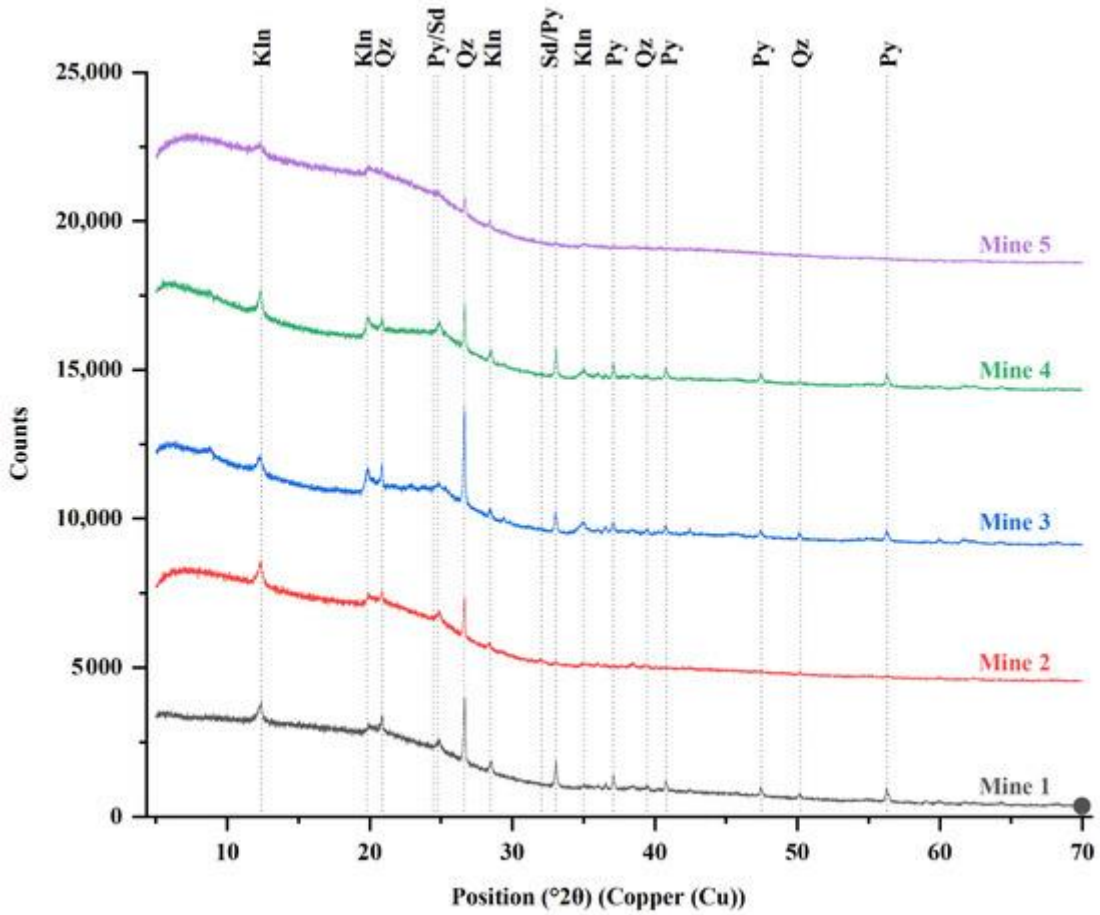

Figure 4. 2: XRD patterns of coal samples from Mine 1, Mine 2, Mine 3, Mine 4, and Mine 5. Symbols, according to[139, 140]: quartz (Qz), kaolinite (Kln), siderite (Sd), pyrite (Py), and calcite (Cal).

Table 4. 4: Minerals, compound names, and chemical formulas of the crystalline phases present in Mine 1, Mine 2, Mine 3, Mine 4, and Mine 5.

			Mine ID				
Mineral	**Compound Name**	**Chemical Formula**	**Mine 1**	**Mine 2**	**Mine 3**	**Mine 4**	**Mine 5**
Quartz	Silicon Oxide	SiO_2	X	X	X	X	X
Kaolinite	Aluminum Silicate Hydroxide	$Al_2(Si_2O_5)(OH)_4$	X	X	X	X	X
Pyrite	Iron Sulfide	FeS_2	X	X	X	X	
Siderite	Iron Carbonate	$Fe(CO_3)$		X			
Calcite	Calcium Carbonate	$CaCO_3$			X		

After plotting the raw data, a large wave in the spectrum at the beginning of the graph was observed. This hump in the XRD spectra is characteristic of amorphous materials due to the random molecular structures.[141, 142] It indicates the presence of considerable amounts of amorphous materials corresponding to the carbonaceous matter.

The relative abundance of the mineral phases was obtained from the intensity displayed by each one in the XRD patterns. The same peaks from the different samples were compared to identify which mine had more content of each mineral. Some peaks in the spectra had influence from two minerals, so only the major peaks showing the influence of single minerals were considered for comparison. This helps to have an idea of the relative abundance of the minerals among the mines, but not a measured value. The overall idea is that, comparing the same peaks, the higher the intensity, the higher the abundance of the mineral in the samples since the beam found more atoms aligned in this direction. **Table 4.5** shows the values of the counts for each mineral extracted from the software. In **Figure 4.3**, the counts per mineral phase were plotted for the five mines. The major peak was located at the position 2θ~26.65°, which corresponds to quartz. It is clear from **Figure 4.2** that the peak for Mine 3 is significantly higher than for the rest of the samples, suggesting that Mine 3 has a higher amount of quartz in its composition. In the same way, Mine 5 has a smaller peak at this position, indicating a lower amount of quartz in the sample.

Table 4. 5: Percentages of the relative mineral abundance, total counts, and counts per mineral in XRD data

	Counts of major peak					**Peak position (°2θ)**
Mineral	**Mine 1**	**Mine 2**	**Mine 3**	**Mine 4**	**Mine 5**	
Quartz	2167.11	1316.02	3266.8	1626.2	564.32	26.65°
Kaolinite	341.11	394.53	697.91	609.89	312.64	12.38°
Pyrite	885.48	81.46	657.47	942.21	0	33.04°
Siderite	0	81.53	0	0	0	32.02°
Calcite	0	0	138	0	0	29.44°

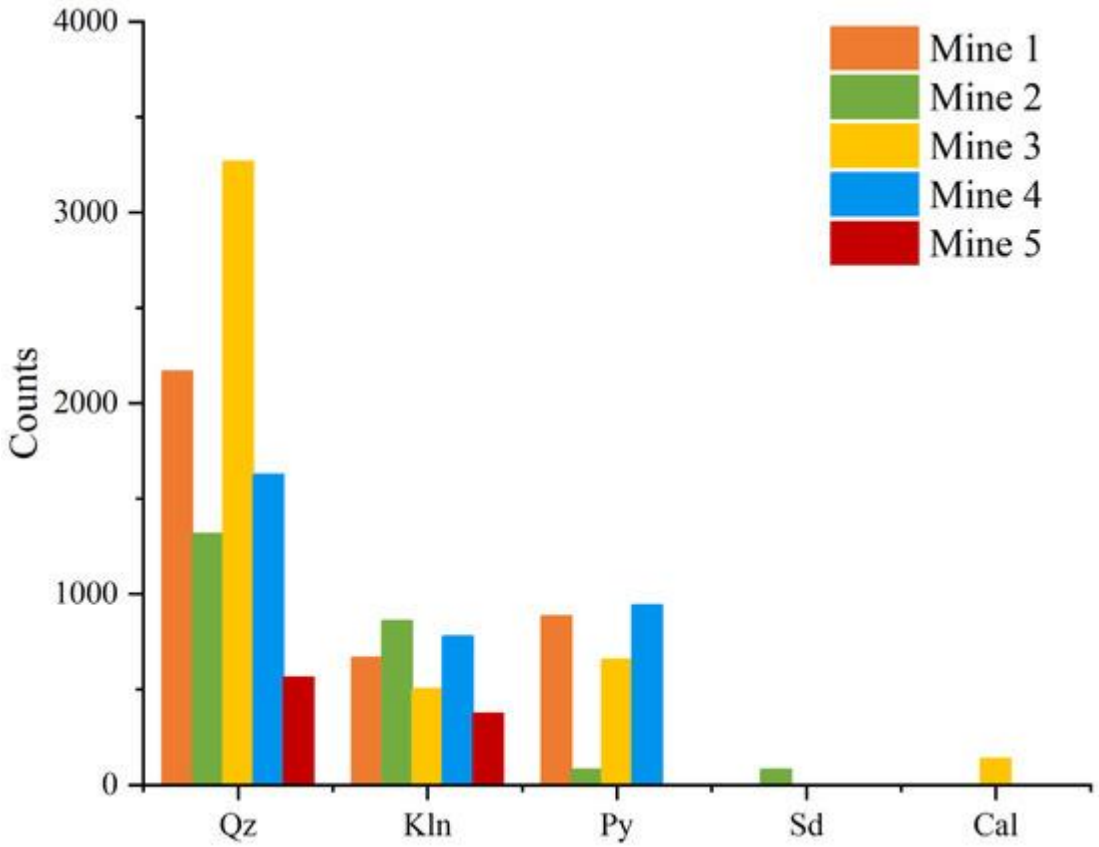

Figure 4. 3: Relative abundance of the minerals in Mine 1, Mine 2, Mine 3, Mine 4, and Mine 5. Quartz (Qz), Kaolinite (Kln), Siderite (Sd), Pyrite (Py), and Calcite (Cal).

Regarding kaolinite, from **Figure 4.2**, we can observe that the peaks for kaolinite (position $2\theta \sim 12.38°$) look to have similar intensities. This can be observed as well in **Figure 4.3**, where the major peaks for each mineral were compared. The relative amount within the mines is very similar, except for Mine 5, which had fewer counts in the diffraction pattern. Pyrite was not observed in Mine 5 and showed a low intensity in Mine 2. The other three mines showed similar contents of pyrite.

Mine 5 was a relatively cleaner sample since it has only quartz and kaolinite, and peaks can barely be seen in the diffraction pattern, indicating small amounts of minerals. With respect to the geographic locations, quartz and pyrite vary within the mines in the Appalachian region with no trends. The same observation was achieved for samples from the Rocky Mountains. Considerable differences were found within the Appalachian region mines since Mine 5 was collected in north–central Appalachian and Mine 3 and 4 were collected from northern Appalachia, which may indicate geological differences.

In underground mines, RCMD has contributions from different sources, mainly from the coal seam, host rock, diesel equipment, and rock dust. The final composition of RCMD is a mixture of all these components, providing, in some cases, higher concentrations of quartz and other minerals (compared to the dust from only the coal seam),

especially in the production areas.[29] In this study, only the coal samples from the seam were used, so small mineral contributions were expected in the dust samples.

4.6.3 Elemental Composition

From the original raw data, Be, Co, Se, Mo, Ag, Cd, Sn, Sb, Tl, Th, and U were not included in the results since all of them showed readings under 10 ppb, which is lower than the limit of detection for the method with the dilution used. Additionally, after mass normalization, almost all of the above-mentioned elements resulted in under 5 ppm, suggesting that these elements were in negligible concentrations or not present in the samples.

The SRM sample was digested completely, and the total concentration of the analyzed elements was obtained. The results from the method and the information of the SRM were compared, and reliable data were obtained for 14 elements: Al, Si, Fe, Ti, Sr, Ba, Pb, Mn, Ni, Cu, As, V, and Cr (**Table 4.6**). Most of them met the allowable error described in the SRM information when available or remained between 1% and 15% when the error was not reported in the SRM data. Only Si, Al, and Fe were out of range but still within 1%–15% of the relative difference with the SRM, so they were included in the results.

Table 4. 6: Summary of element content of dust samples.

Mine ID	Al	Si	Fe	Ti	Sr	Ba	Pb	Mn	Ni	Cu	Zn	As	V	Cr
	%	%	%	µg/g	µg/g	µg/g	µg/g	µg/g	µg/g	µg/g	µg/g	µg/g	µg/g	µg/g
Mine 1	0.66	1.18	0.65	608	127.4	53.3	20.4	28.7	7.5	20.8	24.0	6.8	9.3	8.0
Mine 2	0.73	1.13	0.20	503	21.6	8.9	23.5	7.2	7.4	11.7	12.6	1.0	4.8	7.1
Mine 3	0.90	3.53	0.89	1114	41.2	56.6	16.6	24.4	21.8	20.4	52.7	27.8	36.9	26.3
Mine 4	1.03	2.46	1.13	1040	69.2	45.0	8.7	8.0	16.0	13.0	36.3	14.8	55.4	26.1
Mine 5	0.65	0.91	0.12	310	75.5	45.1	10.6	4.9	11.3	23.2	3.7	1.2	11.6	7.5

Li, Mg, K, and Ca showed relatively high concentrations but were not included in the results due to high relative differences (30% to 44%) when tested using SRM. These elements were under or very close to their detection limit, so it may have led to the spreading in the results. The information and results of the SRM are shown in **Table 4.7**. Zn and Sr were not reported in the SRM information, so it was impossible to verify their reliability, but the results were in the same order as the digested SRM in the lab, so they were included for reference. The results are shown in **Figure 4.4** and are separated into major and trace element components.

Table 4. 7: SRM verification (µg/g)

Element	Li	Mg	Al	Si	K	Ca	Ti	V	Cr	Mn	Fe	Ni	Cu	As	Ba	Pb
SRM CLB-1 Digested	5.7	157.5	6815	10465	440	1095	452	12.24	9.29	8.4	8309.6	18.1	8.5	13.6	31.6	5.1
SRM CLB-1 Information	8.0	279.1	7991	11734	631	1572	467	12.0	9.70	8.0	8742.5	18.0	10.0	13.0	34.0	5.1
Allowable error	N.R.	18	212	982	41.5	71.5	18	1	1.2	N.R.	350	2	N.R.	N.R.	5.0	0.7
Difference	2.31	122	1176	1269	191	477	15.45	-0.24	0.41	-0.4	432.9	-0.10	1.52	-0.56	2.37	0.03
Relative difference (%)	29%	44%	15%	11%	30%	30%	3%	-2%	4%	-4%	5%	-1%	15%	-4%	7%	1%

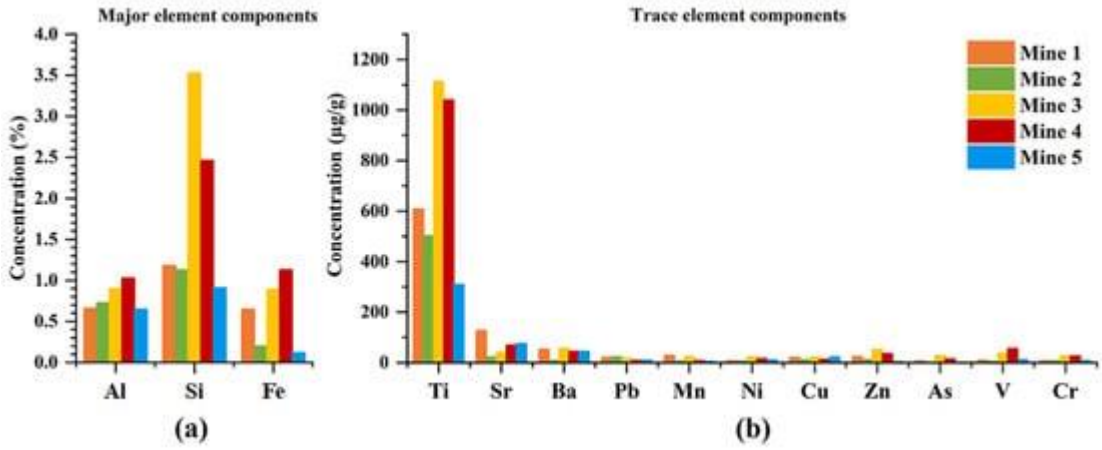

Figure 4. 4: (**a**) Major and trace element components in the samples, (**b**) Trace element components in the samples.

Most of the elements had higher concentrations in Mine 3 and Mine 4, from the Appalachian region. Mine 5, overall, had the lowest concentrations, except for Cu and Sr, which were higher than in other mines. Al, Si, and Fe were the major elements in all the samples, corresponding to the major components of the minerals found in the XRD analysis. The rest of the elements were in very low concentrations, so it could be said that they are present in trace levels. Al showed similar concentrations among the coal from the different mines, similar to the XRD results. Fe was in a lower concentration in Mine 2 and Mine 5, and Si significantly higher in Mine 3, both in accordance with the XRD results as well.

4.6.4 Surface Composition

A typical coal dust sample exhibited strong peaks due to the carbon and oxygen, with small peaks due to the iron also observed in the elemental content and dissolution studies. The C1s region was fitted using the asymmetric Doniach-Sunjic-Shirley profile as described in recent literature.[137] The C1s region shown in **Figure 4.5** was dominated by a graphitic carbon peak as well as a sp^3 hybridized carbon peak. Carbon-oxygen bonds (C-O and C=O) corresponded to about 2.4% of the total carbon. This was much less than the

total oxygen content obtained from the O1s/C1s ratio shown in **Table 4.8**. The O1s region was broad and did not allow an exact spectrum fitting. This suggests that coal dust samples also contained a significant amount of oxygen associated with hydroxyl groups or trapped water. The total oxygen content was comparable in all samples but for Mine 3, where it was markedly lower.

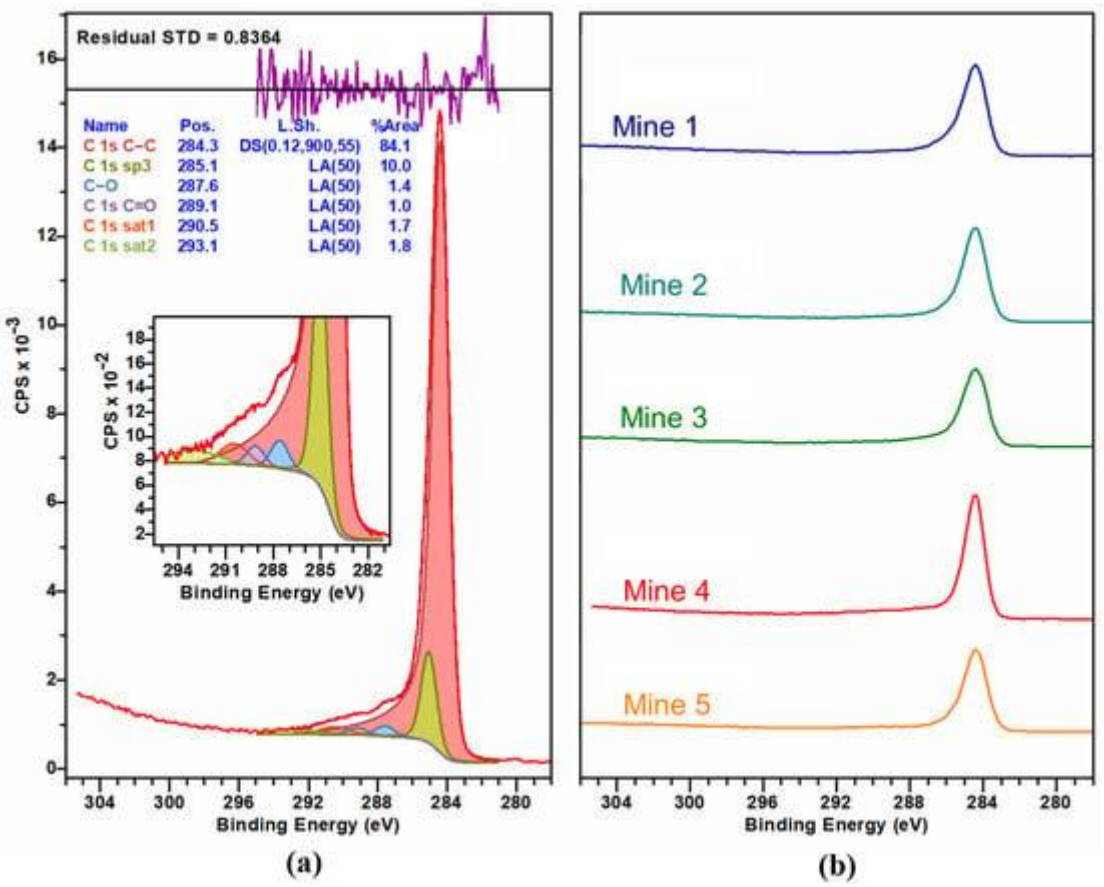

Figure 4. 5: (**a**) High-resolution C1s spectrum of Mine 4, peak fitted with synthetic components based on the literature data.[137] (**b**) C1s spectra of the dust samples.

Table 4. 8: Elemental composition on the surface of the coal dust.

Mine ID	**Al (2p) %**	**C (1s) %**	**O (1s) %**	**Si (2p) %**
Mine 1	0.91	86.55	11.75	0.79
Mine 2	1.37	87.09	10.41	1.13
Mine 3	0.83	90.98	6.74	1.44
Mine 4	1.89	87.74	9.27	1.10
Mine 5	0.17	90.82	8.28	0.73

The results are shown in **Table 4.8**. As expected, the main component on the surface of the sample was C1s. Si2p had a composition according to the results from the total digestion. In the case of Al, the results were not according to the total digestion. Mine 3 had a high concentration of Al in the total digestion, close to the concentration of Mine 4, but here the percentage of Al in Mine 3 was significantly lower. The same was seen for Mine 5, which had a similar concentration to Mine 1, but here it was shown to be around five times less than Mine 1. This may be explained by the minerals present in the selected samples. Al is related to kaolinite, which occurs in nature packed in layers, so Al may not be exposed on the surface in all cases. Fe was found with the total digestion and XRD, but it did not appear exposed on the particle surface according to the XPS results.

When analyzing the trends by geographic location, the samples regarding Al and Si did not follow a clear pattern. The only significant differentiation was for O, which presented a lower exposure in the particle surface for the mines in the Appalachian region.

4.6.5 Specific Surface Area and Micro-Pore Analysis

The specific surface area of dust samples was determined using a seven-point N_2 adsorption isotherm, and the measured surface area was found to be similar for all the samples, ranging from 6.80 to 7.77 m^2/g. The surface area was 7.77 ± 0.45, 7.66 ± 0.15, 6.80 ± 0.10, 7.11 ± 0.23, and 7.58 ± 0.33 m^2/g for Mine 1, Mine 2, Mine 3, Mine 4, and Mine 5, respectively. Further, micro-pore analysis was performed, and all the samples were found to be mesoporous with a half pore size distribution found at 58.81 Å. The summary of the results is shown in **Table 4.9**.

Table 4. 9: Specific surface area and half-pore width of samples.

Mine ID	**Specific Surface Area (m^2/g)**	**Half Pore Width (Å)**
Mine 1	7.77 ± 0.45	58.81
Mine 2	7.66 ± 0.15	58.81
Mine 3	6.80 ± 0.10	58.81
Mine 4	7.11 ± 0.23	58.81
Mine 5	7.58 ± 0.33	58.81

The specific surface area and micro-pore analysis of the dust samples are important because they give the area that is in contact with the SLF in the dissolution experiments. The formation of the surface complexes is highly dependent on the exposed surface area and thus governs the dissolution process. The same mass (20 mg) was used for each dissolution experiment. Therefore, a big difference in the specific surface area among the samples may influence the final dissolutions of the elements because it is presumed that a larger exposed area to the SLF can result in more dissolution and, finally, biased results. In this case, the specific surface area of the samples was very close to each other, representing the minimum influence of the exposed area in the dissolution experiments.

4.6.6 Initial Functional Groups

FTIR spectra of coal dust were collected from a 4000 to 600 cm^{-1} wavenumber range. In general, FTIR spectra of coal show four bands: 3800-3000 cm^{-1} for the hydroxyl structures, 3000-2800 cm^{-1} for the aliphatic structures, 1800-1000 cm^{-1} for the oxygen-containing functional groups, and 900-700 cm^{-1} for the aromatic structures. However, the spectra we collected showed no prominent peak in the hydroxyl and aliphatic regions. Hence, spectra are reported within the range of 2000 to 700 cm^{-1} wavenumbers. The obtained results are shown later in **Figure 4.10,** and their respective peak assignments are in **Table 4.13**.

The absorption peak around 1000-1200 cm^{-1} is the most obvious. This peak indicates the presence of oxygen-containing functional groups in the coal dust as the highest species. The peak coming at 1120-1080 cm^{-1} is associated with S=O stretching. The peaks in the range of 1060-1020 cm^{-1} are associated with Si-O-Si or Si-O-C stretching. The doublet at 799-779 cm^{-1} is a representative of Si-O-Si bridging, which is the characteristic peak for low-temperature quartz and is also used for the quantitative determination of silica. The peak at 913 cm^{-1} is associated with kaolinite, a common clay mineral. The peak at 1602 cm^{-1} is for benzene ring C=C stretching, whereas the peak at 1445 cm^{-1} is associated with antisymmetric -CH_3 deformation.[143]

4.6.7 Dissolution in Simulated Lung Fluids

Variable dissolutions of elements across the samples and within the same SLF were found. This may be influenced by several factors, such as the particle size, the surface area, the availability of the elements (elemental composition), the surface composition, and/or the mineralogy. **Figure 4.6** shows the elements dissolving in GS, and **Figure 4.7** in ALF. Dissolutions were mass normalized, and each panel used the same scale to visualize the mines that presented more dissolution of the main elements. The data were fitted to the Langmuir-type model. Surface area normalization was carried out as well to eliminate the particle size and surface area influence, and the results are shown in **Figures 4.8** and **4.9**. The surface area was very similar for all the samples, so the exact behavior of dissolutions was obtained in the results.

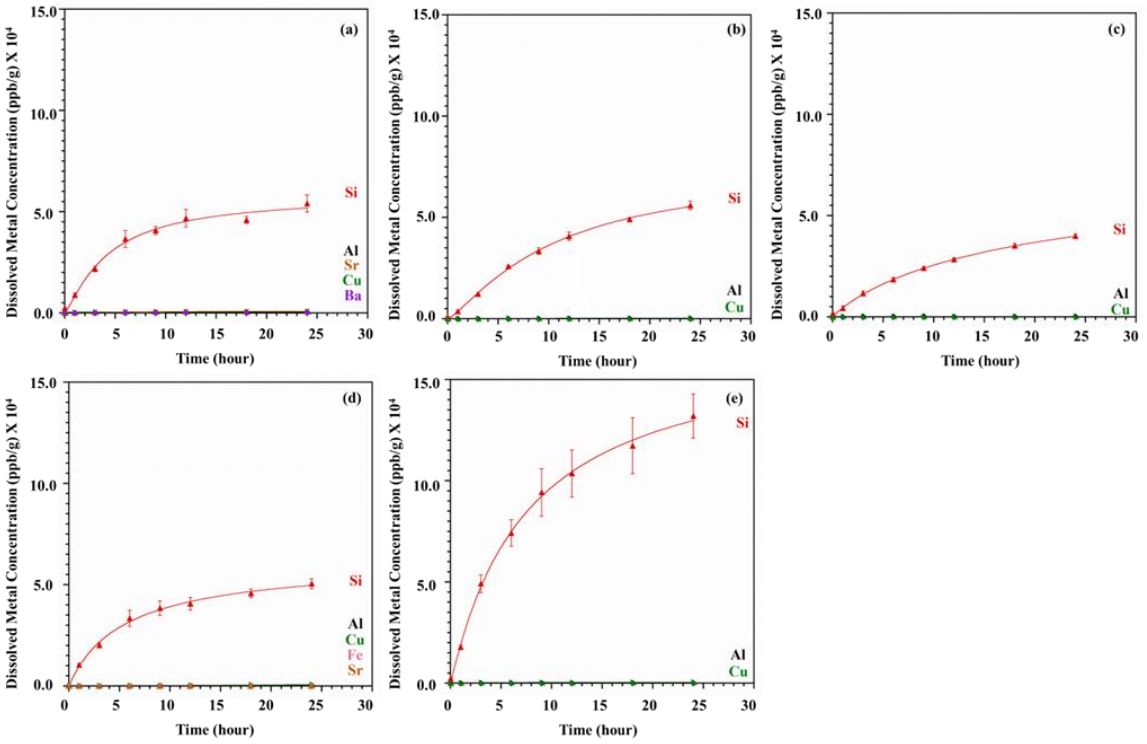

Figure 4. 6: Mass normalized dissolution of metals as a function of time in GS from (**a**) Mine 1, (**b**) Mine 2, (**c**) Mine 3, (**d**) Mine 4, and (**e**) Mine 5.

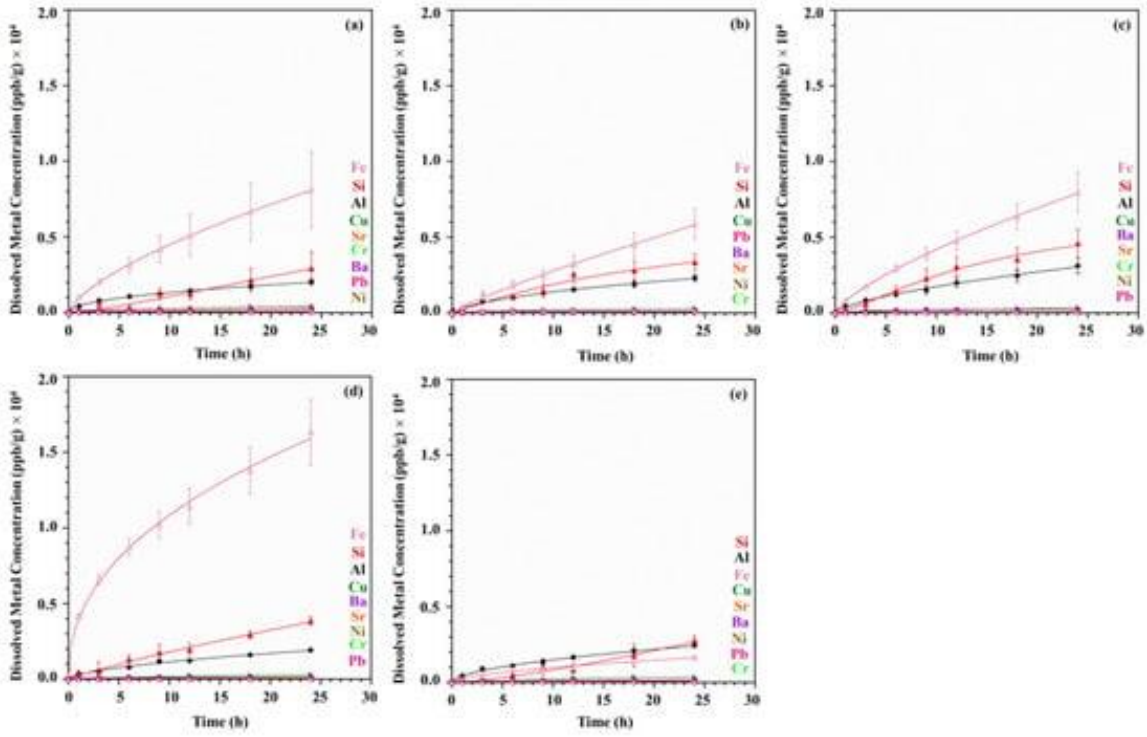

Figure 4. 7: Mass normalized dissolution of metals as a function of time in ALF from (**a**) Mine 1, (**b**) Mine 2, (**c**) Mine 3, (**d**) Mine 4, and (**e**) Mine 5.

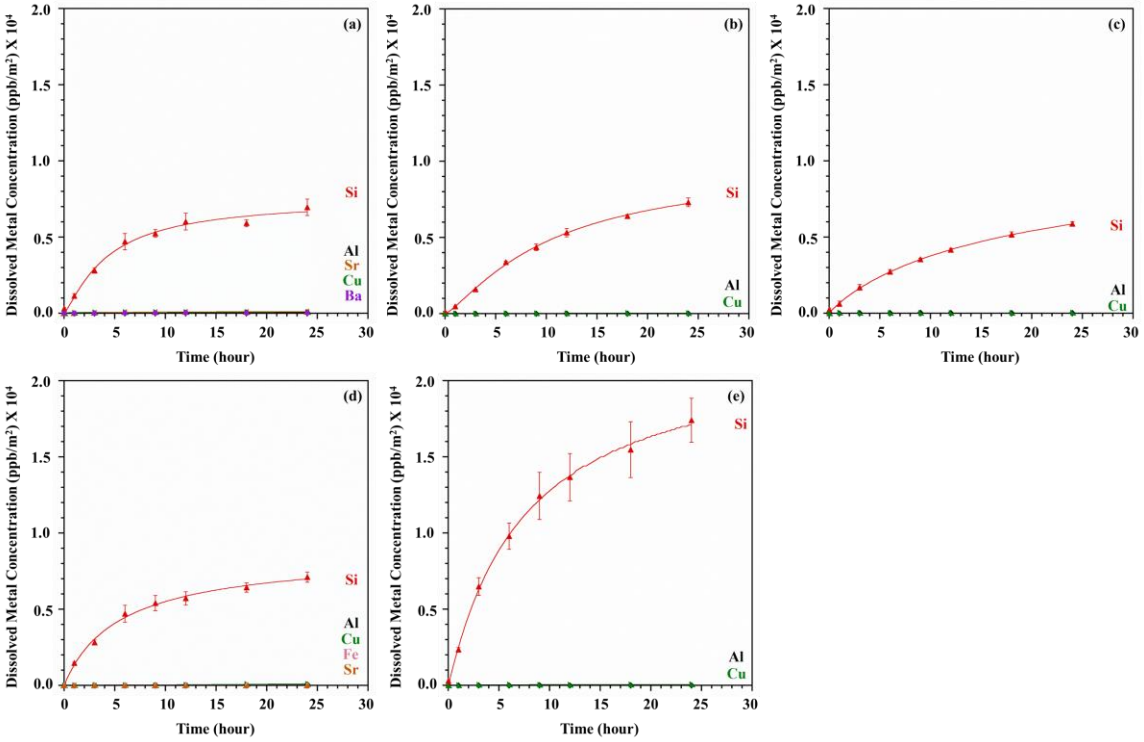

Figure 4. 8: Mass and surface area normalized dissolution of metals as a function of time in GS from (a) Mine 1, (b) Mine 2, (c) Mine 3, (d) Mine 4, and (e) Mine 5.

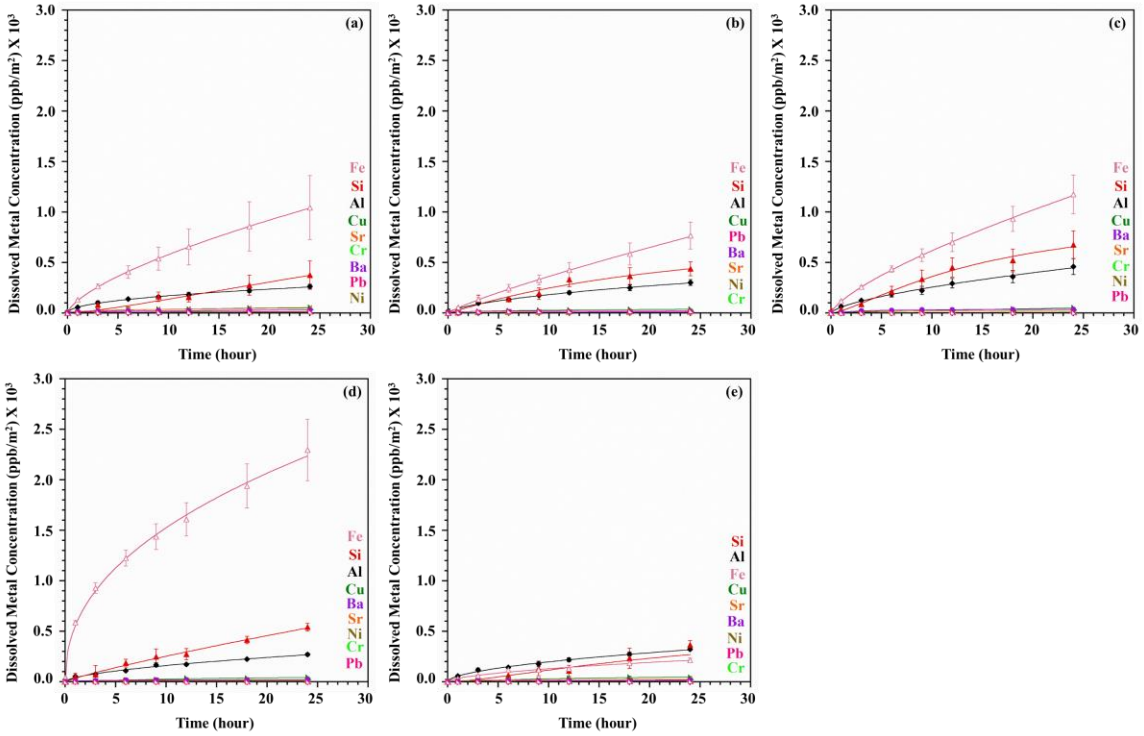

Figure 4. 9: Mass and surface area normalized dissolution of metals as a function of time in ALF from (a) Mine 1, (b) Mine 2, (c) Mine 3, (d) Mine 4, and (e) Mine 5.

The ICP-MS analysis showed Si being the most dissolved element in GS for all the coal samples. Significantly lower dissolutions of Al, Cu, and in some cases Fe, Ba, and Sr were found after 24 h of the dissolution experiment. For ALF, higher dissolutions were found for Fe, Al, Si, and Cu, which showed increases in the concentration with the reaction time for all the coal samples. Very low dissolutions of Sr, Cr, Ba, Pb, and Ni were consistently found as well in ALF. The total dissolutions of the most dissolved elements after 24 h are shown in **Table 4.10**.

Table 4. 10: Final metal concentrations after 24 h of dissolution in SLF. Values in ppb/g.

	Al		**Si**		**Fe**		**Cu**		**Sr**		**Pb**	
Mine ID	**ALF**	**GS**	**ALF**	**GS**	**ALF**	**GS**	**ALF**	**GS**	**ALF**	**GS**	**ALF**	**GS**
Mine 1	2316.8	142.6	3351.4	56,005.8	5879.2	-	291.5	323.6	83.1	-	160.2	-
Mine 2	2058.8	555.8	2918.8	54,117.4	8117.8	7.7	435.9	692.4	391.8	-	109.9	-
Mine 3	3135.5	210.2	4591.1	39,917.9	7993.1	-	354.4	245.0	188.9	-	47.6	-
Mine 4	1925.6	468.1	3850.9	50,576.9	16,329.1	315.4	309.1	752.5	108.4	-	22.5	-
Mine 5	2444.2	162.5	2764.3	131,965.8	1633.2	-	334.8	546.6	202.9	-	56.4	-

It was observed that some of the element dissolutions were influenced by the pH of the SLF used. In general, Al, Fe, Sr, and Pb showed higher dissolutions in ALF than in GS, indicating the great influence of the pH of the SLF used. Al and Fe showed 4 to 16-fold and > 50-fold higher dissolutions in ALF, respectively. Higher dissolutions for Si (9 to 48-fold higher) and slightly higher for Cu were found in GS. The higher dissolution of Si in GS may be explained by the fact that part of the Si may come from the quartz (SiO_2) present in the sample. Quartz is an acid oxide, so it dissolves slowly in alkaline solutions.[144] The GS pH is 7.3, placed on the alkaline side of the pH scale. The ALF pH is 4.5, representing a more acidic media for the Si dissolutions (giving less dissolution), but providing better conditions of pH for the dissolution of other components (i.e., Fe, Al, Sr, and Pb).

Table 4. 11: Percentage dissolves from the initial availability of the elements.

Mine ID	Al (%)		Si (%)		Fe (%)		Cu (%)		Sr (%)		Pb (%)	
	ALF	GS	ALF	GS	ALF	GS	ALF	GS	ALF	GS	ALF	GS
Mine 1	0.035	0.002	0.028	0.475	0.090	-	1.401	1.556	0.065	-	0.785	-
Mine 2	0.028	0.008	0.026	0.479	0.408	0.000	3.726	5.918	1.814	-	0.468	-
Mine 3	0.034	0.002	0.013	0.113	0.089	-	1.737	1.201	0.459	-	0.287	-
Mine 4	0.018	0.005	0.016	0.206	0.144	0.003	2.378	5.789	0.157	-	0.259	-
Mine 5	0.038	0.003	0.031	0.462	0.131	-	0.443	0.356	0.269	-	0.532	-

Characterization experiments indicated that Al, Si, and Fe were the main components of the samples, which gave the higher dissolutions as well in SLF, so overall, the initial availability of the metals in the samples plays a vital role in the dissolutions in SLF (the more the availability, the higher the concentration after dissolution in SLF). However, comparing the magnitude of the initial concentration vs. the total dissolution in SLF (availability normalization) for the major element components (Al, Si, and Fe) and some of the trace elements (Sr and Pb), a very small percentage of the initial amount was dissolved, representing less than 0.5% in most of the cases for both GS and ALF, many even below 0.1%. The availability comparison is shown in **Table 4.11**. On the other hand, Cu, which was found as a trace element, having a lower availability in the samples, and, thus, a low concentration after the dissolutions in SLF, showed values ranging from 1.2 to 5.9% of the initial concentrations. So, Cu was more soluble than the other elements since a higher percentage of the initial available Cu was digested in both GS and ALF. Sarver et al. found much higher dissolutions of elements when RCMD samples collected in the filter were dissolved in SLF.[29] Si, Al, Cu, and Fe were found to have 75, 26, 90, and 5% or less of the total initial concentration dissolved in SLF. This previous study is based on dust samples collected on the filter, while the current research was conducted using bulk coal samples collected from the mines and then prepared in the lab; therefore, the composition of the dust is different. According to the mean mineralogy distributions found for the samples collected in the filter (larger particles: 400-10,000 nm), the carbonaceous mineralogy class represented less than 15% of the composition for all the mines and sample locations studied.[29] Characterization results indicate that samples used in this study were mainly carbonaceous materials with very few mineral contributions. In the case of the major elements found by Sarver et al., the total element concentrations (acid-soluble) ranged from 10 to 200 mg/g, while the samples used in this study ranged from 1.2 to 35.3 mg/g (0.12%–3.53%) as shown in **Table 4.6**. These significant differences in sample compositions might explain the difference in the results between the two studies.

Higher dissolution of Si in GS and Al, Fe, and Pb in ALF were observed when the initial availability of these elements was higher, indicating that dissolutions in these cases are directly related to the mineral composition. This behavior was not observed in the rest of the dissolutions, which are generally influenced by the pH of the solution. In the case of Cu, it was observed that the initial availability nor pH of the solutions did not drive its dissolutions. In this case, the dissolution may have been driven by the chemical affinity of the Cu with the free ions in the SLF solutions. The mode of occurrence and oxidation state of the elements in the RCMD have an important role in the dissolution process, improving or impairing their affinity with the free ions and solvent agents in the SLF solutions.

The Sarver et al. study associated the dissolution in SLF of these elements with the contribution of the geologic strata in the mine or the rock dusting products applied to the RCMD.[29] This study only studied coal from the seam (no strata or rock dust influence); thus, it can be concluded that the coal seam also contributes to the final concentrations of elements found after dissolution experiments in the SLF, but probably in small quantities.

A clear trend was not observed when comparing by geographic location since the dissolutions were led by different factors (**Table 4.12**). Even if samples from the

Appalachian region had a higher initial availability in most cases, the dissolution experiments varied in the final concentration after being dissolved in SLF.

Table 4. 12: Factors influencing dissolutions in SLF. Av: availability.

Al		Si		Fe		Cu		Sr		Pb	
ALF	GS	ALF	GS	ALF	GS	ALF	GS	ALF	GS	ALF	GS
pH	pH + Av.	Av.	pH	Av. + pH	pH	Possible Affinity	Possible Affinity	pH	pH	pH	pH

In summary, from the dissolution experiment, it was obtained that the main elements dissolving from the dust samples when in contact with the SLF were Al, Si, Fe, Cu, Sr, and Pb. The overloading in the human body of Al, Fe, Cu, and Pb has been related to different diseases and health issues, as described below.

In humans, Mg^{2+} and Fe^{3+} are replaced by Al^{3+}, which causes many disturbances associated with intercellular communication, cellular growth, and secretory functions.[145, 146] Al has been found to be very harmful to nervous, osseous, and hemopoietic cells.[145] Al also accumulates in the kidney, producing renal function.[147-149] Exposure to quartz as RCS (present in the samples) has been related to the development of chronic renal disease.[150]

Fe and Cu are essential elements for humans. Fe plays an important role in fundamental vital activities (such as growth and survival) [145, 151-158], and Cu is in the function and maintenance of the human immune system.[159-163] While Cu and Fe are essential nutrients for humans, they can pose risks to human health with elevated exposure.[151, 155, 162, 164] An excess of Cu and Fe aggravates oxidative stress, which leads to accelerated tissue degeneration and DNA damage.[151, 163, 165] Fe overload may be harmful, causing carcinogenesis. Fe toxicity is primarily based on its ability to catalyze the generation of radicals, which attack and damage cellular macromolecules and promote cell death and tissue injury.[151, 155, 156] Hemochromatosis, hepatocellular cancer, iron-loading anemias, dietary iron overload, and chronic liver disease are conditions related to Fe overload.[151, 156] Fe dysregulation is closely associated with the initiation and development of several malignant tumors, including lung cancer.[155, 157, 158]

An excess of free Cu ions can cause damage to cellular components and reduce cell proliferation.[162, 165] In the most severe forms, Cu toxicity leads to rhabdomyolysis, cardiac and renal failure, methemoglobinemia, intravascular hemolysis, hepatic necrosis, encephalopathy, and ultimately death.[165]

Al, Fe, and Cu are related to neurodegenerative changes.[151, 160, 166] Al and Fe have been linked to neurological disorders, including Alzheimer's and Parkinson’s disease.[146-148, 151, 166-169] Cu toxic levels in the brain have been reported to cause apoptosis, astrocytosis, impaired learning and memory, cognitive dysfunction, and accelerated disease progression.[162]

Pb is the second most toxic metal after Arsenic (As) and is considered carcinogenic (Group 2B) to humans.[170-172] In adults, Pb causes cardiovascular, central nervous system, kidney, and fertility problems.[171] Long-term exposure to Pb is associated with immune dysfunction and may affect the kidneys, heart, liver, brain, and lungs.[173, 174] Pb exposure has been shown to induce oxidative stress and the altered expression of genes related to inflammation. Previous studies have reported increased incidences of lung cancer among workers exposed to Pb.[174-178]

Si and Sr have not been reported as harmful to humans.[179, 180] Sr can replace Ca in bones and in teeth when entering the bloodstream,[181] but its accumulation can be slowly eliminated from the body, taking long periods.[180] Silica is used widely in the food and beverage industry as a food additive, so the human body obtains large loads of Si from dietary sources. Relatively insoluble forms of silica can release small but meaningful quantities of silicon into biological compartments. Still, Si exposure to humans is limited and largely in chemical forms that are not readily absorbed or bioavailable.[182] Opposite to toxic, silicic acid has been associated with beneficial effects for bone [183] and also to the reduction of Al toxicity and risk of Alzheimer's disease due to its high affinity to Al.[184, 185]

The dissolved amounts of metal in SLF were found to be lower than the recommended dietary allowance (RDA), and tolerable upper intake levels (UL). The average intake (AI) usually found for these elements is in the order of mg/day (Al-Al: 10 mg/day,[186] Fe-UL: 1.1 mg/day,[179] Cu-UL: 10 mg/day,[179] Sr-Al: 1.9 mg/day,[187] and Pb-UL: 1.75 mg/week[188]), except for Si, for which there is no evidence of adverse health effects or UL.[179]

In addition, the concentrations obtained were per gram of coal dust, so considering that the permissible exposure limit (PEL) for RCMD is 1 mg/m^3,[126] if we set a scenario where a mine folds five times the PEL (i.e., 5 mg/m^3), it would take a long time for a miner to inhale 1 g of RCMD. An average breath carries around 0.5 L of air [189], and the average number of respirations for a healthy adult ranges from 12 to 20 breaths per min.[190] This means that considering the extreme (20 breaths/min), a person could breathe around ~5 m^3 of air in 8 h (regular shift), resulting in a total dose of ~25 mg/8-h of RCMD, so it would take several days to achieve 1 g inhaled, not considering the fraction that is exhaled or expelled from the body. Thus, the concentrations found in the dissolution experiments are challenging to reach in short periods from RCMD, and more, concentrations in toxic levels.

However, the immediate release of these elements to the cells and the direct contact with tissues may play a role in cell damage. It was found in the literature that free Cu ions can cause cell damage, and replacements by Al^{+3} cause disturbances in cell communication and growth. Pb exposures alter the expression of genes related to inflammation, so the effects of the direct contact of these elements with the cells should be further studied to determine how they may affect their functionality and be involved in developing diseases.

4.6.8 Changes in Functional Groups

FTIR analysis was carried out on the samples after dissolution in SLF experiments. The spectra collected for the coal dust that has been dissolved in SLF and recollected

showed almost similar spectral bands to the initial spectra found in the samples before dissolution but with lower intensities. The spectra of the dust after dissolution indicate that oxygen-containing functional groups are the most consumed. The spectra obtained for samples before and after SLF dissolution are shown in **Figure 4.10,** and the peak assignments are in **Table 4.13**.

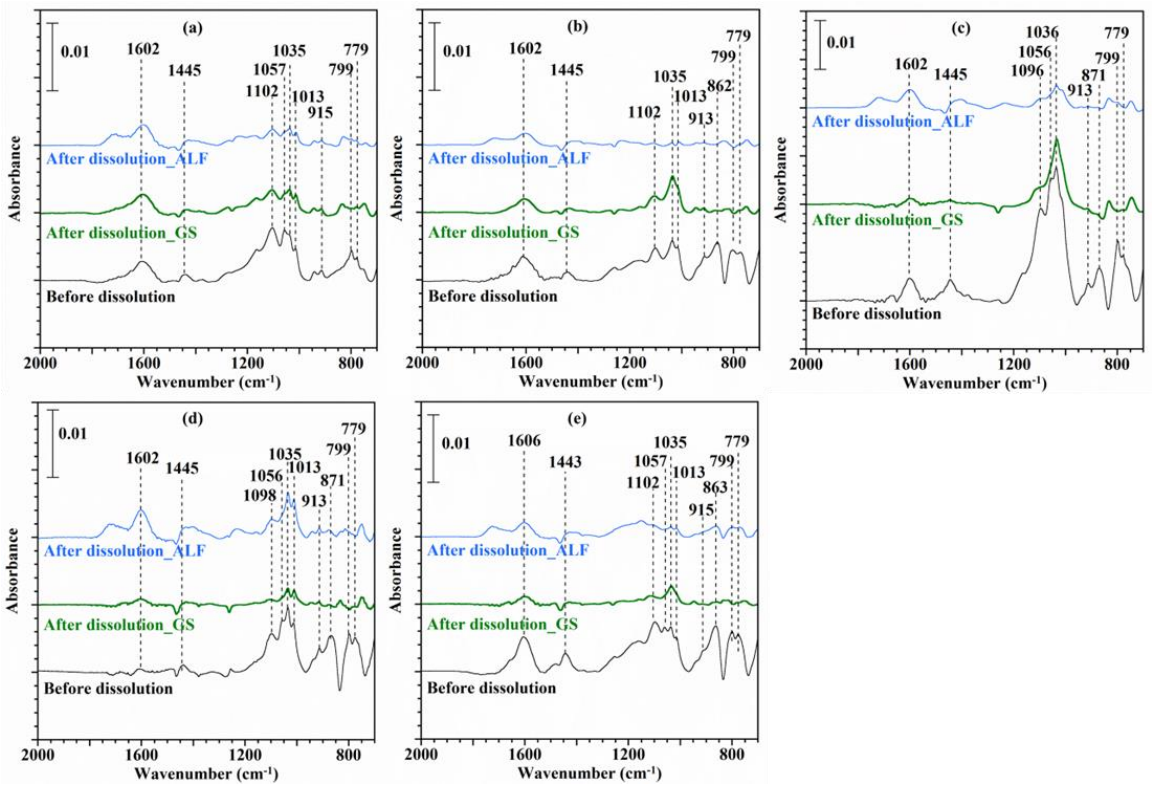

Figure 4. 10: FTIR spectra of (**a**) Mine 1, (**b**) Mine 2, (**c**) Mine 3, (**d**) Mine 4, and (**e**) Mine 5.

Table 4. 13: Peak assignments from FTIR.

Wavenumber (cm^{-1})	**Peak Assignment**
779 and 799	Quartz
913	Kaolinite
1000–1200	Si=O, Si-O-Si, Si-O-C, C-O-C
1445	Antisymmetric–CH_3 deformation
1602	Benzene C=C stretching

4.6.9 In Vitro Inflammatory Response

Existing literature has focused on the development of pulmonary fibrosis in pneumoconiosis, largely examining the role of fibroblasts in the development of CWP.[191-193] Instead of merely examining the role of fibroblasts, we assessed the impact of coal-based PM10 on epithelial (A549), neutrophilic (HL-60), and macrophage (THP-1) cells. The results of the PM10 coal dust in vitro exposures for cells HL-60, A549, and THP-1 are shown in **Figure 4.11**, **Figure 4.12,** and **Figure 4.13**, respectively.

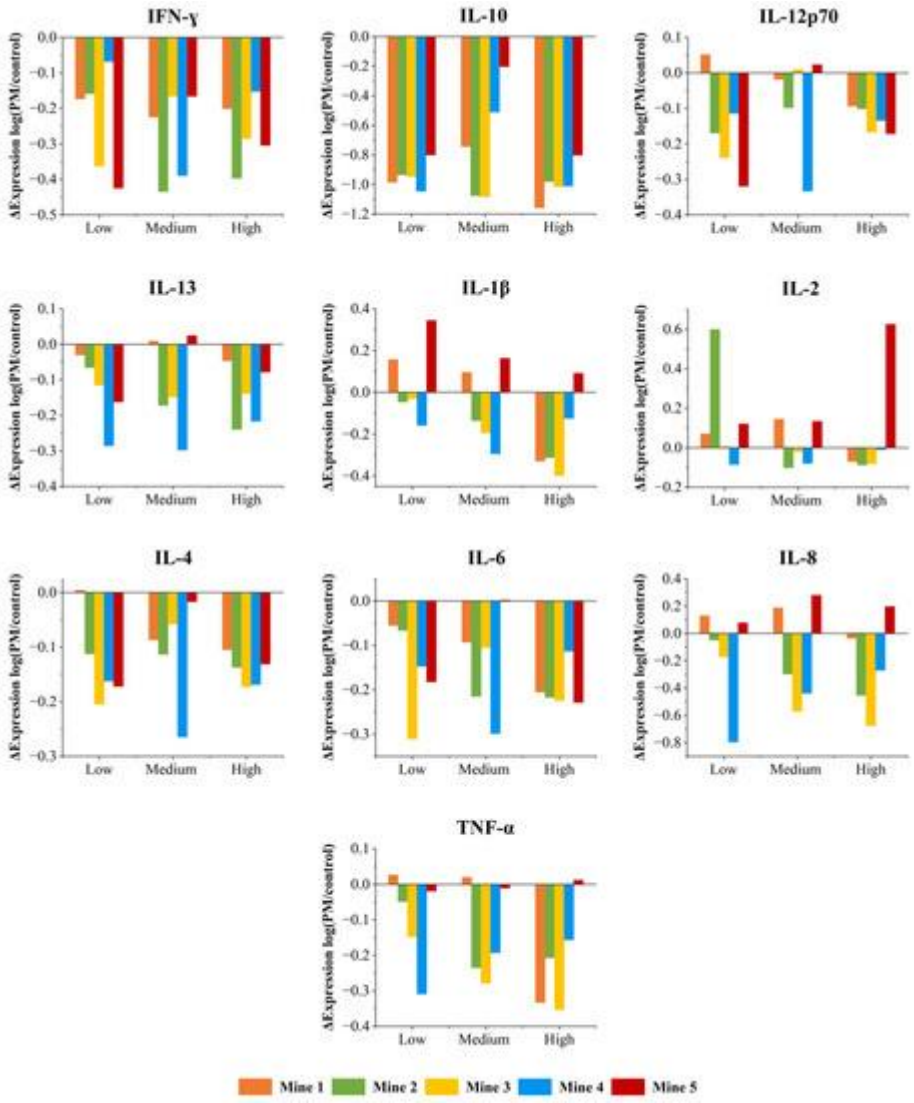

Figure 4. 11: Results of PM10 coal dust exposures to HL-60 cells using low (5 µg/mL), medium (10 µg/mL), and high (20 µg/mL) concentrations.

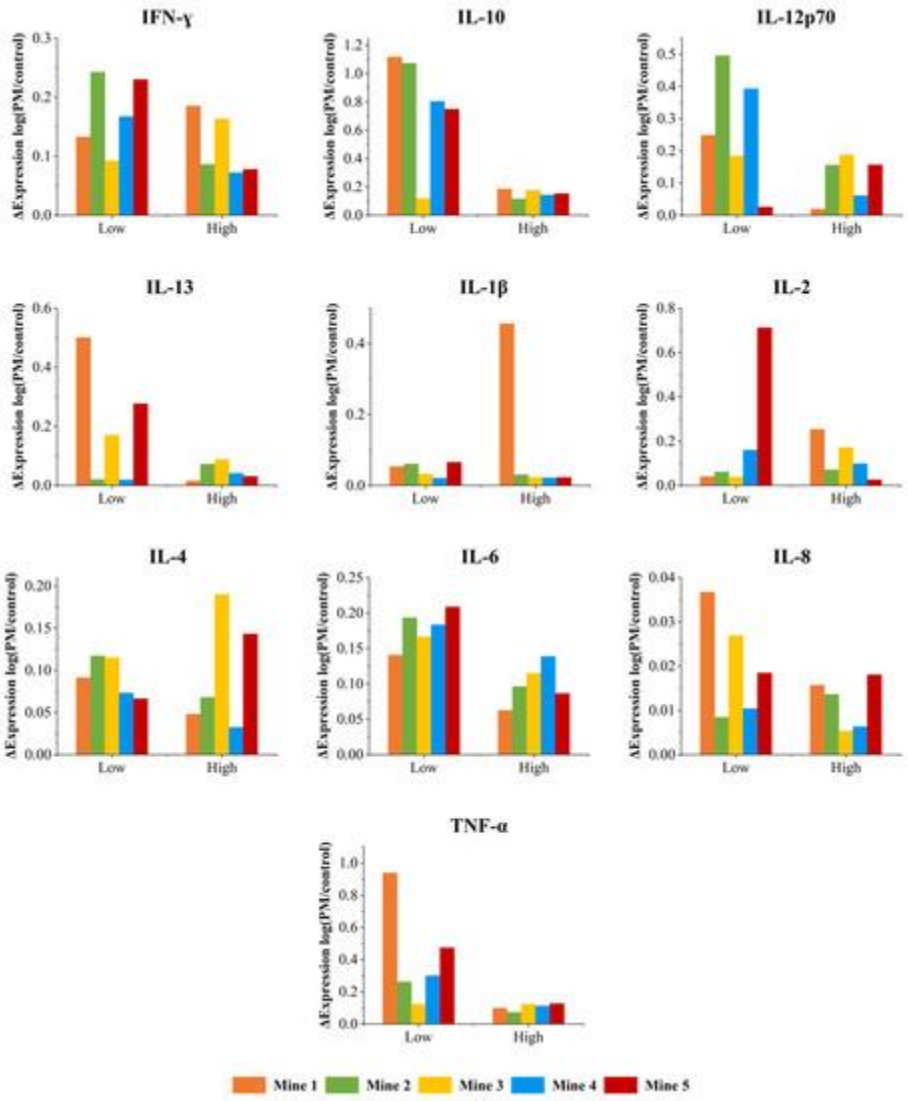

Figure 4. 12: Results of PM10 coal dust exposures to A549 cells using low (10 µg/mL) and high (100 µg/mL) concentrations.

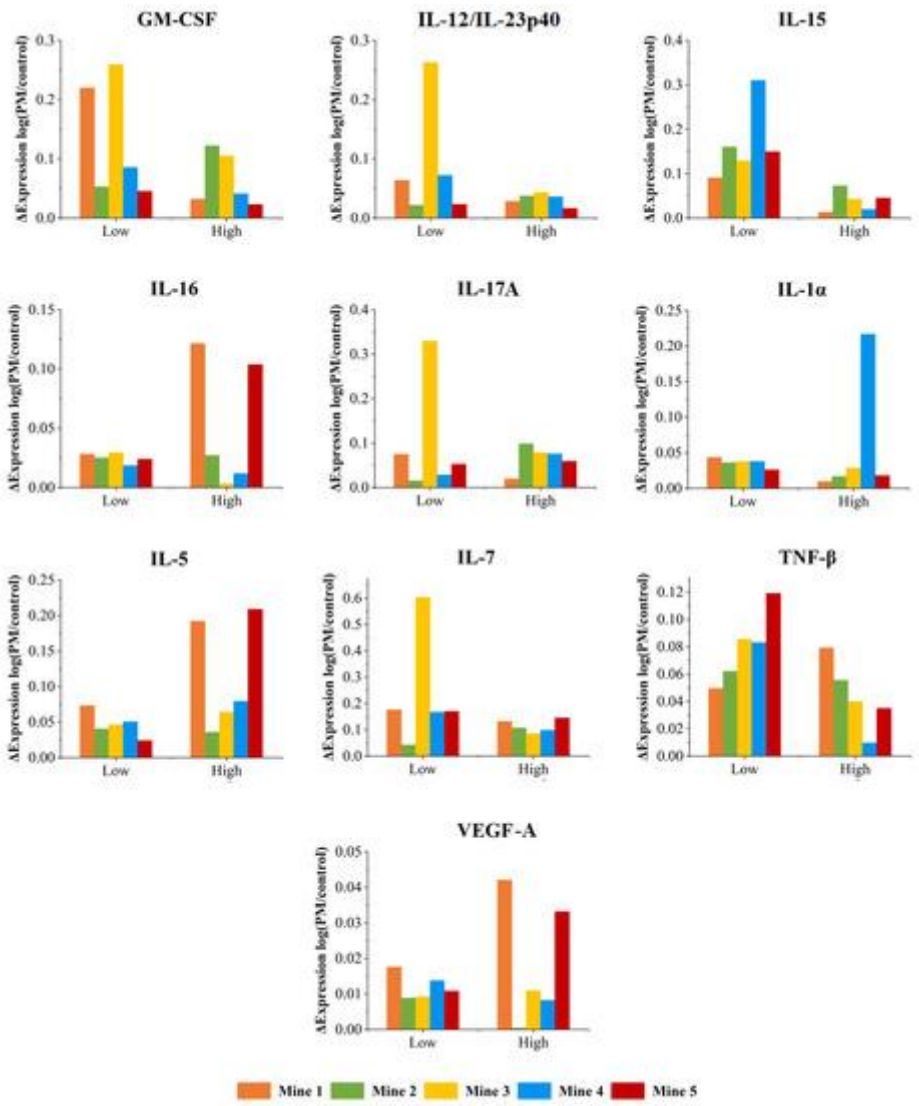

Figure 4. 13: Results of PM10 coal dust exposures to THP-1 cells using low (10 µg/mL) and high (100 µg/mL) concentrations.

After 4 h of in vitro dust exposure, HL-60 cells indicated mostly a decrease in cytokine expression. Interferon gamma (IFN-γ), interleukin-10 (IL-10), interleukin 12p70 (IL-12p70), interleukin-13 (IL-13), interleukin-4 (IL-4), and interleukin-6 (IL-6) demonstrated a diminished expression across low (5 µg/mL), medium (10 µg/mL), and high (20 µg/mL) treatment groups, relative to controls (no dust exposure). These cytokines are biological signaling molecules frequently involved in chronic inflammatory conditions, including CWP. Overall, the three concentrations did not demonstrate a dose-response, only IL-1β showed a decrease in the cytokine expression when the dose increased for almost all the mines. Interestingly, IL-2 expression mostly increased across treatment groups, with Mine 2 and Mine 5 demonstrating the greatest relative IL-2 expression. IL-8 and IL-1β indicated mixed results, with both up and downregulation across all three treatment groups.

For A549 cells, after 4 h of in vitro dust exposure, they showed an increase in cytokine expression for all the mines across both low (10 µg/mL) and high (100 µg/mL) treatment groups. IL-10 demonstrated a remarkably high increased expression when exposed to low concentrations, except for Mine 3. IL-8 showed the lowest response to the PM10 exposures, as well as IL-1β, which showed a very low upregulated expression for most of the mines, except for Mine 1 at a high concentration. IL-10, IL-12p70, IL-6, and TNF-α indicated a dose-response, showing a decreased expression when the dose was increased. The rest of the cytokines showed a mixed dose response, with both increasing and decreasing expressions when treated with a higher concentration.

THP-1 cells also displayed an increase in cytokine expression for all the mines after 4 h of in vitro dust exposure and across both low (10 µg/mL) and high (100 µg/mL) treatment groups. Overall, the two concentrations did not demonstrate a dose response. Only IL-1β showed a decrease in the cytokine expression when the dose increased.

Selected cytokines were selected based on their role in pneumoconiosis. Chronic inflammation is a key symptom of pneumoconiosis in lung tissues and bronchoalveolar lavage fluid.[194] Pneumoconiosis is characterized by pulmonary injury and the recruitment of inflammatory cells such as monocytes, macrophages, and neutrophils.[195-197] Neutrophils are known for being the most abundant leukocytes in the blood, and for that, they are used as the first line of defense in the immune system in several situations. From the circulation, they are quickly mobilized to sites of inflammation.[198, 199] In pneumoconiosis, neutrophils respond to several inflammatory cell chemoattractants generated by activated macrophages. Neutrophils migrate from the vascular compartment to the alveolar space.[195, 196] Once they are inside the alveolar space, recruited neutrophils secrete toxic oxygen radicals or proteolytic enzymes. As a result, they induce an inflammatory response by avoiding lung colonization from agents such as silica, asbestos fibers, and coal dust.[195, 196, 200]

Dust particles under 5 µm escape mucociliary clearance and deposit in the terminal bronchioles and alveoli.[200, 201] Then, lung epithelial cells play a huge role in avoiding lung colonization by these agents (silica, asbestos fibers, or coal dust). They recognize microbial molecules through specialized receptors, such as toll-like receptors, pattern recognition receptors (PRRs), and CD14 receptors.[202] The detection of foreign material by the epithelial cells triggers the immune system response, resulting in the activation of alveolar macrophages, which accept the smaller particles via phagocytosis and collect in the interstitium along the perivascular and peribronchiolar regions of the lung.[201] It also results in the release of cytokines that stimulate inflammation, such as IL-1 and TNF-α, the generation of free radicals, and the augmentation of cell-signaling pathways. As a result, the different cytokines result in the promotion of fibrosis.[200, 201, 203] Following this, once the inflammation process is complete, the fibrotic process initiates by stimulating growth factors. Then, type 1 pneumocytes grow over the collected alveolar macrophages and enclose them in the interstitium. Fibroblasts become stimulated to cause fibrosis and tissue remodeling by producing ECM and matrix metalloproteinases.[200] Fibrocytes can also induce chemotaxis and attract inflammatory factors and chemokines to increase the immune response trying to prevent the establishment of these pathogenic microorganisms.[200] By the end of the fibrotic process, there is an overproduction of

fibronectin and collagen, resulting in scar tissue formation in the lungs,[200] which is less compliant than normal lung tissue, making it harder to breathe over time. These reactions take place for years before showing any symptoms. Heppleston's theory states that the death and disintegration of macrophages engulfing dust results in fibrosis.[194]

TNF, IL-6, and IL-8 are some of the mediators that may be involved in the pathogenesis of coal workers' pneumoconiosis.[191] TNF participates in the initiation and regulation of inflammatory reactions, as well in the regulation of fibrotic reactions, while IL-6 and IL-8 in the chemotaxis and activation of lymphocytes and the chemotaxis of inflammatory cells, respectively.[191] Previous literature has found TNF-α, IL-6, and IL-1 highly related to CWP and silicosis after conducting in vitro, in vivo animals, and human studies from patients with these lung diseases.[191, 204-208] The increase in both TNF-α and IL-12p40 was associated with silicosis development and severity.[208] TNF seem to play a crucial role in the control of the inflammatory and fibrotic response of the lungs to RCMD and RCS.[191, 205, 209] Furthermore, it has been found that IL-8 (important as neutrophil attractants and adhesion molecules), is associated with PMF.[196]

Davis G.S. et al. studied IFN-γ (a lymphocyte cytokine that acts in macrophage activation) and IL-4 (involved in the differentiation of T cells and eosinophilic inflammation) in mice exposed to silica, finding an immune–inflammatory response from IFN-γ but not from IL-4.[210, 211] IFN-γ also may help in the production of fibroblast growth factors by macrophages, but its influence remains in discussion.[191]

IL-12 has multiple biological activities, and it is a key factor that drives Th1 responses and IFN- production. IL-12 may provide protection against bacterial and viral infections. IL-13, which is linked to inflammatory diseases and appears to contribute to the development of pulmonary fibrosis and the formation of granulomas, was found upregulated in a study when mice were exposed to silica, relating this cytokine to lung diseases.[212]

IL-2 is a signaling molecule involved in T-cell proliferation. Previous literature suggests that bronchoalveolar lavage fluid samples from pneumoconiosis patients have tested positive for IL-1α and β, TGF-β, IL-5, IL-2, and IL-10.[213] IL-12 has a variety of biological functions and is a critical regulator of Th1 responses and IFN-γ production; also, it may play a key role in protecting against bacterial and viral infections.[214]

In these current results, TNF-α, IL-2, IL-1β, IL-8, IL-6, and IL-10 were upregulated mainly for Mine 1 and Mine 5 in the neutrophilic cells, and for all the mines in epithelial cells, but showed a higher expression for Mine 1 and 5 as well in most of the cases. IL-1α and IL-5 in the macrophage cells were also upregulated, showing an exceptionally high expression for Mine 4 in IL-1α and for Mine 1 and Mine 5 in IL-5 at high concentrations. IFN-γ and IL-4 were upregulated in epithelial cells for all the mines but were downregulated in neutrophilic cells, not displaying any trend.

From the data obtained, in some of the cytokines studied in the neutrophilic cells, an immune suppressive effect was found (a downregulated response), but in general, the cytokines of the epithelial, macrophage and some of the neutrophilic cells showed an upregulated response, indicating an inflammatory response when exposed to low and high

concentrations of PM_{10} coal dust. This inflammatory response obtained from most of the cytokines may have led to the activation of the mechanisms mentioned that produce scar tissue formation and, thus, lung diseases. Results also indicate that Mine 1 and Mine 5 may produce higher inflammatory stimulation since they were found consistently upregulated and/or with a higher expression in the cytokines that the literature links to inflammation and pneumoconiosis. Based on our results, further research is warranted on cytokine production in non-fibroblast cell types in pneumoconiosis models, including neutrophils, lung epithelial cells, and macrophages.

4.7 Conclusions

This study provides characterization and bio-accessibility information on RCMD from two regions in the US (the Appalachian region and the Rocky Mountains). This study analyzed the characteristics and toxicity of the RCMD fraction coming only from the coal seam and compared the differences of samples coming from the Appalachian region and the Rocky Mountains to identify the existence of trends related to the geographic location. From the results obtained, the following conclusions are made.

The particle size distribution of the samples showed to be finer for those coming from the Appalachian region. Appalachian region samples were suggested to have more minerals and higher elemental concentrations, which would indicate that these samples would be more resistant to the reduction process, but otherwise, as expected, these samples reached finer samples when reduced under the same procedure. Even particles smaller than 1 micron were found for samples from the Appalachian region but not for samples from the Rocky Mountains.

The XRD experiment showed that quartz, kaolinite, and pyrite were the main mineral components of the samples. These results were in accordance with the elemental content results, where Si, Al, and Fe were the elements with higher concentrations in the samples and the main element components of the minerals observed in the XRD. Additionally, XRD and elemental content results showed that samples from the Appalachian region had more mineral and elemental contents compared to the samples from the Rocky Mountains.

As for XRD analysis, Si followed the same trend for its exposure on the surface as the elemental content, but Al did not show any trend related to the initial concentration or the geographic location, indicating that not the same proportion of Al was exposed in the particle surfaces and that Al atoms may be packed inside the particles or the distinct layers of the clay minerals (kaolinite). Fe was not observed in the particle surfaces, but it was dissolved later in the dissolution experiment, so the Fe atoms, even if they were not exposed in the surface, were reached by the SLFs and partially digested.

Kaolinite and quartz showed decreases in the peaks of the FT-IR spectra after dissolution in both GS and ALF, indicating that the SLFs were digesting these minerals and the dissolution of Al and Si obtained in SLF came from them. The main factors influencing the dissolutions were the pH of the SLF and the initial availability of the elements in the samples. The specific surface area did not affect the general behavior of the dissolutions.

The elements with the higher availability in the samples (AL, Si, and Fe) gave the higher total dissolutions in the SLFs, but the percentage dissolved from the initial contents did not exceed 0.5% in most of the cases. In contrast, Cu (trace elements) was dissolved from 1.2 to 5.9% of the initial content in the samples, so it can be concluded that normalized to the initial availability, Cu is more bio-accessible than the other elements.

The toxicity of the samples based on the metal dissolutions could not be related to the geographic location since the factors influencing the dissolutions in SLF varied from the different samples and within the elements dissolved. So, the higher incidence of lung diseases in the Appalachian region may be related to other factors such as the exposure to RCMD, the particle size distribution of the actual RCMD in each mine, and the mineral contributions from the different sources in the mine to the RCMD that the miners inhale, which may be significantly different in each region.

In vitro studies indicated a proinflammatory response of the cytokines studied, especially in the epithelial and macrophage cells, which suggests possible participation from these cell types in pneumoconiosis and lung disease development.

4.8 Acknowledgement

The authors thank Maria Pineda, and Carlha Barreto for helping with the sample preparation, and Virgil Lueth, Bonnie Frey, and Kelsey McNamara at the New Mexico Bureau of Geology for providing training to perform XRD and total microwave digestion experiments.

Permission

Reprinted (adopted) and does not require specific permission for reprint in the dissertation.

SALINAS, V.; DAS, M.; JACQUEZ, Q.; CAMACHO, A.; ZYCHOWSKI, K.; HOVINGH, M.; MEDINA, A.; RUBASINGHEGE, G.; REZAEE, M.; BALTRUSAITIS, J.; FAIRLEY, N.; ROGHANCHI, P. CHARACTERIZATION AND TOXICITY ANALYSIS OF LAB-CREATED RESPIRABLE COAL MINE DUST FROM THE APPALACHIANS AND ROCKY MOUNTAINS REGIONS. ***Minerals 2022***, 12, 898.

CHAPTER 5

A COMPARATIVE TOXICOLOGICAL STUDY OF LAB CREATED COAL MINE DUST FROM VARIOUS SOURCES WITHIN THE SAME MINE

5.1 Abstract

RCMD exposure is one of the utmost health hazards to the mining community causing various health issues, including coal worker pneumoconiosis (CWP). Considering multiple potential sources of RCMD having different physicochemical properties within the same mine suggests a wide range of health impacts, yet not been studied extensively. In this study, we investigate the toxicity of lab-created RCMD based on different sources; coal seam, rock dust, host floor, and host roof collected from the same mine. Comparative samples obtained from several mines situated in various geographic locations were also assessed. This work quantifies metal leaching in simulated lung fluids and correlates dissolution with in-vitro immune responses. Here, dissolution experiments were conducted using two simulated lung fluids; gamble solution (GS) and artificial lysosomal fluid (ALF). In-vitro studies were performed using a lung epithelial cell line (A549) to investigate their immune responses and cell viability. Si and Al are the most dissolved metals, among several other trace metals Fe, Sr, Ba, Pb, etc. RCMD from the coal seam and the rock dust showed the least metal leaching, while floor and roof dust dissolved the most. Results from in-vitro studies showed a prominent effect on cell viability for floor and roof dust samples suggesting high toxicity.

5.2 Introduction

A major health risk to the mining industry is respirable coal mine dust (RCMD).[126] Workers in coal mines are exposed to a significant amount of RCMD that has been released into the mine's atmosphere as a result of different routine activities, such as cutting, drilling, blasting, and transportation.[17-19] Exposure to an elevated concentration of RCMD can lead to numerous diseases among coal workers and residential communities in close proximity. The diseases include silicosis, coal workers' pneumoconiosis (CWP), mixed dust pneumoconiosis, dust-related diffuse fibrosis (DDF), progressive massive fibrosis (PMF), emphysema, and chronic bronchitis, all of which can be fatal in the worst case scenario.[18, 55] Although limited work has been reported recently to limit exposure to RCMD, lung disorders brought on by RCMD still pose a serious threat to the coal mining industry. Early in the new millennium, it was discovered that CWP was becoming more common and severe.[18, 29, 55]

According to its definition, RCMD is defined as airborne particulate matter with a particle size of less than 10 micrometers or having an average aerodynamic diameter of 4 micrometers.[4, 126-129] Inhalation is the primary exposure method to RCMD.[126] While particles larger than 10 micrometers can be cleared to the gastrointestinal tract, particles smaller than 4 micrometers can pass through the nasal filtration system and can reach the deep lung in the alveolar region.[2] There, they can deposit in two partitions of the lung: the acidic environment of the alveolar macrophages and the nearly neutral extracellular environment of the lungs' interstitial fluid.[11, 101, 102, 104, 215] Despite the fact that numerous studies have clearly linked RCMD exposure levels and exposure times to the development of pneumoconiosis, many studies also imply that RCMD toxicity depends on multiple chemical and physical properties other than the concentration of RCMD.[4, 6, 29, 32-37] Although the chemical and physical characteristics of RCMD are very much site-specific and may cause various toxicity levels, research into toxicity based on the source of RCMD is still quite limited.[4]

Furthermore, numerous studies have linked the metal leaching capacity of dust particles, which may make it available for subsequent interactions with related body tissues and trigger inflammatory responses, to the toxicity of the dust particles.[2-4] Studies show that the amount of metal that might leach into physiological fluids depends on a number of physicochemical properties of the dust itself, including particle size and shape, mineralogy, and chemical composition.[2, 3] The source of the dust, which controls many of the physicochemical characteristics of the dust, is therefore essential in establishing the toxicity of any particular dust. Thus, the current study focuses on the toxicity of respirable coal mine dust (RCMD) based on its ability to leach metals and the inflammatory response in connection to its particular sources. Here, metal leaching tests were carried out for the RCMD samples obtained from three different mines in simulated lung fluids (SLF), including Gamble Solution (GS) and Artificial Lysosomal Fluid (ALF), as well as in-vitro reactions. Each mine's coal seam, host floor, and host roof served as the sources for the RCMD samples since their physicochemical composition can vary, potentially producing various RCMD. Additionally, rock dust, which primarily consists of stable oxides like silicates and carbonates, is used in underground coal mines to control the spreading of fire, which are another possible source of RCMD.[216-219] Further, the current study investigates RCMD produced from the rock dust gathered from each mine.

5.3 Materials and Methods

5.3.1 Dust Samples Collection and Preparation

Samples were collected from the coal seam, floor, roof, and rock dust within the same mine. Table 1 summarizes bulk sample information directly collected from the mine.

Table 5. 1: Details on the samples used in this study

Mine ID	Mining Method	Source	Sample ID
Mine 1	Long wall	Coal	Mine 1_Coal
		Continuous miner machine floor	Mine 1_Floor
		Rock dust	Mine 1_RD
		Continuous miner machine roof	Mine 1_Roof
Mine 2	Room & Pillar	Coal	Mine 2_Coal
		Host floor	Mine 2_Floor
		Host roof	Mine 2_Roof
Mine 3	Room & Pillar	Coal	Mine 3_Coal
		Host floor	Mine 3_Floor
		Rock dust	Mine 3_RD
		Host roof	Mine 3_Roof

During a shift, a miner inhales aerosolized materials. The goal of the bulk sample collection was to establish a representative collection of these substances. Coal samples were collected directly from the coal seam, while floor samples were taken from the mine floor. We also collected roof samples from the roof of the continuous machine and samples from rock dust. It should be noted that Mine 2 lacks a sample of rock dust due to that particular mine did not have any.

The bulk sample was first reduced to a smaller sized particles using a jaw crusher or a mortar and pestle until it completely passed through the U.S. standard sieve No. 6. (ASTM E11). The sample was then ground using media of zirconia 1/2" x 1/2" radius end cylinder, magnesia stabilized, in a 755RMV jar mill with dimensions of 9.5 inches in diameter and 8.5 inches in height. To eliminate the large particles that the mill could not reduce, the material was first ground for 6 hours and sieved using a U.S.A. standard sieve No. 120 (opening 125 μm). The material that passed through the sieve was then pulverized for an additional six hours. The material was additionally crushed with a RETSCH XRD-Mill McCrone, which maintains the structure of the coal samples during the reduction process, in order to achieve a greater fraction of particles smaller than 10 μm. Using agate as the grinding medium, the operation was carried out in four steps over the course of five minutes. Last but not least, a next-generation cascade impactor (NGI, model 170 NGI, from MSP Corporation) with an attached aerosol generator and gravimetric stages were used to separate the samples smaller than 10 μm fraction (mass mean aerodynamic diameter). A pump made by Copley Scientific that was set to flow at a flow rate of 60 L/min for 4 secs was used to draw dust samples through an induction port after they had been weighed,

loaded, and sealed inside hydroxypropyl methylcellulose capsules. The fractions smaller than 10 μm were gathered from various stages and used for future investigations.

5.3.2 Dust Characterization

The surface areas of the dust samples were determined using a 7-point N_2 adsorption Brunauer-Emmet-Teller (BET) isotherm following outgassing at 150˚C for 16 hours each. The particle size distributions of the dust samples were determined from the SEM images using the software package ImageJ. The mineral components of the dust sample were identified from the X-ray diffraction pattern collected using a PANalytical X'Pert Pro diffractometer (PANalytical B.V., Almelo, The Netherlands) equipped with a Cu Kα source.

The surface functional groups of the dust samples were determined using a Nicolet iS50 series FTIR coupled with a Ge-ATR crystal. The sample preparation for the FTIR-ATR analysis was done in a 2 mL centrifuge tube using ~10 mg of the dust samples and about 1 mL of isopropyl alcohol (IPA). The suspension of dust samples in IPA was then sonicated for 20 minutes and transferred to the ATR crystal using a Pasteur pipette, followed by overnight drying. FTIR spectra were collected using 250 scans at 4 cm^{-1} resolutions. The collected FTIR spectra were processed to the spectrum of bare crystal and only reported the processed spectra.

The elemental composition of metals in the dust samples was obtained using an inductively coupled plasma mass spectroscopy (ICP-MS, Agilent 7900) following the SK-PE-017 method. The microwave-based acid digestion method for coal samples designed in two steps. In the first step, up to 200 mg of the dust samples was weighed and added to individual digestion tubes, followed by 10 mL of concentrated nitric acid. The microwave program we used was a 10-minute ramp to 190˚C and held the temperature for 15 minutes with a 1200 W system power. In the second step, 2 mL of concentrated trace metal grade hydrofluoric acid was added, followed by a microwave program with a 20-minute ramp to 230˚C, and held it for the next 15 minutes. A standard material CLB-1 from the USGS was used with each batch as a reference for the digestion method.[95] The digested samples were filtered and diluted to analyze using the ICP-MS.

5.3.3 Toxicological Study

Toxicological assessments of the coal dust samples were performed using dissolution studies in simulated lung fluids in combination with in-vitro studies using corresponding cell lines.

5.3.4.1 Dissolution Study in SLFs

Dissolution studies of the coal dust samples in simulated lung fluids (SLFs) were performed using a similar method described in our previous studies.[2, 4] We used a custom-built glass reactor equipped with a removable airtight top inside a dark room. Two simulated lung fluids, Gamble's solution (GS) mimicking the interstitial lung environment and artificial lysosomal fluid (ALF) mimicking the acidic environment inside macrophages, were used to study the metal leaching from the coal dust. We used a dust loading of ~20 mg in 100 mL of the SLFs. Before adding the dust, SLFs were purged with

oxygen to maintain an oxygenated environment. The reaction vessels were equipped with a heated water jacket to control the temperature at 37˚ C with continuous mixing using a magnetic stirrer. During the reaction, a suspension aliquot of 1.5 mL was collected periodically using a disposable syringe connected to a 12 cm-long Teflon tube. The collected samples were centrifuged, filtered, and stored in the fridge. Then the collected samples were subjected to ICP-MS analysis to determine the dissolved metal concentration. All these dissolution experiments were performed in triplicates and reported only the average dissolved metal concentration with one standard deviation.

5.3.4.2 In-vitro Study

A549 is a human lung carcinoma epithelial cell line obtained from American Type Culture Collection (ATCC). We cultured the cells with Dulbecco's modified Eagle's medium (DMEM) with L-glutamine and supplemented with 10% fetal bovine serum. The cells were maintained in a 37°C humidified atmosphere of 95% air and 5% CO_2. The coal dust samples were first autoclaved and then suspended in the cell culture media. Before use, coal dust suspension was sonicated for 20 minutes.

When there was enough growth of cells, media was aspirated, and washed the cells with phosphate buffer solution (PBS). PBS was also aspirated, and Trypsin-EDTA solution was added to the flask. Then it was incubated for 8 minutes. After all the cells started to float, the media was added to inactivate the trypsin. The cells were counted by preparing a mixture of trypan blue and cell media of 1:1 using a cell counter. 20 mL cell-media mixture was prepared such that the concentration of cells became 20,000/mL. This was mixed well, and 100 µL was introduced in each well of the 96-well plate. They were allowed to adhere overnight inside the incubator. After 24 hours, the media was changed and treated the cells with coal dust suspension to make the final concentration of 25, 50, and 100 µg/mL. 10 µg/mL of Polyarsine oxide (PAO) was used as the positive control, and for the negative control, cells were kept untreated. The cells were then incubated for 48 hours and treated with 20 µL of MTT solution (5 mg/mL) without removing the media. It was again incubated, and after 2 hours, when the crystals formed, the supernatant solution was removed. The crystals were dissolved in DMSO by mixing with a multichannel micropipette. The absorbance was measured at 490 nm using a microplate reader.

5.3.4 Standards and Chemicals

All chemicals used for this study were reagent grade or better, and standards were used as received. The standard material CLB-1 from USGS was used as a reference during the elemental analysis. All the chemicals used in this study are listed in the following sections.

5.3.4.1 Materials Used for Dissolution Study

Both gamble solution (GS) and artificial lysosomal fluid (ALF) for the dissolution study were prepared using the method discussed in previous studies.[2, 4, 138] All solutions were prepared in purified water (18.2 MΩ, Milli-Q-A10). The following chemicals were used for the media preparation. Sodium chloride (NaCl, Acros, +99.0%), Disodium hydrogen phosphate (Na_2HPO_4, Sigma-Aldrich, +99.0%), Sodium bicarbonate

($NaHCO_3$, Sigma, 99.5%), Trisodium citrate dihydrate ($C_6H_5Na_3O_7.2H_2O$, Sigma-Aldrich, +99%), Ammonium chloride (NH_4Cl, VWR International, 99.5%), Glycine (NH_2CH_2COOH, Aldrich Chemical Company, +99%), Sodium dihydrogen phosphate (NaH_2PO_4, Sigma-Aldrich, +99.0%), L-cysteine ($C_3H_7NO_2S$, Aldrich Chemical Company, 99%), Sodium hydroxide (NaOH, VWR International, 97%), Citric acid monohydrate ($C_6H_8O_7.H_2O$, Fluka Analytical, +99%), Calcium chloride dihydrate ($CaCl_2.2H_2O$, Fisher Scientific, +99%), Sodium sulfate (Na_2SO_4, Sigma-Aldrich, +99%), Magnesium chloride hexahydrate ($MgCl_2.6H_2O$, Sigma-Aldrich, +99%), Disodium tartrate dihydrate ($C_4H_4Na_2O_6.2H_2O$, Honeywell Riedel – de Haen, 99.5%), Sodium L- lactate ($C_3H_5NaO_3$, Sigma, 98%), Sodium pyruvate ($C_3H_3NaO_3$, Sigma-Aldrich, +99%).

5.3.4.2 Materials Used for In-vitro Study

The following chemicals were used for the MTT assays and the media preparation. Dulbecco's Modified Eagle's Medium (DMEM) with L-Glutamine (Quality Biological, VWR), Fetal Bovine Serum (Avantor Seradigm, VWR), 0.25% Trypsin-EDTA 1X (Gibco, VWR), Dulbecco's Phosphate Buffered Saline 1X without Calcium & Magnesium (Quality Biological, VWR), Trypan blue stain 0.4% (Invitrogen, Thermo-Fischer Scientific), 96-well tissue culture plate (Avantor, VWR), Dimethyl sulfoxide 99.9% (VWR life science, VWR), phenylarsine oxide (Spectrum chemical, VWR), 3-(4,5-Dimethylthiazol-2-yl)-2,5-diphenyltetrazolium bromide (MTT) 98% (VWR life science, VWR).

5.4 Results and Discussion

5.4.1 Results for the Particle Characterization

The shape and size distribution of the dust particles were analyzed using SEM images. A representation of the SEM images is illustrated in **Figure 5.1.** These confirm the particles' irregular shape and micron-to-submicron size distribution. More than 400 particles were measured using the ImageJ software program for each sample to generate the particle size distribution. **Figure 5.2** and **Table 5.2** report the size distributions, showing particles with an average size of 1.55 to 3.80 micrometers. Additionally, we estimated the PM_{10} and PM_4 fractions. The results indicated nearly all of the particles were PM_{10} and that more than 60% of the particles were PM_4, which can be as high as 97.8%.

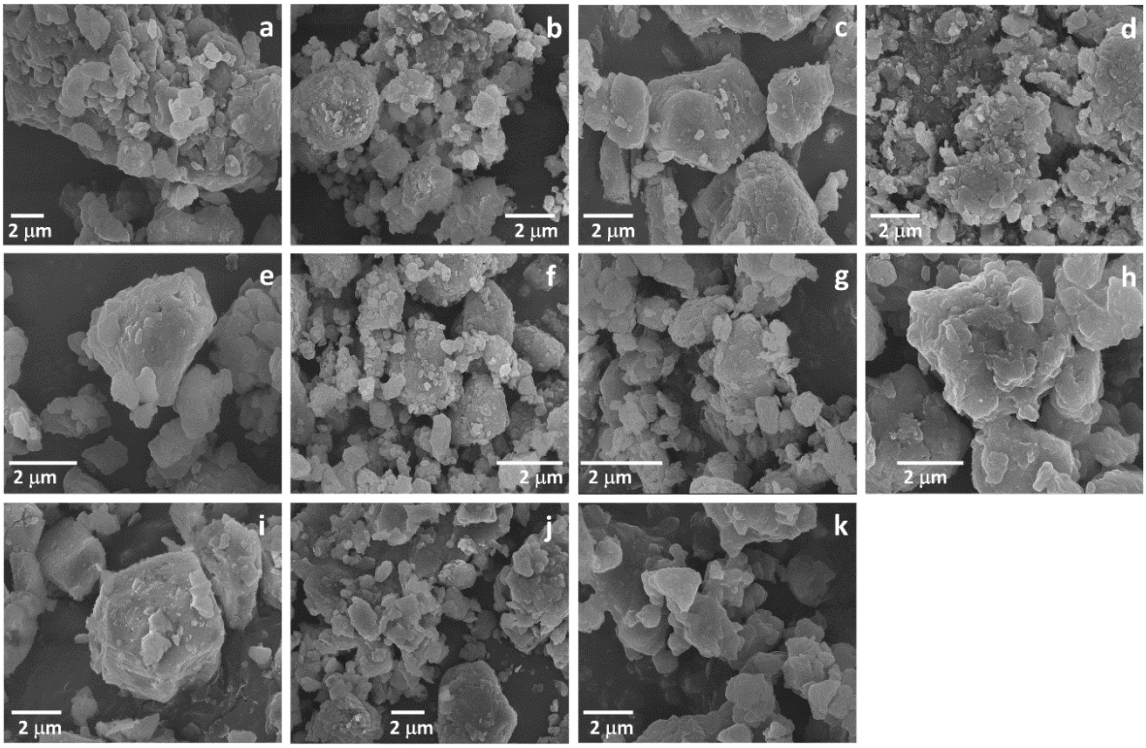

Figure 5. 1: SEM images for the lab generated RCMD (a) Mine 1_Coal (b) Mine 1_Floor (c) Mine 1_RD (d) Mine 1_Roof (e) Mine 2_Coal (f) Mine 2_Floor (g) Mine 2_Roof (h) Mine 3_Coal (i) Mine 3_Floor (j) Mine 3_RD (k) Mine 3_Roof.

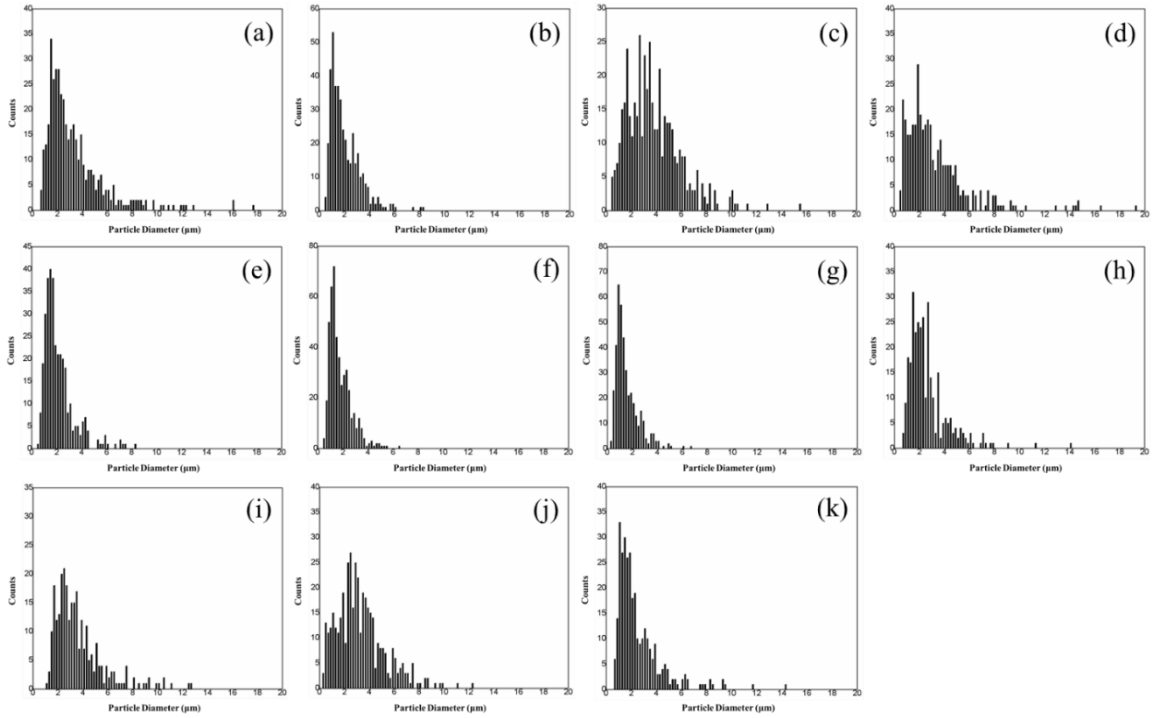

Figure 5. 2: Particle size distribution, prepared from the SEM images, for samples (a) Mine 1_Coal (b) Mine 1_Floor (c) Mine 1_RD (d) Mine 1_Roof (e) Mine 2_Coal (f) Mine 2_Floor (g) Mine 2_Roof (h) Mine 3_Coal (i) Mine 3_Floor (j) Mine 3_RD (k) Mine 3_Roof.

Table 5. 2: Size distribution calculated from the SEM images.

Sample	Average Particle Size (μm)	PM10 (%)	PM4 (%)
Mine 1_Coal	3.36 ± 2.42	97.4	74.3
Mine 1_Floor	3.31 ± 2.74	97.3	73.5
Mine 1_RD	3.80 ± 2.13	98.2	60.3
Mine 1_Roof	2.03 ± 1.20	100.0	94.2
Mine 2_Coal	2.17 ± 1.25	100.0	91.0
Mine 2_Floor	1.79 ± 0.90	100.0	97.0
Mine 2_Roof	1.55 ± 0.94	100.0	97.8
Mine 3_Coal	2.68 ± 1.65	99.4	84.1
Mine 3_Floor	3.65 ± 2.01	97.8	70.0
Mine 3_RD	3.29 ± 1.93	99.5	71.7
Mine 3_Roof	2.55 ± 1.82	99.4	86.4

As expected, Quartz is the only mineral common in all the samples, per the XRD data shown in **Table 5.3**. All samples, with the exception of those taken from the Mine 2 floor and rock dust samples, also include kaolinite. Other minerals common among several samples were pyrite, muscovite, and calcite. There were also trace levels of chlorite and dolomite, while siderite was identified in the Mine 1_Roof. Only Mine 1_Floor sample contained illite and microcline. It is also crucial to be aware that the instrument's detection range is only 1 to 2%, meaning that any minerals with lower abundances than this range were not reported in this work. The surface areas of the samples were also determined using a 7-point N_2 adsorption isotherm, and they are shown in **Table 5.4**. This shows that, despite having a very similar size distribution, the coal dust samples gathered from the various sources have a broad range of specific surface areas starting from 4.10 m^2/g to 39.85 m^2/g. Particularly, samples from the coal seam and rock dust tend to have lower surface areas than floor and roof dust samples.

Table 5. 3: Mineral composition of the coal dust samples from XRD results.

Sample ID	Q	K	P	I	Mu	M	Ch	Ca	D	S
Mine 1_Coal	√	√	-	-	-	-	-	-	-	-
Mine 1_Floor	√	√	-	√	-	√	-	-	-	-
Mine 1_RD	√	-	-	-	-	-	√	√	√	-
Mine 1_Roof	√	√	-	-	√	-	-	-	√	√
Mine 2_Coal	√	√	√	-	-	-	-	√	-	-
Mine 2_Floor	√	-	-	-	√	-	√	√	-	-
Mine 2_Roof	√	√	√	-	√	-	√	-	-	-
Mine 3_Coal	√	√	-	-	√	-	-	√	√	-
Mine 3_Floor	√	√	√	-	√	-	-	-	-	-
Mine 3_RD	√	-	-	-	-	-	-	√	-	-
Mine 3_Roof	√	√	√	-	√	-	-	-	-	-

*** Quartz (Q), Kaolinite (K), Pyrite (P), Illite (I), Chlorite (Ch), Muscovite (Mu), Microcline (M), Calcita (Ca), Dolomite (D), Siderite (S)

Table 5. 4: BET surface area measurements for the coal dust samples.

Samples	Average Surface area (m2/g)
Mine 1_Coal	6.91 ± 0.15
Mine 1_Floor	10.01 ± 0.17
Mine 1_RD	4.72 ± 0.03
Mine 1_Roof	18.59 ± 0.14
Mine 2_Coal	8.46 ± 0.15
Mine 2_Floor	38.46 ± 0.19
Mine 2_Roof	39.85 ± 0.26
Mine 3_Coal	6.89 ± 0.14
Mine 3_Floor	37.25 ± 0.09
Mine 3_RD	4.10 ± 0.05
Mine 3_Roof	14.76 ± 0.04

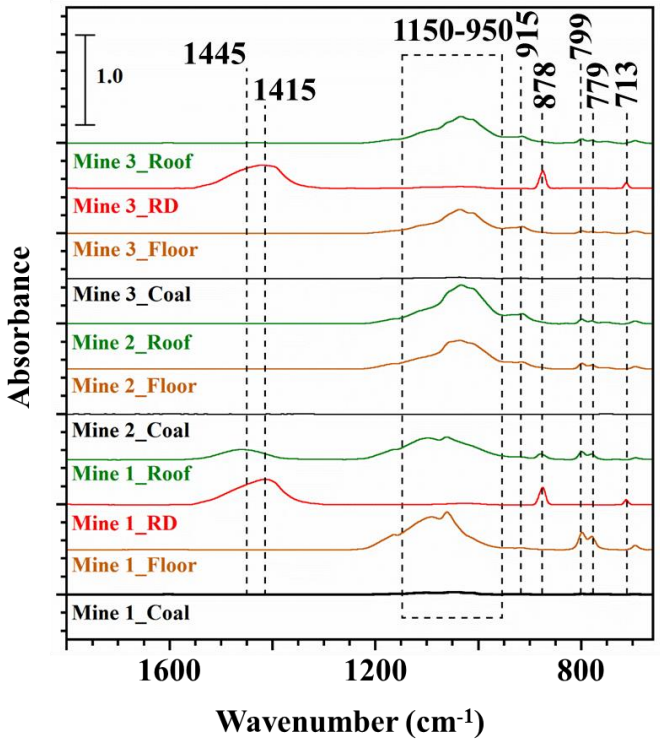

Figure 5. 3: FTIR spectra of the coal dust samples.

Additionally, the surface functional groups were identified using the FTIR spectra and reported in **Figure 5.3,** with the peak assignments presented in **Table 5.5**. The doublet at 799 and 779 cm^{-1} corresponds to the symmetric stretching of the Si-O-Si in representing the presence of low temperature quartz in all the samples, which agrees with the findings from the XRD data.[143] Further, a peak at 878 cm^{-1} corresponds to C-O bonds in carbonate, which is present only for the rock dust samples. Further, it is also evident that spectra of rock dust samples have peaks at 713 and 1415 cm^{-1}, likely due to the N-H bending and stretching for the nitrates, respectively.[143] The small peak at 915 cm^{-1} represents the presence of kaolinite, a common clay mineral in the samples. Further, the absorption band at 950 to 1150 cm^{-1} represents the oxygen-containing functional groups such as S=O, Si-O-Si, Si-O-C, which is most apparent for the samples gathered from the floor or roof. Further, the peak at 1445 cm^{-1} is also not prominent for most of the samples, indicating the presence of an aliphatic $–CH_3$ functional group.[143] It is also important to note that the samples collected from the coal seam tend to have the least functional groups on the surface.

Table 5. 5: FTIR peak assignments.

Experimental Peaks at cm-1	Standard Peaks at cm-1	Peak assignments
779 & 799	800 & 780	Silica
713	718	N-H bending
878	878	C-O bonds in carbonates
915	915	Kaolinite
950-1150	-	S=O, Si-O-Si, Si-O-C, C-O-C
1445	1445	Antisymmetric –CH3 deformation
1415	1412	C-N/N-H for nitrates

Our results for the elemental analyses are shown in **Table 5.6**. In total, 30 elements were examined in each sample, but only those that showed signs of dissolution in the lung fluids were reported. The data for the quality control sample SRM-CLB 1 presented here is an average of five trials, and for the majority of measurements, the error was within the permitted range previously reported.[95] The dust particles' elemental composition indicates that Si, Al, and Fe were the main components, along with other trace metals like Cr, Sr, Ba, and Pb. Furthermore, it is clear that dust collected from the floor or the roof of all three mines contains more silicon than dust from coal seams or rock. Furthermore, it was discovered that roof and floor dust had more significant iron contents than the other two types.

Table 5. 6: Elemental composition of samples.

Samples	% elemental concentration								
	Al	Si	Cr	Mn	Fe	Cu	Sr	Ba	Pb
Mine 1_Coal	1.307	5.276	0.002	0.000	0.121	0.002	0.004	0.0223	0.004
Mine 1_Floor	0.793	27.233	0.004	0.001	0.201	0.001	0.002	0.023	0.001
Mine 1_RD	0.020	1.457	0.000	0.039	0.177	0.001	0.004	0.001	0.013
Mine 1_Roof	0.802	25.434	0.006	0.072	2.064	0.003	0.008	0.030	0.002
Mine 2_Coal	0.114	0.507	0.001	0.000	0.190	0.001	0.010	0.003	0.005
Mine 2_Floor	0.481	24.997	0.009	0.016	1.687	0.004	0.005	0.034	0.002
Mine 2_Roof	0.646	23.786	0.009	0.006	1.105	0.005	0.026	0.044	0.003
Mine 3_Coal	1.115	4.331	0.004	0.001	0.677	0.002	0.001	0.005	0.024
Mine 3_Floor	0.771	23.469	0.012	0.004	1.893	0.008	0.035	0.044	0.007
Mine 3_RD	0.060	1.614	0.000	0.006	0.158	0.000	0.009	0.001	0.000
Mine 3_Roof	0.693	17.016	0.008	0.018	9.364	0.005	0.008	0.034	0.022
SRM_CLB 1	0.633	1.227	0.001	0.001	0.810	0.001	0.006	0.004	0.001

5.4.2 Results from the Dissolution Study in SLFs

We carried out dissolution experiments for all the lab-created coal mine dust samples in Gamble's solution (GS) and artificial lysosomal fluid (ALF). The mass-normalized amounts of dissolved metals in GS are shown in **Figure 5.4,** while those in ALF are shown in **Figure 5.5**. Si was the most dissolved element in GS from all the samples, as shown in **Figure 5.4**, while Al was also significantly dissolved in most instances. For the most part, all other metals did not disintegrate. However, in addition to Al and Si, mass normalized dissolution in ALF reveals a significant concentration for metals such as Fe, Cu, Sr, Mn, Ba, and Pb. The slightly more acidic pH of the ALF media, which supports the proton-promoted metal leaching, is likely to blame for the higher dissolution of all metals except Si in ALF.[4, 58] Quartz (SiO_2), an acidic oxide that tends to dissolve more in basic solutions, may account for a sizeable portion of the Si, causing a higher dissolution in GS.[144] As a result, the pH of Gamble's solution, which is slightly alkaline (pH - 7.3), favors the dissolving of Si, making it potentially bio-accessible. However, as demonstrated in **Table 5.7** and **Table 5.8**, the extent of metal dissolution in each solution is not only influenced by the solution pH. It is evident that four samples taken from the same mine show differences in the metal leaching in the same dissolution medium. Additionally, samples taken from similar locations but from different mines show noticeable differences in metal dissolution. Remarkably, most of the samples taken from the floor and roof exhibit greater mass-based dissolution than those taken from the coal

seam and the rock dust. Characterizations indicate that this pattern may be due to the fact that dust from floors and roofs has a larger surface area than dust from coal seams and rock dust. Hence, the floor and roof dust can potentially be more hazardous than the coal and rock dust on a mass basis because of their higher specific surface area, even though sample preparation was carried out under the same conditions for all samples.

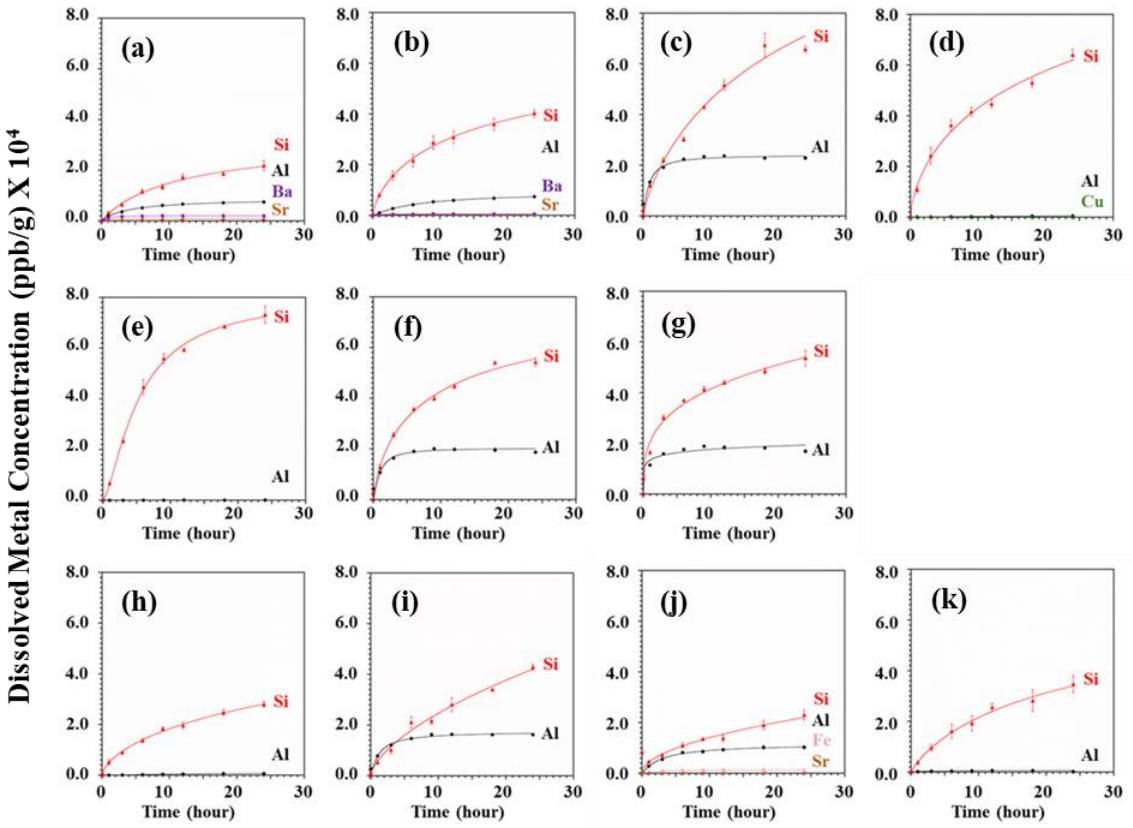

Figure 5. 4: Mass normalized dissolution of metals in GS from samples (a) Mine 1_Coal (b) Mine 1_Floor (c) Mine 1_Roof (d) Mine 1_RD (e) Mine 2_Coal (f) Mine 2_Floor (g) Mine 2_Roof (h) Mine 3_Coal (i) Mine 3_Floor (j) Mine 3_Roof (k) Mine 3_RD.

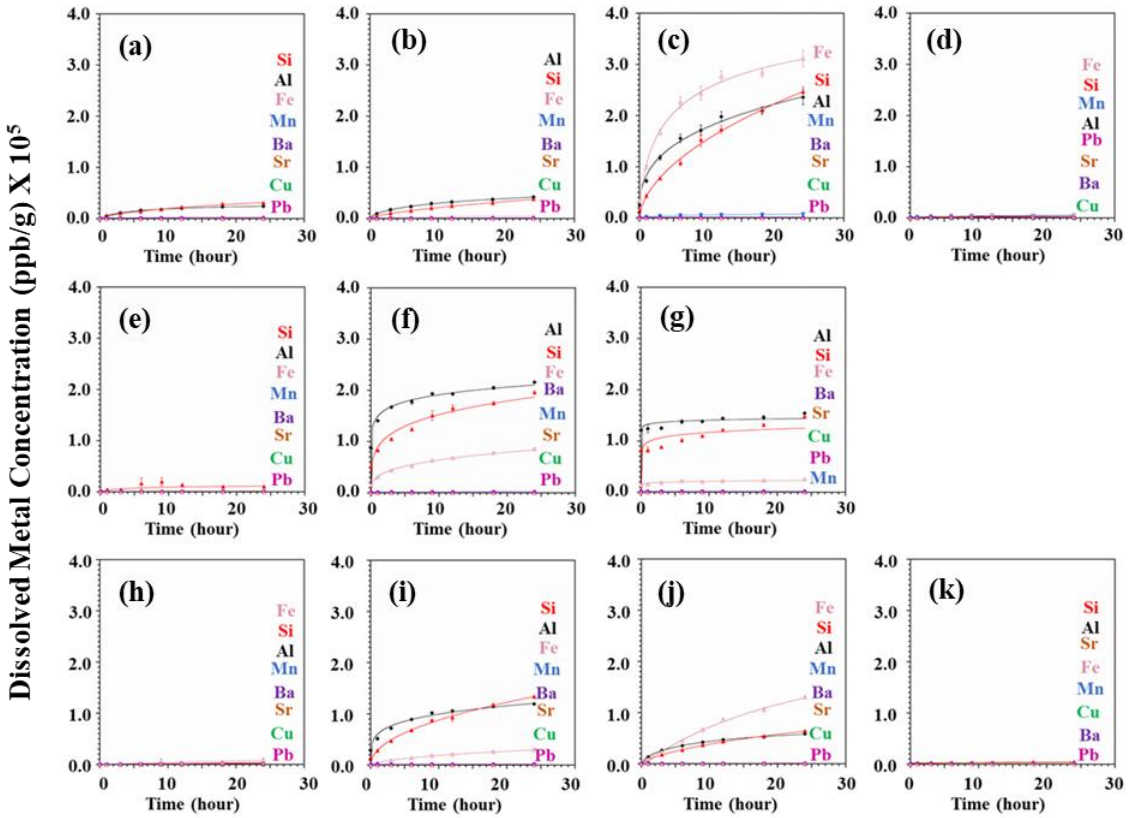

Figure 5. 5: Mass normalized dissolution of metals in ALF from samples (a) Mine 1_Coal (b) Mine 1_Floor (c) Mine 1_Roof (d) Mine 1_RD (e) Mine 2_Coal (f) Mine 2_Floor (g) Mine 2_Roof (h) Mine 3_Coal (i) Mine 3_Floor (j) Mine 3_Roof (k) Mine 3_RD.

Table 5. 7: Mass normalized dissolved metals in GS and ALF following 24 hours of dissolution experiments (1st half of the list).

	AL (ppb/g)		Si (ppb/g)		Mn (ppb/g)		Fe (ppb/g)	
Samples	ALF	GS	ALF	GS	ALF	GS	ALF	GS
Mine 1_Coal	24157	7491	30628	21867	19	-	2995	-
Mine 1_Floor	42106	7395	38263	40324	46	-	4630	-
Mine 1_RD	3199	554	4691	64097	4349	-	6260	-
Mine 1_Roof	236210	22903	246474	65779	7381	-	311387	-
Mine 2_Coal	261	129	10007	73247	26	-	2181	-
Mine 2_Floor	216190	18717	195795	54311	671	-	85658	-
Mine 2_Roof	154646	16914	147532	53600	96	-	24964	-
Mine 3_Coal	1229	671	3213	27958	25	-	9168	-
Mine 3_Floor	119462	16223	133812	42885	101	-	29332	-
Mine 3_RD	3281	236	4769	34697	570	-	2746	-
Mine 3_Roof	58544	10277	64096	23090	367	-	129782	1226

Table 5. 8: Mass normalized dissolved metals in GS and ALF following 24 hours of dissolution experiments (2nd half of the list).

	Cu (ppb/g)		Sr (ppb/g)		Ba (ppb/g)		Pb (ppb/g)	
Samples	ALF	GS	ALF	GS	ALF	GS	ALF	GS
Mine 1_Coal	50	-	730	980	2090	2055	269	-
Mine 1_Floor	168	-	540	393	1399	561	32	-
Mine 1_RD	168	126	1289	-	325	-	1465	-
Mine 1_Roof	176	-	879	-	2070	-	117	-
Mine 2_Coal	699	-	315	-	272	-	447	-
Mine 2_Floor	146	-	299	-	2157	-	130	-
Mine 2_Roof	286	-	538	-	2308	-	108	-
Mine 3_Coal	784	-	210	-	154	-	2603	-
Mine 3_Floor	364	-	790	-	2172	-	310	-
Mine 3_RD	148	-	3106	-	33	-	31	-
Mine 3_Roof	97	-	220	156	982	-	1049	-

All dissolution extents were normalized to the sample-specific surface area to reduce particle size and surface area impact. The GS and ALF surface area normalized

dissolved metal concentrations are illustrated in **Figures 5.6** and **5.7**, respectively. After surface area normalization, the data reveal that the dissolution extents still vary significantly between samples even when they are in the same dissolving media (**Table 5.9** and **Table 5.10**). The mineralogy, composition, and accessible elemental concentrations in the particular sample may play a role in producing these variations. Therefore, in the following step, we normalized our dissolution extents to the percentage elemental content within the sample.

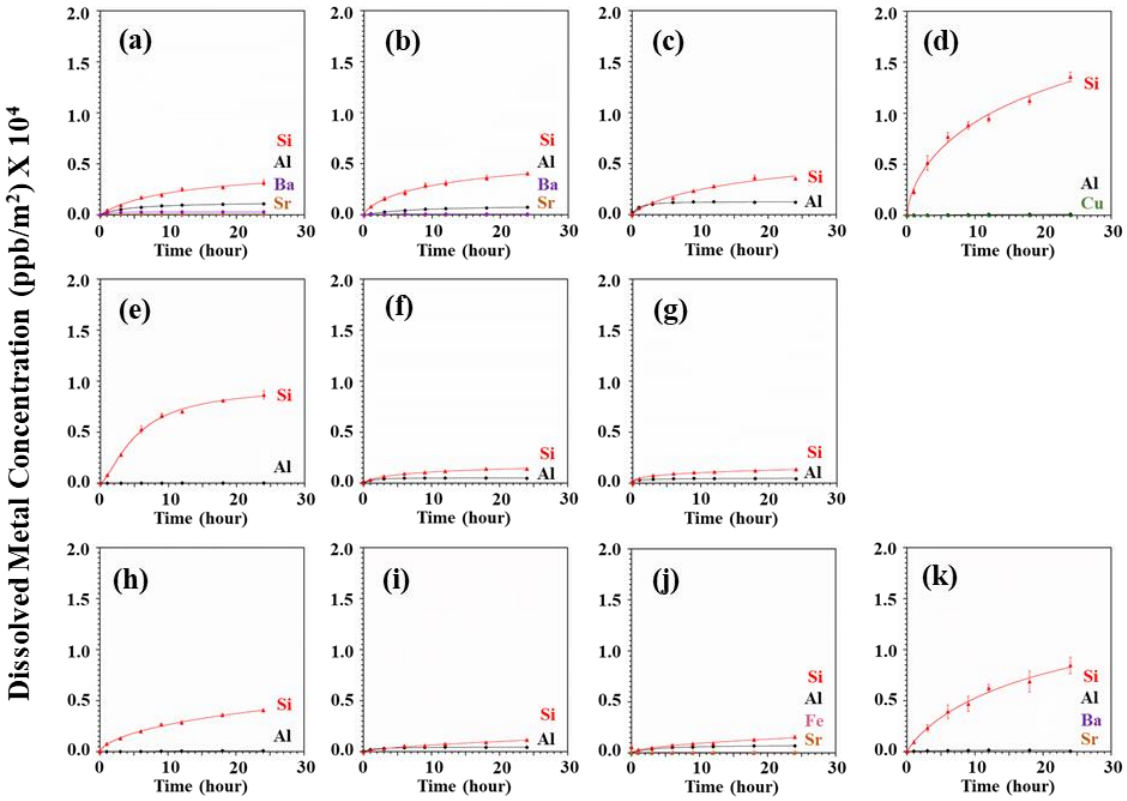

Figure 5. 6: Surface area normalized dissolution of metals in GS from samples (a) Mine 1_Coal (b) Mine 1_Floor (c) Mine 1_Roof (d) Mine 1_RD (e) Mine 2_Coal (f) Mine 2_Floor (g) Mine 2_Roof (h) Mine 3_Coal (i) Mine 3_Floor (j) Mine 3_Roof (k) Mine 3_RD.

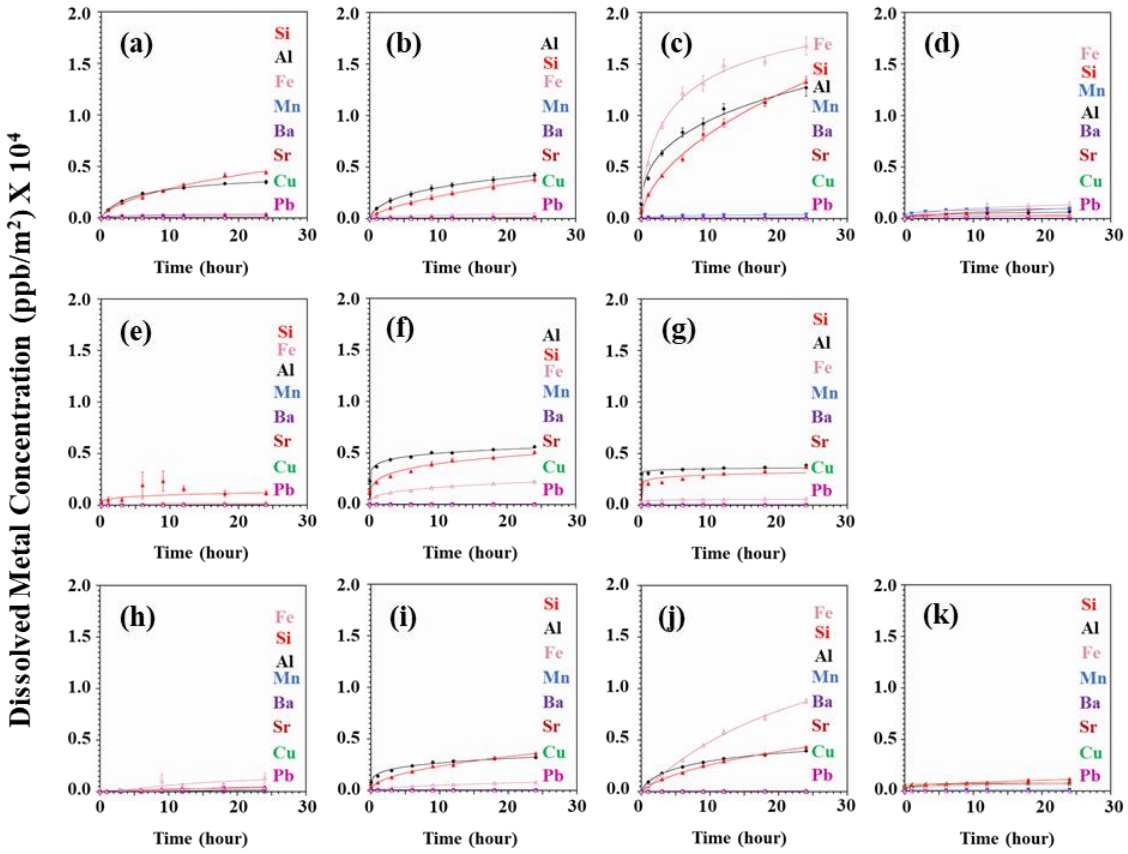

Figure 5. 7: Surface area normalized dissolution of metals in ALF from samples (a) Mine 1_Coal (b) Mine 1_Floor (c) Mine 1_Roof (d) Mine 1_RD (e) Mine 2_Coal (f) Mine 2_Floor (g) Mine 2_Roof (h) Mine 3_Coal (i) Mine 3_Floor (j) Mine 3_Roof (k) Mine 3_RD.

Table 5. 9: Surface area normalized dissolved metals in GS and ALF following 24 hours dissolution experiments (1st half of the list).

	AL (ppb/m2)		Si (ppb/m2)		Mn (ppb/m2)		Fe (ppb/m2)	
Samples	ALF	GS	ALF	GS	ALF	GS	ALF	GS
Mine 1_Coal	3496	1084	4432	3165	3	-	433	-
Mine 1_Floor	4206	739	3822	4028	5	-	463	-
Mine 1_RD	678	117	994	13580	921	-	1326	-
Mine 1_Roof	12706	1232	13258	3538	397		16750	
Mine 2_Coal	31	15	1183	8658	3	-	258	-
Mine 2_Floor	5621	487	5091	1412	17	-	2227	-
Mine 2_Roof	3881	424	3702	1345	2	-	626	-
Mine 3_Coal	178	97	466	4058	4	-	1331	-
Mine 3_Floor	3207	436	3592	1151	3	-	787	-
Mine 3_RD	800	58	1163	8463	139	-	670	-
Mine 3_Roof	3966	696	4343	1564	25	-	8793	83

Table 5. 10: Surface area normalized dissolved metals in GS and ALF following 24 hours dissolution experiments (2nd half of the list).

	Cu (ppb/m2)		Sr (ppb/m2)		Ba (ppb/m2)		Pb (ppb/m2)	
Samples	ALF	GS	ALF	GS	ALF	GS	ALF	GS
Mine 1_Coal	7	-	106	142	302	297	39	-
Mine 1_Floor	17	-	54	39	140	56	3	-
Mine 1_RD	36	27	273	-	69	-	310	-
Mine 1_Roof	9		47		111		6	
Mine 2_Coal	83	-	37	-	32	-	53	-
Mine 2_Floor	4	-	8	-	56	-	3	-
Mine 2_Roof	7	-	13	-	58	-	3	-
Mine 3_Coal	114	-	30	-	22	-	378	-
Mine 3_Floor	10	-	21	-	58	-	8	-
Mine 3_RD	36	-	758	-	8	-	8	-
Mine 3_Roof	7	-	15	11	67	-	71	-

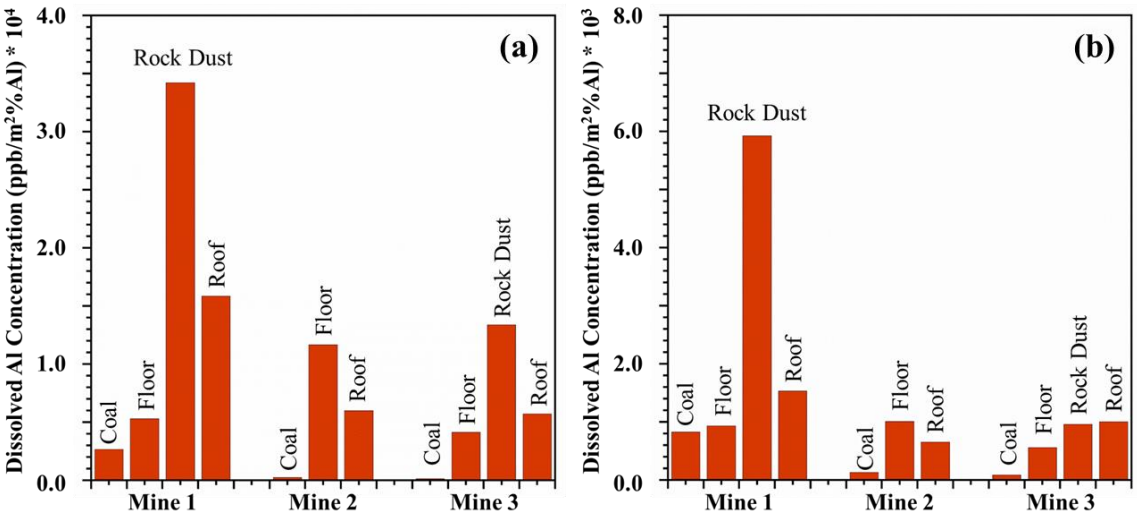

Figure 5. 8: % Al normalized dissolved Al in (a) ALF and (b) GS from all three mines.

Al dissolution in both ALF and GS, normalized to %Al, is shown in **Figure 5.8**. The figure summarizes the dissolved metal concentrations for all the samples following a 24-hour experiment on metal dissolution. The Al concentration in ALF, **Figure 5.8 (a)**, reveals that the dissolution extents of all the samples vary significantly between the samples from the same mine. The extent of Al dissolution varies as follows: For mines 1 and 3: rock dust > roof > floor > coal dust. The order for Mine 2 is floor > roof > coal. In GS, dissolution extent occurs in the same order as shown in **Figure 5.8 (b)**. It is also crucial to remember that after all the normalization, identical samples from three distinct mines leached out varying amounts of aluminum in both ALF and GS media. Variable Al dissolving extent followed by complete normalization may be connected to the sample's unique physicochemical characteristics, which will be described further in this section.

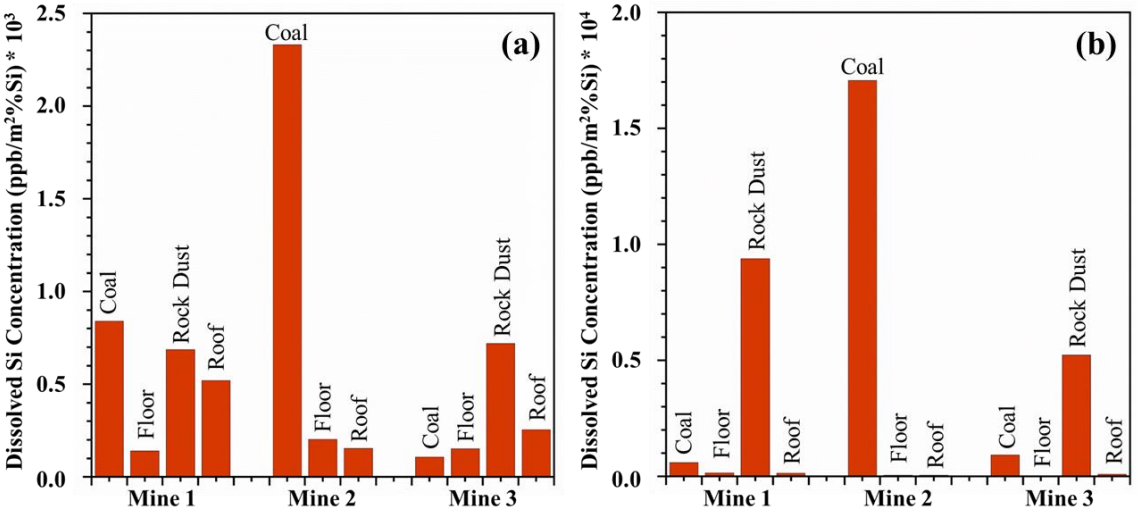

Figure 5. 9: % Si normalized dissolved Si in (a) ALF and (b) GS from all three mines.

Figure 5.9 represents the %Si normalized dissolved Si concentration at the end of the dissolution experiment in ALF and in GS**.** It is evident that all the dust from the same mine has visible differences in Si leaching and that dust from similar sources from three different mines varies in Si leaching following all the normalization. However, as previously mentioned, having higher dissolution in GS, Si leaching capability comparison between samples would be more accurate for the dissolution in GS. The order of the leaching of Si in the GS is as follows: rock dust > coal > roof > floor. Floor and roof dust have very little disintegration.

Iron is another metal that displayed some degree of disintegration in ALF. Since there was no appreciable dissolution of Fe in GS, Fe dissolution is normalized only for the dissolution in ALF and illustrated in **Figure 5.10**. Our results highlight that even after all the normalization and Fe dissolving, samples from the same mine and different mines still exhibit significant variances. Additionally, according to elemental analysis, no element normalization was done for other metals because they typically had very little elemental dissolution and low total elemental concentrations.

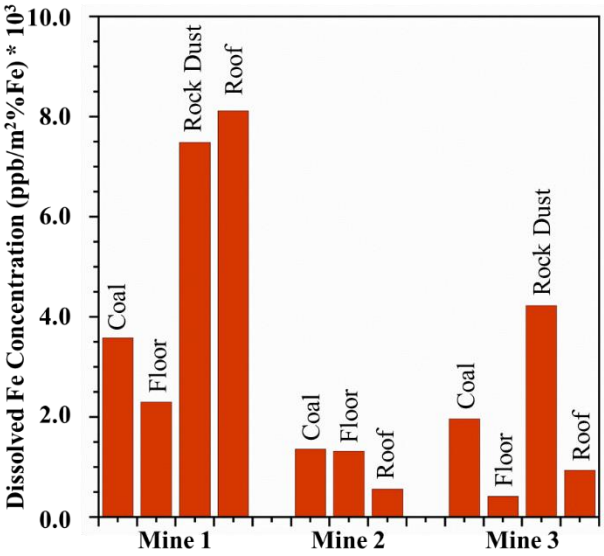

Figure 5. 10: % Fe normalized dissolved Fe in ALF from all three mines.

In summary, the dissolution experiment revealed that Si, Al, and Fe were the primary components that dissolved from the dust samples when they came into contact with the SLFs. The samples from the same mine from various sources, such as coal seams, rock dust, floor dust, and roof dust, show noticeable differences in the leaching of metals. The amount of dissolved metals in the same bodily fluid varies when similar sample types are taken from different mines. These variations in dissolution, followed by the entire process of normalization, may be connected to the mineralogy of the sample and its actual composition. The XRD data, given in **Table 5.3**, indicate considerable differences in the mineral components of the samples taken from the same mine. Even the dust that was gathered from comparable sources in three different mines contains a variety of minerals. While the coal dust from Mine 1 only contains quartz and kaolinite, the coal dust from Mine 2 also includes pyrites and calcite, and the coal dust from Mine 3 also includes

muscovite, calcite, and dolomite. Additionally, it was found that the rock dust from Mine 1 contained quartz, chlorite, calcite, and dolomite, whereas mine 3 had just quartz and calcite. Similar to this, no other sample, whether from the same mine or another, has the same mineral phases. The composition of minerals also varies, as revealed by the XRD spectra, and no two samples have the same composition. As one of the main contributing factors to metal leaching, mineralogy and composition have been identified previously.[2] While the sources from which dust is produced and its surroundings largely determine its mineralogy and composition, it is crucial to consider source-specific physicochemical features when evaluating dust-related toxicity rather than generalizing it.

5.4.3 Results from the In-vitro Study

Cell viability test was performed using MTT assay. **Figure 5.11** shows the data for 11 samples studied under the current investigation. The lung epithelial cells were exposed to three different doses of dust, and all the coal dust samples showed at least some decreased viability with increased concentration. This effect was more prominent for roof and floor dust samples than coal and rock dust which is in agreement with the results from the dissolution experiment where dust from the floor and roof showed higher leaching capability on a mass basis. This implies if an individual is exposed to coal dust generated from the coal seam, floor, roof, and rock dust, the dust coming from the floor and roof will potentially cause higher toxicity.

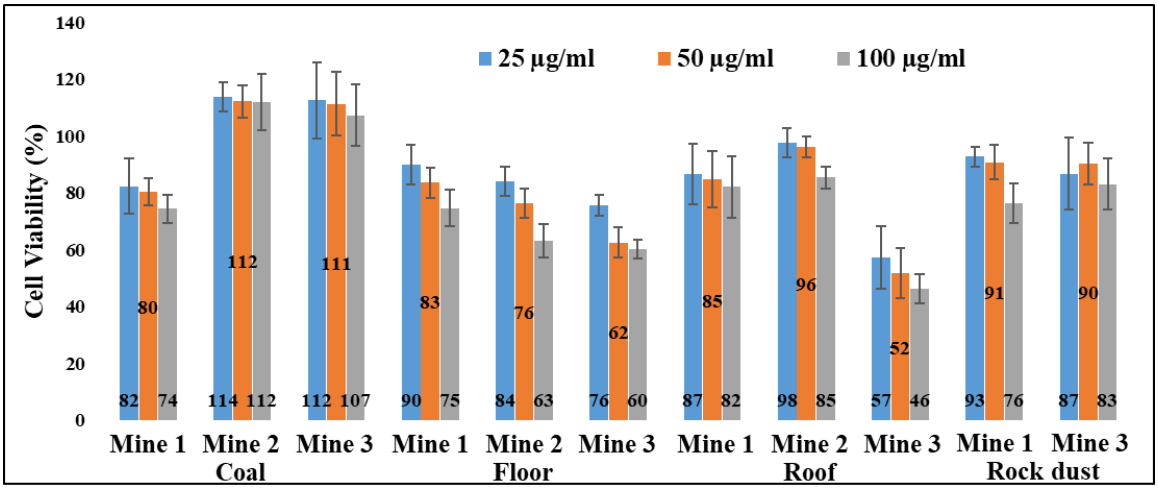

Figure 5. 11: Cell viability data for the 11 dust samples from various sources of three different mines.

5.5 Conclusions

The features and toxicity of RCMD are evaluated in the current study in connection to their unique intra- and inter-mine sources based on their metal leaching capabilities in SLFs. This work examined coal dust samples from the coal seam, the mine's floor and roof, and rock dust samples from the same mine. Additionally, we assessed coal dust taken from three separate mines situated in various geographic regions. Our research suggests that the physicochemical characteristics such as specific surface area, available elemental content, mineralogy and site specific compositions of RCMD substantially impact the metal

leaching in lung fluids and the overall toxicity of the results. It was discovered that the dust produced by the mine's floor and the roof had a higher specific surface area than the dust produced by the coal seam and the rock dust. On a mass basis, the greater surface area of the floor and roof dust resulted in more significant metal leaching and increased toxicity. The cell viability assays also reveal that dust from the floor and roof can be more toxic. Our findings also imply that the mineralogy and composition of the samples are essential factors in determining their toxicity. The composition and mineralogy of RCMD are highly sample-specific and primarily derived from the distinctive sources from which they were created. Hence the toxicity of RCMD will depend on the source. Therefore, our findings suggest that metal leaching from RCMD is an inescapable occurrence regardless of its source. However, the extent of metal leaching is greatly influenced by the sources from which they are produced.

5.6 Acknowledgement

The authors thank Virgil Lueth, Bonnie Frey, and Kelsey McNamara at the New Mexico Bureau of Geology for providing the facility to perform XRD and total microwave digestion experiments. The material presented in this chapter remain unpublished and author holds the copyright.

CHAPTER 6

ATMOSPHERIC PROCESSING AND BIOAVAILABLE IRON PRODUCTION FROM COAL FLY ASH: EFFECT OF TiO_2 IN IRON LEACHING

6.1 Abstract

Iron (Fe) has been recognized as one of the limiting nutrients for aquatic life. The principal source of accessible iron for the seas is atmospheric iron-containing mineral dust. In the current study, we looked into coal fly ash (CFA) as a source of bioavailable iron. We used spectroscopic techniques coupled with the dissolution experiments in both low- and high-flux conditions. We conducted the nitric acid dissolution studies in atmospherically relevant conditions. We have also investigated the impact of the external mixing of titanium dioxide (TiO_2), rutile and anatase, on CFA's capacity to leach iron. Both industrial and natural dust samples include TiO_2, particularly at the nanoscale. Further, we assessed the CFA's atmospheric processing in terms of particle size, mineralogy, and composition. Our findings show that titanium, whether it be titanium added externally or titanium present in the sample itself, increases the iron mobility from the CFA. As a result, this research will give us vital, as yet undiscovered, information about CFA as a source of bioavailable iron.

6.2 Introduction

Iron is one of the main micronutrients that restricts the worldwide ocean's primary productivity in the high nutrient low chlorophyll (HNLC) zone.[220] Despite being the fourth-most common metal in the earth's crust, direct iron dissolution from the crust is only possible up to a concentration of 0.1 nM because seawaters have a basic pH (pH 8.3). Despite this restriction, the oceanic iron content can reach up to 2 nM.[221] Numerous studies have linked the Fe-containing atmospheric aerosols to this higher dissolved iron content. During their stay in the atmosphere, Fe containing aerosols are processed by moisture and other gases to create deliquescence layer. Further, the pH of deliquescence layer can drop to as low as 1 as a result of atmospheric processing, which causes more Fe to leach out when added to ocean waters. Most of the Fe that is transported in the atmosphere comes from lithogenic sources, accounting for around 95% of all the Fe that is present in suspended particles.[61] Therefore, most research to date has focused on the atmospheric processing of mineral dust containing Fe.[62-65] However, alternative Fe sources come from combustion sources, such as burning biomass, coal, and oil.[66, 67]

Although these sources only make up a small portion of the total Fe, their increased solubility can significantly impact primary production and help the biogeochemical cycle by inducing more CO_2 uptake.[5, 68-73]

In contrast to the overall Fe emission from mineral dust, which was estimated by Wang et al., (2015) to be 41.0 Tg yr^{-1}, the average Fe emission from combustion sources between 1960 and 2007 was 5.3 Tg yr^{-1} on average.[74] Additionally, according to their estimate, there is an 8.4 Tg yr^{-1} overall sink for Fe deposition across the world's oceans, with combustion sources accounting for 7% of that amount. The coal combustion process accounts for the majority of the Fe from the combustion sources. As a result, numerous research has looked into coal combustion products, or coal fly ash (CFA), as potential sources of bioavailable iron for the ocean in recent years.[5, 7, 75]

Additionally, while CFA contributes relatively little bioavailable Fe globally, it is predicted to account for 50% of the Fe deposits in the water surrounding industrialized regions.[88] Additionally, because CFA particles are in a fine mode (<1 μm) in the atmosphere, they can travel a considerable distance before being deposited in the ocean.[89] While being transported over such a long distance, CFA particles may be processed by acidic gases such as HNO_3, H_2SO_4, HCl, etc.[222-224] The inherent characteristics of the Fe-containing particle, such as size, shape, specific surface area, iron speciation, and Fe distribution within the particle, are strongly correlated with Fe solubility under atmospheric processing.[63, 76-81] Additionally, a study revealed that the presence of metal oxides other than those containing iron, such as Al_2O_3, CaO, TiO_2, and others, affects the leaching of iron during atmospheric processing.[82] Additionally, it has been claimed that the presence of Ti in the sample or the addition of TiO_2 from the outside promotes the dissolution of Fe from mineral dust that contains Fe.[83, 84] While the sources show that CFA particles have a significant likelihood of mixing with TiO_2 (the most prevalent industrial dust) during their time in the environment, the elemental composition also points to a sizable Ti content in the CFA particles.[85-87] Although we predicted that the Fe leaching from CFA would increase in the presence of TiO_2, following the same pattern as mineral dust, it has not yet been verified. Therefore, in the present study, we assessed coal fly ash as a potential source of bioavailable Fe in the presence of TiO_2.

In this study, laboratory tests were carried out to ascertain the Fe leaching for four standard reference materials for coal fly ash under simulated atmospheric processing. We specifically looked into Fe leaching and speciation in the presence of TiO_2 under conditions that were relevant to the atmosphere. According to the experimental findings, externally added TiO_2 or Ti content within the sample produced increased bioavailable Fe for all of the coal fly ash samples.

6.3 Methods and Materials

6.3.1 Standards and Chemicals

The National Institute of Standards and Technology's (NIST's) standard reference materials for coal fly ash were acquired from the USGS and used as received. The following common reference sources were employed: SRM 1633b, SRM 2689, SRM 2690,

and SRM 2691. To make it easier to understand, coal fly ash will be referred to as sample names CFA 1, CFA 2, CFA 3, and CFA 4.

For this study, reagent-grade or greater compounds were employed. The Mili-Q water (18.2 M, Mili-Q-A10) was used to prepare all the media. In the batch reactors, two different titanium dioxide mineralogical phases rutile and anatase were combined with coal fly ash samples. Hydrochloric acid (HCl, VWR International - BDH, 36.5 - 38.0%), Hydroxylamine hydrochloride ($HONH_2$.HCl, Acros Organic, >99%), Ammonium fluoride (NH_4F, J.T. Baker Chemicals, 99%), 1,10-phenanthroline ($C_{12}H_8N_2$, Acros Organic >99%), Ammonium acetate (CH_3COONH_4, VWR International, ultra-pure), and Acetic acid (CH_3COOH, VWR International, glacial) were the chemicals utilized in the 1,10-phenanthroline process. A quantitative calibration plot for the Fe determination was done using ferrous ammonium sulfate hexahydrate ($Fe(NH_4)_2(SO_4)_2 \cdot 6H_2O$, Fischer Scientific, 98.5%) following the same procedure developed previously.[96]

6.3.2 Characterization of the Coal Fly Ash

SEM images were collected using a NOVA-Nano-SEM-450 at the center for integrated nanotechnology (CINT), to determine the particle size and shape of the coal fly ash samples. Using the ImageJ software, ~500 particles per sample were measured to generate the size distribution. X-ray diffraction spectra obtained with a Cu Kα source were used to analyze the mineral components of the coal fly ash samples. Following a 16-hour outgassing at 150° C, the samples' specific surface area was calculated using the BET N_2 adsorption isotherm. A Nicolet iS50 series FTIR was used to gather the FTIR spectra, which were used to determine surface functional groups. A small (2 mL) centrifuge tube was utilized for sample preparation. About 20 mg of the material was sonicated in 1 mL of water for 20 minutes before being pipette-transferred to the Ge ATR crystal. After an overnight air-drying process, the sample remained visible on the ATR crystal in a thin layer. The collected spectra were compared to the bare crystal and reported.

6.3.3 Dissolution of Iron in the Acid Media from the Coal Fly Ash

Dissolution tests were performed in acidic solutions as described in earlier research to simulate the atmospheric processing and chemistry of coal fly ash's deliquescence layer.[83, 225] Inside a dark room, dissolution experiments were carried out using a specially built glass reactors that is made to have a capacity of 100 mL and equipped with an airtight top. With a sample loading of 20 mg (coal fly ash or coal fly ash with TiO_2) per 100 mL of medium, we employed a dissolution media of HNO_3 at pH 2. In the case of coal fly ash with TiO_2, sample loading was 13.3 mg of coal fly ash and 6.7 mg of TiO_2. To create a reducing environment, the acid medium was purged with nitrogen gas at 5 sccm for 5 minutes before the sample was added. A magnetic stirrer was used to agitate the reaction mixture continuously, and a heated water jacket was used to keep the temperature at 25 °C. Using disposable syringes attached to 12 cm Teflon tubes, a 1.5 mL sample aliquot was taken periodically during the reaction. The 1,10-phenanthroline approach was used to immediately determine the dissolved iron concentration for both Fe^{2+} and total Fe in the obtained sample.[96] Both dark and light conditions were used for each dissolving experiment. A solar simulator (150 W xenon lamp, New Port Corp.) was fitted with a 1.5

air mass filter for the light reaction. The average result with the standard error was presented after each dark, and the light response was carried out individually in triplicate.

6.4 Results & Discussion

6.4.1 Particle Characterization

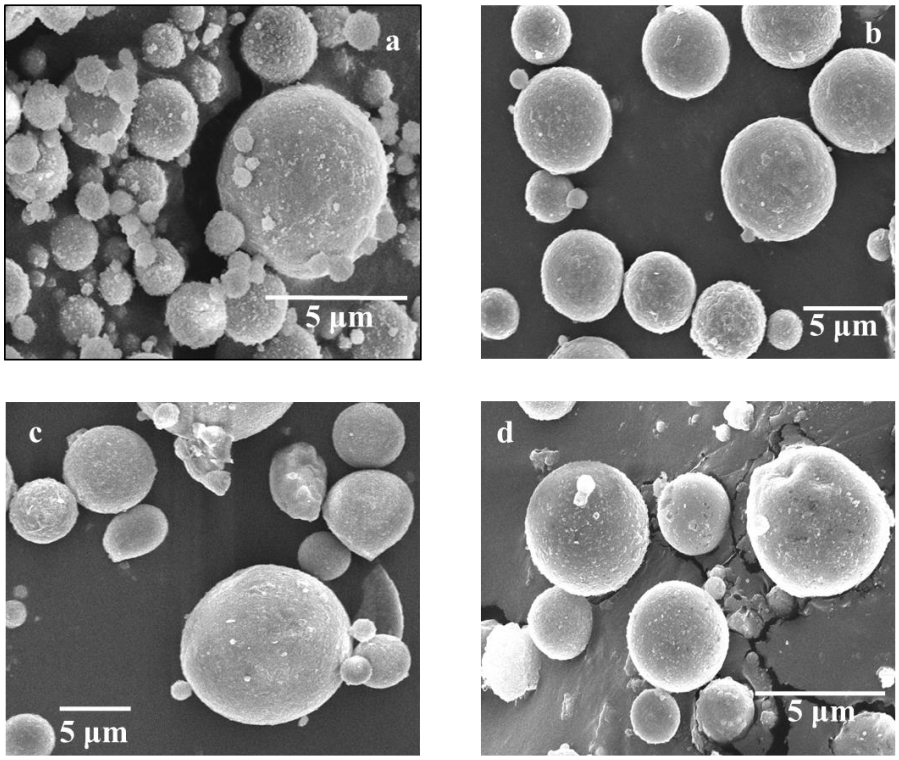

Figure 6. 1: Representative SEM images of the coal fly ash (a) CFA 1, (b) CFA 2, (c) CFA 3, and (d) CFA 4.

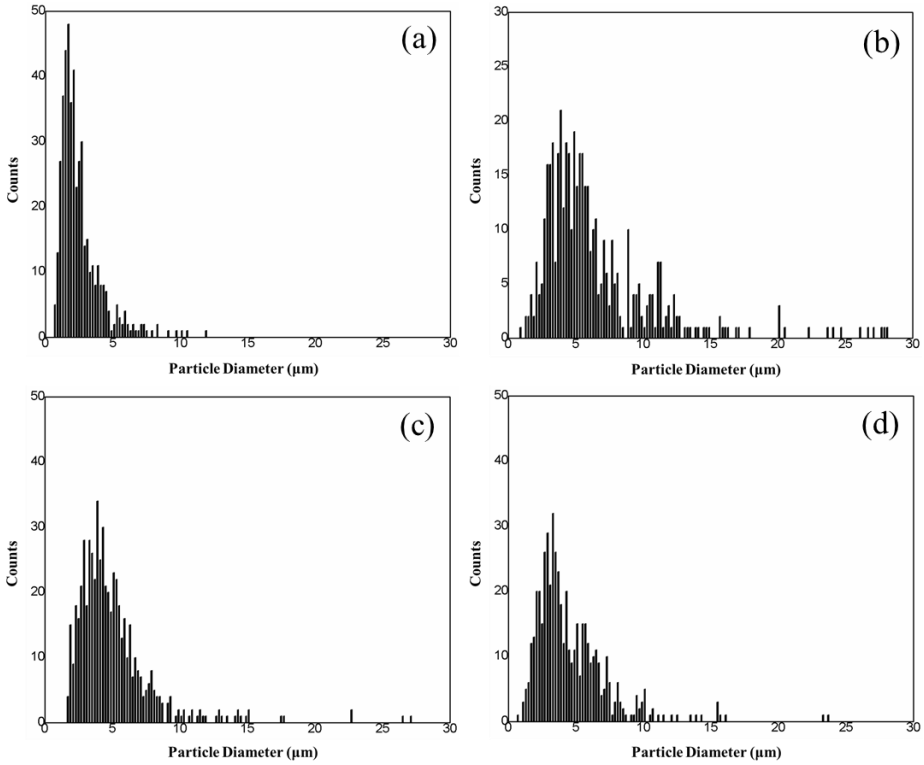

Figure 6. 2: Histograms generated using SEM images of coal fly ash (a) CFA 1, (b) CFA 2, (c) CFA 3, and (d) CFA 4.

Table 6. 1: Particle size distribution calculated from histograms.

Samples	Average Particle Size (µm)	BET Surface Area (m2/g)
CFA 1	2.57 ± 1.59	2.09 ± 0.29
CFA 2	6.88 ± 5.73	0.55 ± 0.02
CFA 3	5.07 ± 2.95	1.95 ± 0.08
CFA 4	4.68 ± 3.04	1.59 ± 0.13

The SEM images were used to calculate the typical particle sizes. Using the software ImageJ, 500 particles on average were counted for each sample. **Figure 6.1** presents the SEM images obtained for the coal fly ash samples and demonstrates that most fly ash particles are spherical and range in size from submicron to a few microns. Histograms are shown in **Figure 6.2**. **Table 6.1** reports the fly ash sample's average particle sizes and specific surface areas. The CFA 1 sample has the largest specific surface area of 2.09 ± 0.29 m^2/g while having the smallest average particle size of 2.57 ± 1.59 µm. The CFA 2 sample, on the other hand, had the lowest specific surface area of 0.55 ± 0.02 m^2/g

and the largest average particle size of 6.88 ± 5.73 μm. While the values for both characteristics for CFA 3 and CFA 4 are inside the above range.

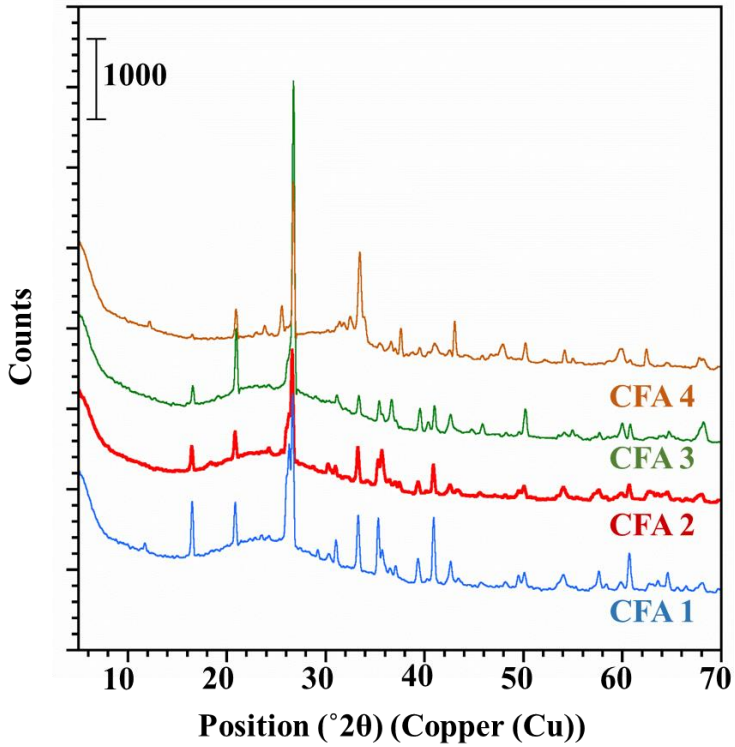

Figure 6. 3: XRD spectra for the coal fly ash samples.

Table 6. 2: Major minerals in the coal fly ash samples.

Sample	CFA 1	CFA 2	CFA 3	CFA 4
Quartz	√	√	√	√
Mulite	√	√	√	
Lime				√
Magnesioferrite	√	√		
Anhydrite				√
Periclase				√
Akermanite				√
Gehlenite				√

According to the XRD results in **Figures 6.3** and **Table 6.2**, the predominant component of all the fly ash samples, except for CFA 4, was mullite ($Al_6Si_2O_{13}$), an aluminosilicate derived from coal's clay components. Additionally, diffraction peaks exist in all the samples demonstrating the presence of quartz (SiO_2). Two of the samples, CFA

1 and CFA 2, were identified to have the magnesium iron oxide mineral magnesioferrite ($Mg(Fe^{3+})_2O_4$), a member of the magnetite class.[226] Lime (CaO), anhydrite ($CaSO_4$), periclase (MgO), akermanite ($Ca_2Mg[Si_2O_7]$), and gehlenite ($Ca_2Al[AlSiO_7]$) were also visible in the X-ray diffractogram of CFA 4. Additionally, XRD spectra of the coal fly ashes exhibited a broadening pattern between 15˚ and 35˚, which was an indication of amorphous phase of silica.[141] Additionally, fly ash sample FTIR spectra were obtained and displayed in **Figure 6.4**. Minor peaks were present in the processed spectra for the hydroxyl stretching and bending modes at 3394 cm^{-1} and 1621 cm^{-1}, respectively. These peaks confirmed that fly ash samples contain a small amount of moisture. A doublet for all the samples at 795 and 777 cm^{-1} were indication of the presence of Si-O-Si bridging, which was one of the quartz's distinctive peaks. The most noticeable peak appeared as a broad band at 1057 cm^{-1}, 1096 cm^{-1}, and 1060 cm^{-1} for samples CFA 1, CFA 2, and CFA 3, respectively. These values are likely related to the Si-O-Si, Si-O-C, or Si-O-Al asymmetric stretching for silicates and aluminosilicates. The most prominent peak for CFA 4 was at 1124 cm^{-1}, indicative of the anhydrite crystals' S=O stretching.[143, 227] However, the IR spectra did not show any phonon modes of other metal oxide minerals.

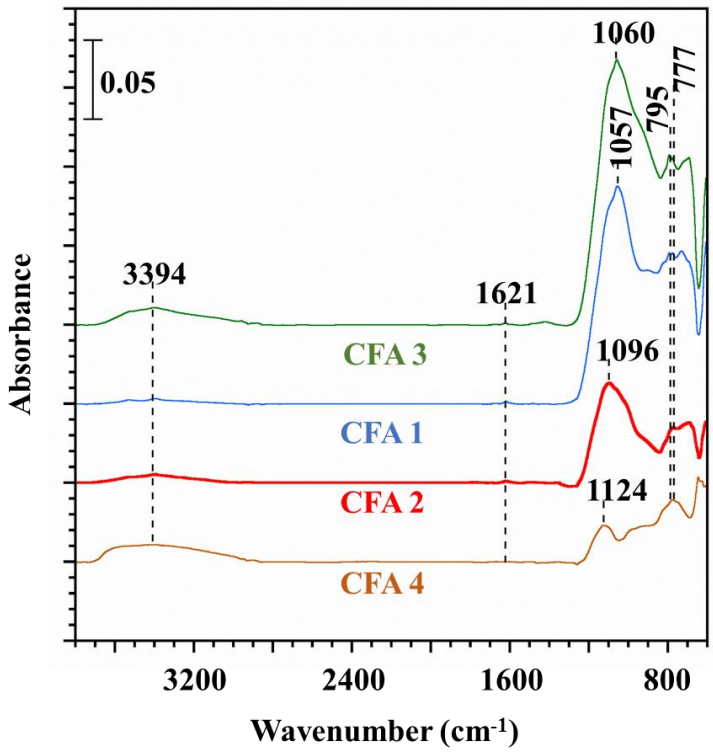

Figure 6. 4: FTIR spectra for coal fly ash samples.

6.4.2 Iron Dissolution from Batch Reactor Studies

The initial investigation into the iron leaching for the coal fly ash samples was carried out in a reduced environment in the absence of solar radiation. **Figure 6.5** compares the mass normalized dissolved total Fe and the Fe(II) from four fly ash samples to an iron oxide proxy, α-Fe_2O_3 (Hematite). Our results highlight that, except for CFA 3, all CFAs dissolve total Fe greater than hematite, while all of them produce less Fe(II) than hematite.

It is also apparent that, on a mass basis, the fly ashes produced vastly different amounts of dissolved total Fe and Fe(II) in the same acid solution. Total Fe dissolves in the following order: CFA 2 > CFA 4 > CFA 1 > CFA 3, whereas Fe(II) dissolves in the following order: CFA 1 > CFA 2 > CFA 3 > CFA 4. These variations in iron leaching within the same medium can be caused by a variety of factors, including particle size, the surface area exposed to the dissolution media, the amount of accessible iron in samples, mineralogy, and composition. We normalized the dissolved iron concentrations to the surface area of the particular samples to remove the impact of particle size and surface area. **Figure 6.6** shows the surface area normalized data and that all CFAs had higher dissolving efficiencies for total Fe and Fe(II) than hematite. The hematite utilized in this work has a specific surface area of 100 m^2/g, which is likely what causes its high mass-based dissolution.

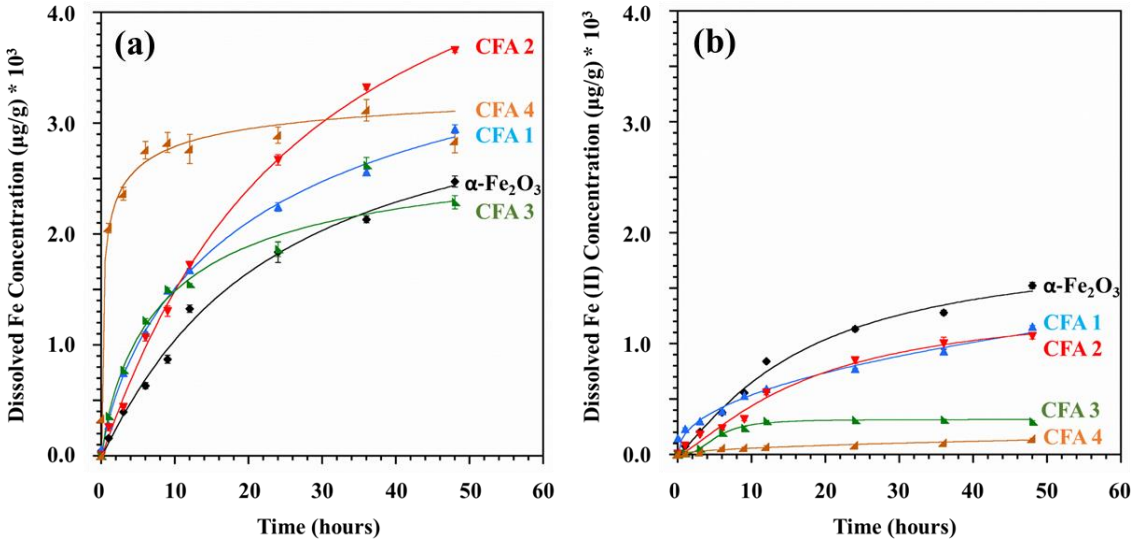

Figure 6. 5: Mass normalized dissolution of (a) Total Fe and (b) Fe (II) from all the fly ash samples including α-Fe_2O_3 in HNO_3 at pH 2.

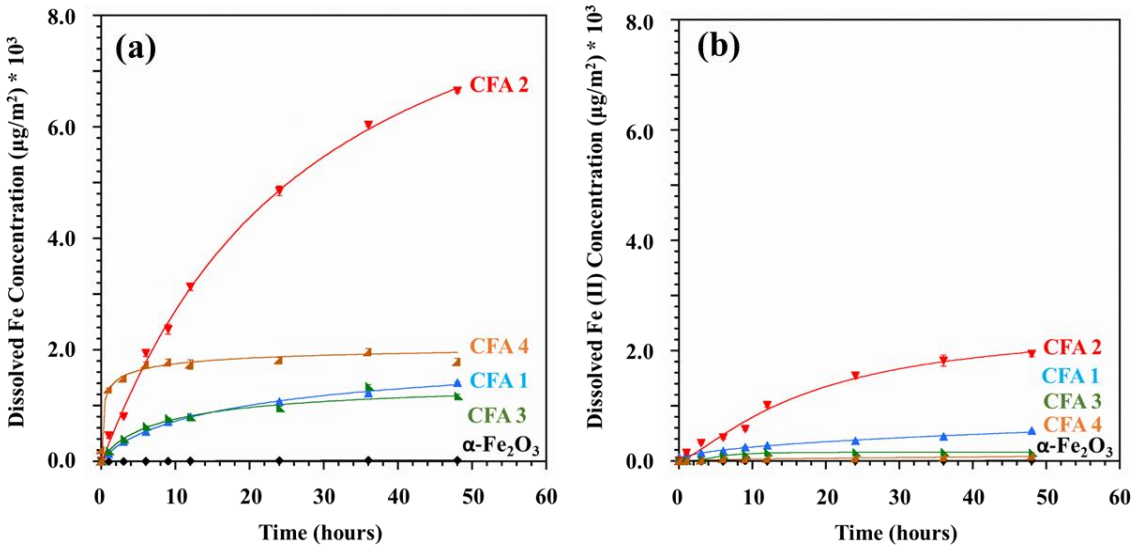

Figure 6. 6: Surface area normalized dissolution of (a) Total Fe and (b) Fe (II) from fly ash samples, in comparison with α-Fe_2O_3 in HNO_3 at pH 2.

The normalization to the respective surface area had little or no effect on the dissolution trends. As a result, the dissolution extents were further normalized to the total %Fe in the respective sample (**Figure 6.7**). After these normalizations, there is still a sizable disparity in the degree of dissolution across the samples, which can be caused by differences in composition and mineralogy, as revealed by our characterization studies. Given that the mineralogy and chemical compositions of CFAs are obtained from the coal that was burned, the conditions of combustion, and the cooling process, the source of the CFA is important for Fe leaching.[5, 228, 229]

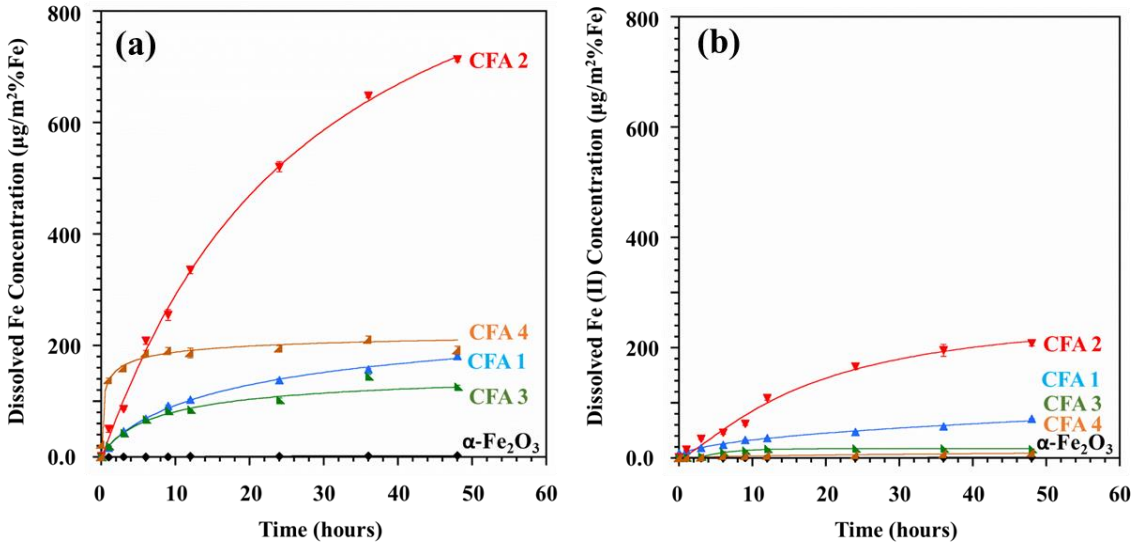

Figure 6. 7: Dissolved (a) Total Fe and (b) Fe (II) from fly ash samples normalized to respective surface area and %Fe present. The dissolution trends are compared against α-Fe_2O_3 in HNO_3 at pH 2.

The current work also focused on dissolved iron production during the daytime by carrying out batch reactor studies under simulated solar radiation. **Figure 6.8** compares the extent of iron dissolution between the presence and absence of solar flux. Our results clearly show that total Fe and Fe(II) leaching decreases for CFA 1 and CFA 2 in the presence of light while increasing for the samples CFA 3 and CFA 4. These trends suggest that there could be a series of reactions where iron dissolution is impacted by processes combining the effects of ligand- and H^+-promotion.[84] During these processes, we speculate that H^+ ions are consumed to form dissolved Fe species, while NO_3^- undergoes surface-mediated reduction to form Fe^{3+}, which can then be re-adsorbed to the surface of CFA particles, hence limiting the overall dissolution of Fe. As a result of these two mechanisms competing, Fe leaching occurs. The following describes the reaction mechanism.

Proton promoted Fe leaching:

$$Fe_2O_3(s) + 6H^+ \rightarrow 2Fe^{3+}(aq) + 3H_2O \quad \text{Eq. 6.1}$$

$$FeO\ (s) + 2H^+ \rightarrow\ Fe^{2+}(aq) + H_2O \quad \text{Eq. 6.2}$$

Surface mediated reduction of NO_3^- to NO_2^-:

$$2Fe^{2+} \rightarrow 2Fe^{3+} + 2e^- \quad \text{Eq. 6.3}$$

$$NO_3^- + 2H^+ + 2e^- \rightarrow NO_2^- + H_2O \quad \text{Eq. 6.4}$$

$$2Fe^{2+} + 2H^+ + NO_3^- \rightarrow 2Fe^{3+} + NO_2^- + H_2O \quad \text{Eq. 6.5}$$

Under solar irradiance, photolysis of the hydroxyl group on the surface of metal oxides can cause Fe(III) to be reduced to Fe(II), which then separates from the surface and releases more dissolved Fe (II).[64] Moreover, semiconductor metal oxides such as Fe_2O_3 and TiO_2 produce photo-induced conduction band electron (e_{cb}^-) which can reduce Fe(III) to Fe(II) while increasing the dissolution.[64, 230-232] However, this pathway is extremely unfavorable due to the significantly low levels of semiconductor metal oxide in CFA samples, as indicated by the certificate values of Ti (0.52 to 0.90%) and Fe (3.57 to 9.32%). Further, protons in the acidic media can consume the photo-induced conduction band electron (e_{cb}^-) producing H_2, raising the pH of the solution, and decreasing solubility. In addition, under solar radiation, NO_2^- undergoes photolytic decomposition, favoring the surface-mediated reduction and reducing the Fe leaching.

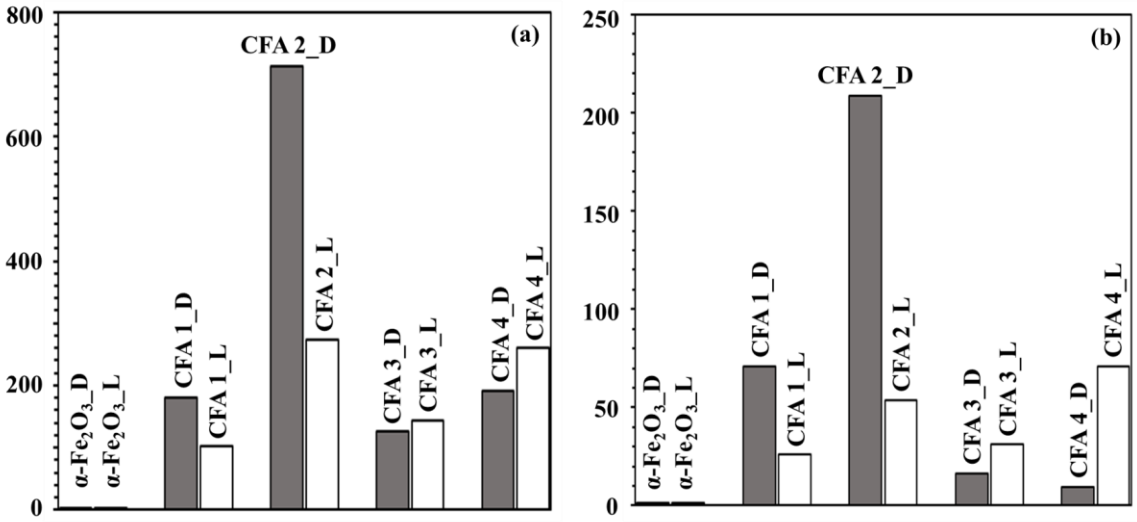

Figure 6. 8: A comparison of (a) total Fe and (b) Fe (II) dissolution for coal fly ash samples in the presence and absence of solar flux after 48 hours. The data presented here are normalized to the surface area and total % Fe of the respective sample.

As shown in **Figure 6.8**, our data do not reveal a generalized trend for iron leaching; instead, they are more sample-specific. Under light conditions, total Fe leaching from CFA 1 and CFA 2 dropped by 43% and 62%, respectively, whereas Fe(II) reduced by 63% and 74%. In contrast, the total Fe leaching from CFA 3 and CFA 4 increased by 14% and 36%, respectively, while Fe(II) increased by 91% and 640%. These shifts in iron dissolution could potentially be explained by the Ti:Fe ratios of the CFA samples. As evident from the data provided in **Table 6.3**, higher Ti:Fe ratio in the CFA samples promotes more Fe leaching to the media under light conditions. In our previous work, we have reported titanium oxide, either occurring within iron oxide minerals or artificially introduced, has a synergistic effect on the leaching of iron.[83, 84] Therefore, assessed the effect of added TiO_2 in iron leaching from the coal fly ash samples under both dark and light conditions.

Table 6. 3: Ti to Fe ratio and percent changes in the Fe leaching in the presence of solar light.

Samples	Ti/Fe ratio	Total Fe	Fe (II)
CFA 1	0.10	↓ 43 %	↓ 63 %
CFA 2	0.08	↓ 62 %	↓ 74 %
CFA 3	0.15	↑ 14 %	↑ 91 %
CFA 4	0.20	↑ 36 %	↑ 640%

Figure 6.9 reports the extent of Fe dissolution in fly ash samples mixed with TiO_2, anatase, or rutile after 48 hours of dissolution. The data presented for dark and light conditions are normalized to the surface area and total %Fe in the respective sample. Rutile

addition to the reaction medium increased total Fe dissolution under dark conditions for CFA 1 and CFA 4 by 1.2- and 1.3-folds, respectively. However, the dissolution was lowered for CFA 2 and CFA 3 by 0.9- fold. The addition of anatase in the dark decreased the dissolution of total Fe for CFA 1, CFA 2, and CFA 3 by 0.75, 0.37, and 0.59 times, respectively, whereas CFA 4 was the sole compound to increase the dissolution by 1.37 times. Rutile and anatase are both known to be efficient adsorbents of anions such as NO_3^- .[233, 234] As a result, surface complexation competes with externally added TiO_2, which could be partially responsible for the lower Fe dissolution. A greater surface area for the surface-mediated reduction discussed in the preceding section can also be provided by additional TiO_2, which will ultimately result in less Fe dissolving. On the other hand, TiO_2 is known to produce conduction band electrons even in total darkness, which can convert Fe(III) to Fe(II) and ultimately promote dissolution. Furthermore, both TiO_2 have surface defects of Ti(III) that, when exposed to a potent oxidizing agent like NO_3^-, can initiate a redox process that will lead to NO_2^-, which can then oxidize back to nitrate, reducing the Fe(III) to Fe(II) in the medium.[235] As a result, all of these potential processes might result in either an increase or a decrease in the total Fe leaching in the presence of TiO_2 under dark conditions.

Under irradiated conditions, the added rutile or anatase produced more dissolved Fe compared to that of the fly ash only sample. The addition of rutile raised the total dissolved Fe by 1.26, 2.20, 1.17, and 1.79 folds for the samples CFA 1, CFA 2, CFA 3, and CFA 4, respectively. The leaching of Fe increased by 1.20, 1.80, 1.35, and 1.71 times, respectively, in the presence of anatase. These are most likely caused by the fact that rutile and anatase both produce more photo-induced conduction band electrons when exposed to radiation than when not, which promotes a greater Fe dissolution.[233] Additionally, both TiO_2 under solar radiation cause Ti(III) surface defects to grow, which aids in the media's ability to reach out additional Fe.[235]

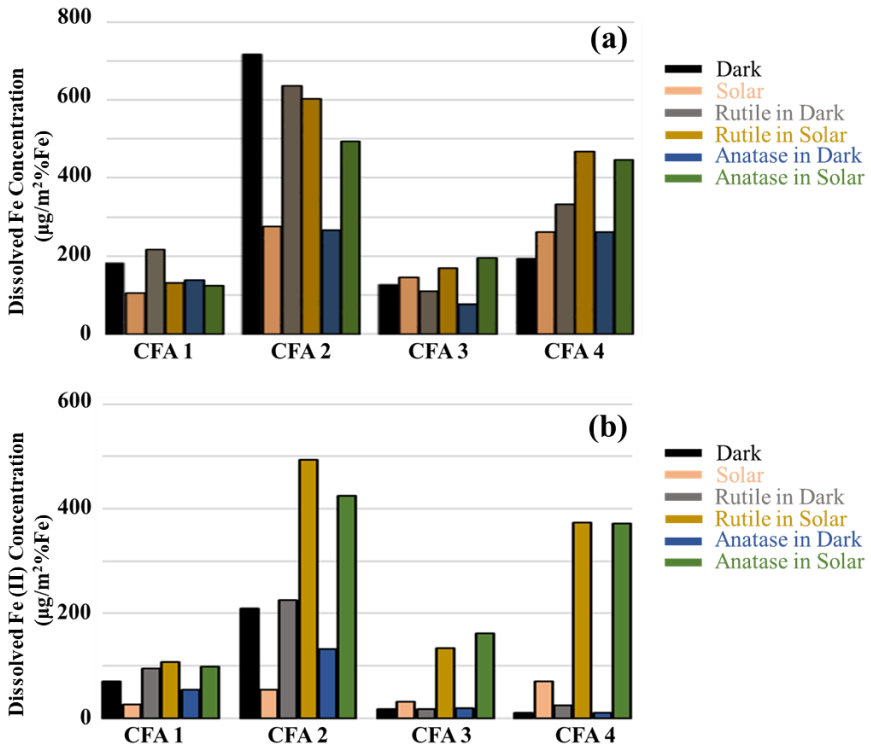

Figure 6. 9: Dissolved (a) total Fe and (b) Fe (II) in the presence of rutile and anatase after 48 hours of dissolution.

Figure 6.9 (b) and **Table 6.4** compare the dissolved Fe(II) for the fly ash samples in the presence of rutile and anatase. Under dark conditions, rutile increased the dissolved Fe(II) concentrations, whereas anatase decreased Fe(II) amounts in CFA 1 and CFA 2 samples. The iron dissolution remained almost unchanged when anatase was added to CFA 3 and CFA 4 samples. These data support the competitive mechanism we discussed earlier, where TiO_2 provides conduction band electrons for Fe reduction, which increases Fe leaching. On the other hand, TiO_2 decreases iron leaching by providing the extra surface for surface-mediated reduction.

Table 6. 4: Fe (II) fractions calculated from the dissolved Fe concentration at 48th hour.

%Dissolved Fe(II) = ([Dissolved Fe (II)] / [Total Dissolved Fe])*100%				
		Sample	Sample + Rutile	Sample + Anatase
CFA 1	Dark	39.1	44.3	40.5
	Light	25.3	82.4	79.5
CFA 2	Dark	29.2	35.5	49.9
	Light	19.6	81.9	86.1
CFA 3	Dark	13.1	15.2	26.0
	Light	21.9	79.2	83.5
CFA 4	Dark	5.0	7.6	3.8
	Light	27.2	80	83.5

TiO_2 has a more pronounced impact on Fe(II) leaching when exposed to solar radiation. According to **Figure 6.9(b)**, the presence of rutile increased Fe(II) leaching for CFA 1, CFA 2, CFA 3, and CFA 4 by 4.10, 9.22, 4.24, and 5.28 folds, respectively. Fe(II) dissolution increased by 3.76, 7.94, 5.13, and 5.24 folds for CFA 1, CFA 2, CFA 3, and CFA 4, respectively, when anatase was added. A similar trend was observed for the %Dissolved Fe(II), as tabulated in **Table 6.4**. These results suggest that fly ash mixing with either of the crystal phases of TiO_2 can leach out high total Fe and Fe(II) under solar radiation and, to some extent, dark conditions. Ti-enhanced iron leaching has been reported previously in our multiple previous studies.[82-84]

Our results highlight that TiO_2 undergoes additional reaction mechanisms in both phases in addition to the surface-mediated reduction to leach off total Fe and Fe(II). TiO_2 is a well-known photo-catalyst that can generate hydroxyl radical ($HO^{\cdot}$) from the adsorbed water when exposed to sun radiation.[236] This quick $HO^{\cdot}$ radical generation can significantly speed up the conversion of Fe(III) to Fe(II). Additionally, under solar radiation, TiO_2 can generate a sizable quantity of conduction band electrons, some of which can convert Fe(III) to Fe(II) using equation 6.6 and thereby raise the concentration of dissolved Fe and the proportion of Fe(II) in solution. Additionally, TiO_2 is known to increase surface defects under solar radiation, the majority of which are Ti(III) defects that also cause the reaction in equation 7 to convert Fe(III) to Fe(II).

$$Fe^{3+} + e_{cb}^{-} \rightarrow Fe^{2+} \quad \text{Eq. 6.6}$$

$$Ti^{3+} + Fe^{3+} \rightarrow Ti^{4+} + Fe^{2+} \quad \text{Eq. 6.7}$$

Protons also consume conduction band electrons generated in the reaction medium under highly acidic conditions to produce hydrogen gas, which raises the pH of the medium and may affect both the speciation and iron leaching. Additionally, the proton-promoted

pathway involves proton consumption, which raises the pH of the HNO_3 solution and affects iron leaching. **Figure 6.10** shows the pH measured after 48 hours of the dissolution experiment. The pH was not maintained over the reaction time, and the pH at the beginning of the dissolution experiment was set to 2. The pH of the entire reaction mixtures increased for all the dissolution experiments, supporting the previously established reaction process.

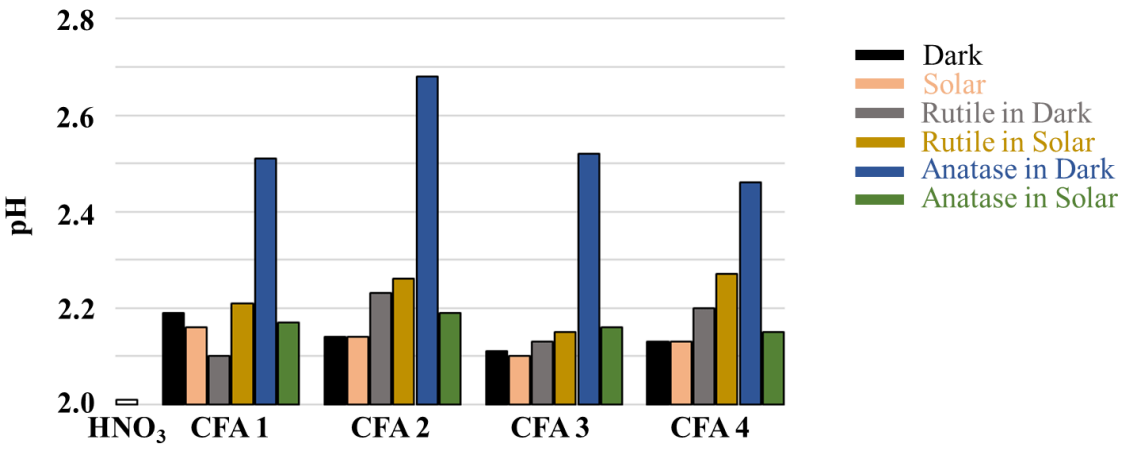

Figure 6. 10: pH of the dissolution media after 48 hours of iron leaching from CFAs.

6.5 Conclusions and Atmospheric Implications

In this work, the effect of titanium dioxide is examined explicitly in relation to the iron mobilization from coal fly ash (CFA) and hematite under simulated atmospheric conditions. We also investigated several other aspects of CFA particles that impact iron mobilization, including particle size, surface area, mineralogy, and composition. We also assessed the influence of solar flux iron leaching in the presence of TiO_2 particles. Our findings imply that CFA dissolved considerably more total Fe and Fe(II) than hematite on a surface area basis. Hematite has a larger specific surface area than other minerals, which may explain why it dissolved more quickly on a mass basis. Furthermore, under identical reaction conditions, the extent of iron dissolution from four distinct CFAs displayed notable variations that the mineralogy and elemental composition of the CFAs may explain. The coal burned to produce CFAs, as well as the combustion method and efficiency, strongly influence the mineralogy and composition. Thus, the source of the CFA has a significant impact on how much iron leaches out of a particular fly ash sample.

Iron leaching from CFAs by atmospheric processing with acidic gases depends critically on solar flux. The Ti:Fe ratio and the photochemistry of adsorbed anion on the particle surface are crucial to this process. While surface-mediated reduction of nitrate to nitrite becomes more favorable under solar light, which reduces overall Fe dissolution, the Ti content within the sample may initiate several photo-induced reactions, increasing the Fe leaching. Because of this competing reaction mechanism, CFA 4 sample, which has the highest Ti:Fe ratio of 0.2036, exhibits the most significant enhancement in the total Fe and Fe(II) leaching among the samples, whereas the CFA 2 sample, which has the lowest Ti:Fe ratio of 0.0805, exhibits the largest decrease in the Fe leaching under solar flux. In the presence of externally added TiO_2, the impact of solar radiation is more pronounced. Given

TiO_2 (anatase and rutile) is such a good adsorbent of anion NO_3^-, it provides competition for surface complexation and favors surface-mediated reduction, which reduces the overall amount of Fe leaching. Moreover, it is known that both anatase and rutile include surface defects of Ti(III) that increase under solar radiation. These defects can also produce conduction band electrons dark and light conditions, which can ultimately reduce Fe(III) to Fe(II) and accelerate dissolution. Additionally, under solar irradiation, TiO_2 generates $HO^{\cdot}$ radicals from adsorbed water molecules, which accelerates the conversion of Fe(III) to Fe(II). Due to this opposing mechanism, the augmentation of total iron dissolution caused by TiO_2 is not noticeable in low light. However, the presence of TiO_2 in light conditions increases the overall iron dissolution. Additionally, externally supplied TiO_2 (anatase and rutile) enhances Fe(II) generation, potentially making iron accessible in both dark and light conditions.

Thus, the current study's main focus was on the iron leaching from coal fly ashes in atmospherically appropriate conditions when TiO_2 was present. The distribution of coal fly ashes varies by location, and it is anticipated that it will be higher in industrialized areas, where it will also result in higher atmospheric processing of CFAs to produce bioavailable Fe deposition. Furthermore, TiO_2 is a commonly utilized semiconductor material that is predicted to have a higher distribution around industrialized areas. Our research indicates that TiO_2 increases the production of bioavailable iron. Therefore, while assessing the global ocean's primary productivity and the deposition of bioavailable iron, it is essential to understand the distribution components. The current study further focused on acidic processing with HNO_3 at pH 2, whereas the environment is a more complicated system with other acidic gases that can result in various reaction mechanisms. Therefore, additional study is advised to comprehend the influence the pH and other acidic gases. It is also crucial to understand these reaction mechanisms of bioavailable Fe production to improve the predictability of biogeochemical models.

6.6 Acknowledgement

The authors thank US geological survey (USGS) for providing the samples for the research reported in this chapter. Thanks to Dr. Virgil Lueth, and Kelsey McNamara at the New Mexico Bureau of Geology for providing the facility to perform XRD. SEM images were collected using the user facility of CINT. The material presented in this chapter remain unpublished and author holds the copyright.

CHAPTER 7

CONCLUSIONS AND FUTURE DIRECTIONS

Mine workers and residents in the surrounding community are at risk of inhaling industrial or mine dust, which has been identified as a major contributor to a variety of lung conditions, cardiovascular diseases, and metabolic disorders. Industrial dust in areas where commercial mining occurs has elevated heavy metal concentrations in the respirable fraction of the dust that has lifted into the atmosphere. Inhaling the respirable fraction of dust particles causes them to potentially deposit in different regions of the respiratory tract as well as the gastrointestinal tract, depending on their size. Furthermore, when inhaled particles interact with physiological fluids in the stomach and lungs, these heavy metals seep out, significantly increasing their bio-accessibility. The bioleaching of these heavy metals from dust is affected not only by dust concentration and exposure but also by their various physicochemical properties, which can result in a wide range of toxicity. Thus, laboratory and computational model studies, in conjunction with field observations, collaborate to develop better methods for predicting the human toxicity of any specific dust. While these dust particles are hazardous to human health, they also frequently alter the atmosphere's chemical balance through heterogeneous processes and thus influence the climate. Furthermore, they are the primary source of bioavailable iron in the global ocean, which influences the productivity of phytoplankton and diatoms, which are known to be the primary producers and CO_2 sequesters. Hence, research into the atmospheric processing of dust particles could lead to more accurate climate predictions.

Understanding industrial dust interactions with specific bodily fluids and ambient gases are vital in these studies. We used a variety of laboratory experiments coupled with computational calculations to achieve this goal. The surface functional group was determined using ATR-FTIR. Scanning electron microscopy (SEM) was used to determine particle size and shape, and X-ray diffraction was employed detecting mineralogy. In addition, several other complementary characterization techniques, such as BET surface area measurements, micro-pore analysis, and microwave acid digestion under high pressure, were carried out. The chemical composition and concentration of bio-leached metals were determined using dissolution experiments followed by ICP-MS or UV-Vis analysis.

The toxicity of inhaled mine dust was investigated in the first part of this study. While small dust particles (less than 4 micrometers) can penetrate deep into the lungs, larger dust particles can be cleared through the gastrointestinal tract. Although these particles are expelled from the body as a self-defense mechanism, the interaction of lung fluids and gastrointestinal fluids with dust particles has the potential to leach out heavy metals and some non-metals, many of which are hazardous. In the scope of this study, we

have investigated uranium mine dust and respirable coal mine dust and their human health implications.

Uranium can damage kidneys, cause renal diseases, and alter gut flora when ingested through the digestive system. However, only a handful of toxicological investigations have focused on uranium-containing dust passing through the digestive system. Therefore, in light of how these dust particles behave in the gastrointestinal tract, we studied the mineralogy-controlled dissolution of uranium and other metals and non-metals in gastric and intestinal fluids. Our findings imply that uranium from the dust particles leached into body fluids, and it was clear that some samples dissolved more readily in conditions resembling those of the human stomach than others did in those of the intestine. Further, we reported that differences in dust solubility in body fluids are partially a result of the mineralogical variations, which was confirmed by our experimentally collected mineralogical data and computational geochemical calculations. The extent of uranium dissolution is influenced by the type of uranium minerals and the presence of non-uranium minerals, i.e., kaolinite and microcline. Uranium in solution was most frequently found in the U^{+6} oxidation state. Therefore, we demonstrate that it is conceivable for solid uranium to dissolve in the human digestive system after inhalation and that site-specific mineralogy determine the extent of uranium concentration and its speciation. The toxicological evaluations and risk assessment models should therefore consider these factors. In addition, the authors recommend more research to understand the interaction of human gut microbiota with uranium present in inhalable dust, given the paucity of data on the effects of dissolved uranium on gut microbiota.

We further investigated the respirable coal mine dust (RCMD) toxicity that was cleared to the lungs. Despite the number of studies linking RCMD exposure to various lung conditions, only a few have focused on the physicochemical characteristics of the dust and their link to health issues. Therefore, in the current study, we assessed the RCMD collected from different mines located in different geographical regions and also from different sources within the mine. Here, the toxicity of RCMD was assessed based on their ability to leach metals and the inflammatory response in relation to their physicochemical properties. The first portion of this work reports data on the bio-accessibility of RCMD from two US regions (the Appalachian region and the Rocky Mountains). Here we compared the variations of samples to determine trends connected to the geographic location. This study examined the characteristics and toxicity of the RCMD fraction that only came from the coal seam. Our results highlighted that geographic location does not solely influence toxicity. This suggests that other factors, such as the exposure to RCMD, the particle size distribution of the actual RCMD in each mine, and the mineral contributions from the various sources in the mine to the RCMD that the miners inhale, may be significantly different in each region and contribute to the higher incidence of lung diseases in the Appalachian region.

The second part of the RCMD work focused on different types of aerosols generated during mining operations and dust collected from various physical locations of the mine. We selected the coal seam, host floor, and host roof of each mine since their physicochemical makeup can vary and lead to different toxicity. In-vitro assays and metal leaching studies were carried out in simulated lung fluids (SLF), such as Gamble Solution

(GS) and Artificial Lysosomal Fluid (ALF), on the RCMD samples taken from three different mines. Furthermore, rock dust, which primarily consists of stable oxides like silicates and carbonates, is applied to prevent coal dust explosions in underground coal mines, another potential source of RCMD. Our results indicate that Si and Al, together with a relatively small amount of other metals, including Fe, Sr, Ba, and Pb, were the most widely dissolved in the dissolution experiments. We report that metal leaching was most prevalent in the dust from floors and roofs and least prevalent in coal seams and rock dust. Moreover, a significant impact on immunological response and cell survival was also seen in in-vitro experiment results for floor and roof dust samples, indicating higher toxicity. Overall, our results indicate that RCMD toxicity cannot be generalized and greatly differs depending on their physicochemical features, many of which are derived from the unique sources from which they are formed.

In this thesis work, we also investigated coal fly ashes (CFA) as a potential source of bioavailable iron for the ocean. We performed laboratory experiments to determine Fe leaching for four coal fly ash samples under simulated atmospheric processing. Our study shows that CFA dissolves substantially to produce total Fe and Fe(II). On a surface area basis, the dissolved Fe from coal fly ash was higher than that of hematite (α-Fe_2O_3), the most commonly used iron oxide proxy in atmospheric modeling. Furthermore, the amount of iron that dissolves from four different CFAs varies noticeably under identical reaction conditions. The mineralogy and elemental composition of the CFAs can be used to explain these variations. The mineralogy and composition of CFAs are significantly influenced by the coal burned, combustion technique, and efficiency. Therefore, the amount of iron that leaches out of a particular fly ash sample depends significantly on the source of the CFA. In addition, under atmospherically relevant circumstances, we investigated Fe leaching and speciation from CFAs in the presence of TiO_2, a common engineered nanoparticle. Our findings show that iron leaching is enhanced by titanium concentration in the samples or by externally applied TiO_2, which is more pronounced in the presence of solar flux. These enhancements are primarily due to the ability of TiO_2 to generate photo-induced conduction band electrons and $HO^{\cdot}$ radicals from the adsorbed water molecule. Both these pathways are known to facilitate the reduction of Fe(III) to Fe(II), overall increasing iron dissolution. As a result, atmospheric processing of CFAs will fertilize the ocean, which lacks dissolved iron, and, thus, significantly increases the ocean's primary productivity, particularly in and around industrial areas. Therefore, it is crucial to consider the distribution of these components when evaluating the primary productivity of the world's oceans and the deposition of bioavailable iron. The environment is a more complex system with additional acidic gases, and the current work concentrated on acidic processing with HNO_3 at pH 2, which can result in various reaction pathways that we are currently ignorant of. We suggest further research in this area to comprehend the impact of pH and other acidic gases fully. This knowledge is crucial to understanding bioavailable Fe production reaction mechanisms to improve the predictability of biogeochemical models.

In conclusion, the research provided in this thesis sheds light on the impact of mine dust mineralogy on human health. By understanding the effects of inhaled particles, the resulting cellular toxicity, and long-term health repercussions, we can develop better risk assessment models. These efforts will assist in detecting the reasons behind the lung disorders of many miners. The current work also sheds light on the atmospheric processing

of coal fly ash mixed with other engineered nanoparticles to fertilize the ocean. The atmospheric model would benefit significantly from incorporating new information from this study.

APPENDIX A

EQUATIONS, CALIBRATION PLOTS & COMPUTER CODES

A.1 Computation Calculations - Input Files for the SGIF Solutions Reprinted with permission from Hettiarachchi et al., 2022.[3]

The inbuilt MINTEQ database was used as the basic database. The other solid and aqueous species were imported from the other inbuilt databases (LLNL.dat, MINTEQ.v4.dat) within the model.

SGF Solution

```
PHASES
Uranophane
    Ca(UO2)2(SiO3OH)2 + 6H+ = 2UO2+2 + Ca+2 + 2H4SiO4
    log_k     17.49
    delta_h   0 kcal
    -Vm       68.32 cm3/mol
PHASES
Coffinite
    USiO4 + 4H+ = H4SiO4 + U+4
    log_k     -7.62
    delta_h   -14.548 kcal
    -Vm       68.32 cm3/mol
SURFACE_MASTER_SPECIES
    Uranophane    Ca(UO2)2(SiO3OH)2
SURFACE_MASTER_SPECIES
    Rutile        TiO2
SURFACE_MASTER_SPECIES
    Coffinite     USiO4
    Quartz        SiO2
SURFACE_SPECIES
SiO2 = SiO2
    log_k     -3.9993
    delta_h   32.949 kJ
SURFACE_SPECIES
TiO2 +2.0000 H2O  =  + 1.0000 Ti(OH)4
    log_k     -9.6452
    delta_h   -226.107 kJ
PHASES
Uranyl_carbonate
    Na4UO2(CO3)3 +3.0000 H+  =  + 1.0000 UO2++ + 3.0000 HCO3- +
4.0000 Na+
    log_k     4.0395
    delta_h   0 kcal
    -Vm       68.32 cm3/mol
PHASES
Rutile
    TiO2 +2.0000 H2O  =  + 1.0000 Ti(OH)4
    log_k     -9.6452
```

```
    delta_h   -226.107 kcal
    -Vm       68.32 cm3/mol
SURFACE_MASTER_SPECIES
    Uranyl_carbonate Na4UO2(CO3)3
SURFACE_SPECIES
Na4UO2(CO3)3 = Na4UO2(CO3)3
    log_k     0
SURFACE_SPECIES
TiO2 = TiO2
    log_k     0
PHASES
Microcline
    KAlSi3O8 + 4H2O + 4H+ = 3H4SiO4 + Al+3 + K+
    log_k     0.616
    delta_h   -12.309 kcal
SURFACE_MASTER_SPECIES
    Microcline    KAlSi3O8
SURFACE_SPECIES
KAlSi3O8 = KAlSi3O8
    log_k     0
SOLUTION_MASTER_SPECIES
    Lactate       Lactate-         0     90.08           90.08
SOLUTION_MASTER_SPECIES
    Ti            Ti(OH)4          0     47.88           47.88

SOLUTION_MASTER_SPECIES
    Taurine       Taurine-         0     125.15          125.15
SURFACE_SPECIES
Ca(UO2)2(SiO3OH)2 = Ca(UO2)2(SiO3OH)2
    log_k     0
    delta_h   0 kJ
SOLUTION_SPECIES
Lactate- = Lactate-
    log_k     0
Lactate- + H+ = LactateH
    log_k     3.86
    delta_h   -1361.9 kJ
SOLUTION_SPECIES
Ti(OH)4 = Ti(OH)4
    log_k     0
SOLUTION_SPECIES
Taurine- = Taurine-
    log_k     0
H+ + Taurine- = TaurineH
    log_k     8.82

SOLUTION_MASTER_SPECIES
    Pyruvate      Pyruvate-        0     88.06           88.06
SOLUTION_SPECIES
Pyruvate- = Pyruvate-
    log_k     0
Pyruvate- + H+ = PyruvateH
    log_k     2.5
EQUILIBRIUM_PHASES 1
    Autunite  0 0
    Calcite   0 0
    Carnotite 0 0
```

```
    Coffinite 0 0
    Dolomite(disordered) 0 0
    Kaolinite 0 0
    Microcline 0 0
    Quartz    0 0
    Schoepite 0 0
    Torbernite 0 0
    Tyuyamunite 0 0
    Uraninite 0 0
    Uranophane 0 0
    Uranyl_carbonate 0 0
    Rutile    0 0
SOLUTION 2
    temp      37
    pH        1.6
    pe        4
    redox     pe
    units     mmol/l
    density   1
    Cl        34.2
    Glycine   0.003
    Na        34.28
    P         0.02
    Taurine   0.08
    -water    0.1 # kg
GAS_PHASE 1
    -fixed_volume
    -equilibrium with solution 2
    -pressure 1
    -volume 1
    -temperature 37
    O2(g)     1
SURFACE_SPECIES
USiO4 = USiO4
    log_k     0
```

SIF Solution

```
PHASES
Uranophane
    Ca(UO2)2(SiO3OH)2 + 6H+ = 2UO2+2 + Ca+2 + 2H4SiO4
    log_k     17.49
    delta_h   0 kcal
    -Vm       68.32 cm3/mol
PHASES
Coffinite
    USiO4 + 4H+ = H4SiO4 + U+4
    log_k     -7.62
    delta_h   -14.548 kcal
    -Vm       68.32 cm3/mol
SURFACE_MASTER_SPECIES
    Uranophane    Ca(UO2)2(SiO3OH)2
SURFACE_MASTER_SPECIES
    Rutile        TiO2
SURFACE_MASTER_SPECIES
    Coffinite     USiO4
```

```
    Quartz        SiO2
SURFACE_SPECIES
SiO2 = SiO2
    log_k     -3.9993
    delta_h   32.949 kJ
SURFACE_SPECIES
TiO2 +2.0000 H2O  =  + 1.0000 Ti(OH)4
    log_k     -9.6452
    delta_h   -226.107 kJ
PHASES
Uranyl_carbonate
    Na4UO2(CO3)3 +3.0000 H+  =  + 1.0000 UO2++ + 3.0000 HCO3- +
4.0000 Na+
    log_k     4.0395
    delta_h   0 kcal
    -Vm       68.32 cm3/mol
PHASES
Rutile
    TiO2 +2.0000 H2O  =  + 1.0000 Ti(OH)4
    log_k     -9.6452
    delta_h   -226.107 kcal
    -Vm       68.32 cm3/mol
SURFACE_MASTER_SPECIES
    Uranyl_carbonate Na4UO2(CO3)3
SURFACE_SPECIES
Na4UO2(CO3)3 = Na4UO2(CO3)3
    log_k     0
SURFACE_SPECIES
TiO2 = TiO2
    log_k     0
PHASES
Microcline
    KAlSi3O8 + 4H2O + 4H+ = 3H4SiO4 + Al+3 + K+
    log_k     0.616
    delta_h   -12.309 kcal
SURFACE_MASTER_SPECIES
    Microcline    KAlSi3O8
SURFACE_SPECIES
KAlSi3O8 = KAlSi3O8
    log_k     0
SOLUTION_MASTER_SPECIES
    Lactate       Lactate-         0     90.08          90.08
SOLUTION_MASTER_SPECIES
    Malate        Malate-          0     116            116
SOLUTION_MASTER_SPECIES
    Ti            Ti(OH)4          0     47.88          47.88

SOLUTION_MASTER_SPECIES
    Taurine       Taurine-         0     125.15         125.15
SURFACE_SPECIES
Ca(UO2)2(SiO3OH)2 = Ca(UO2)2(SiO3OH)2
    log_k     0
    delta_h   0 kJ
SOLUTION_SPECIES
Lactate- = Lactate-
    log_k     0
Lactate- + H+ = LactateH
```

```
    log_k     3.86
    delta_h   -1361.9 kJ
SOLUTION_SPECIES
Malate- = Malate-
    log_k     0
H+ + Malate- = MalateH
    log_k     1.9
SOLUTION_SPECIES
Ti(OH)4 = Ti(OH)4
    log_k     0
SOLUTION_SPECIES
Taurine- = Taurine-
    log_k     0
H+ + Taurine- = TaurineH
    log_k     8.82

SOLUTION_MASTER_SPECIES
    Pyruvate      Pyruvate-        0     88.06           88.06
SOLUTION_SPECIES
Pyruvate- = Pyruvate-
    log_k     0
Pyruvate- + H+ = PyruvateH
    log_k     2.5
EQUILIBRIUM_PHASES 1
    Autunite  0 0
    Calcite   0 0
    Carnotite 0 0
    Coffinite 0 0
    Dolomite(disordered) 0 0
    Kaolinite 0 0
    Microcline 0 0
    Quartz    0 0
    Schoepite 0 0
    Torbernite 0 0
    Tyuyamunite 0 0
    Uraninite 0 0
    Uranophane 0 0
    Uranyl_carbonate 0 0
    Rutile    0 0
SOLUTION 2
    temp      37
    pH        6.5
    pe        4
    redox     pe
    units     mmol/l
    density   1
    Cl        34.2
    Glycine   0.003
    Malate    19.12
    Na        34.28
    P         0.02
    Taurine   0.08
    -water    0.1 # kg
GAS_PHASE 1
    -fixed_volume
    -equilibrium with solution 2
    -pressure 1
```

```
    -volume 1
    -temperature 37
    O2(g)     1
SURFACE_SPECIES
USiO4 = USiO4
    log_k     0
```

Table A.1: Mineralogy Input to PHREEQC for the Computational Calculations.

Mineral	**Chemical Formula**	**St. A. S**	**St. A. R**	**Site K**	**Site L**	**Site M**
Quartz	SiO2	99	99	99	99	99
Dolomite	CaCO3.MgCO3	1	0	1	1	1
Microcline	KAlSi3O8	0	1	1	1	1
Kaolinite	Al2Si2O5(OH)4	1	1	1	1	1
Calcite	CaCO3	0	0	0	0	0
Rutile	TiO2	1	0	0	0	0
Uraninite	UO2	0.01	0	0.7	0.8	0.8
Coffinite	U(SiO4)1−x(OH)4x	0.01	1	0	0.4	0
Andersonite	Na2Ca(UO2)(CO3)3 · 6H2O	0	0.45	0.0003	0	0
Torbernite	Cu(UO2)2(PO4)2 • 12H2O	0	0.1	0	0.02	0.15
Tyuyamunite	Ca(UO2)2V2O8·(5-8)H2O	0	0	0.01	0.02	0.01
Carnotite	K2(UO2)2(VO4)2·3H2O	0	0.2	0.04	0	0
Uranophane	(Ca(UO2)2(SiO3OH)2·5H2O)	0.001	0.03	0.02	0.015	0
Schoephite	(UO2)8O2(OH)12•12(H2O)	0.1	0	0	0	0
Autunite	Ca(UO2)2(PO4)2·10–12H2O	0.08	1	0.2	0.15	0.25

APPENDIX B

PERMISSION

All the figures and table reused from author's published work appropriately cited in the text & are acknowledged at the end of the chapter.

Each permission is as follows:

1. Materials presented in the Chapter 2, 3, and the Appendix A, from the following work,

Reprinted (adopted) and does not require specific permission for reprint in the dissertation.

E. HETTIARACHCHI, M. DAS, D. CADOL, B. A. FREY AND G. RUBASINGHEGE, THE FATE OF INHALED URANIUM-CONTAINING PARTICLES UPON CLEARANCE TO GASTROINTESTINAL TRACT. ***Environ. Sci.: Processes Impacts*****, 2022**, 24, 1257 – 1266

2. Material presented in Chapter 2 and 4 is from the following work,

Reprinted (adopted) and does not require specific permission for reprint in the dissertation.

SALINAS, V.; DAS, M.; JACQUEZ, Q.; CAMACHO, A.; ZYCHOWSKI, K.; HOVINGH, M.; MEDINA, A.; RUBASINGHEGE, G.; REZAEE, M.; BALTRUSAITIS, J.; FAIRLEY, N.; ROGHANCHI, P. CHARACTERIZATION AND TOXICITY ANALYSIS OF LAB-CREATED RESPIRABLE COAL MINE DUST FROM THE APPALACHIANS AND ROCKY MOUNTAINS REGIONS. ***Minerals 2022***, 12, 898. https://doi.org/10.3390/min12070898

When you publish in a Royal Society of Chemistry journal, you keep the copyright of the manuscript. On this page you can learn more about our Licence to Publish and the rights you retain as an author. We also explain where you can deposit and share your article, and how to request permission to re-use other people's work.

Rights retained by authors

When the author accepts the exclusive licence to publish for a journal article, he/she retains certain rights that may be exercised without reference to the Royal Society of Chemistry.

Reproduce/republish portions of the article (including the abstract).

Photocopy the article and distribute such photocopies and distribute copies of the PDF of the article for personal or professional use only (the Royal Society of Chemistry makes this PDF available to the corresponding author of the article upon publication. Any such copies should not be offered for sale. Persons who receive or access the PDF mentioned above must be notified that this may not be made available further or distributed.).

Adapt the article and reproduce adaptations of the article for any purpose other than the commercial exploitation of a work similar to the original.

Reproduce, perform, transmit and otherwise communicate the article to the public in spoken presentations (including those that are accompanied by visual material such as slides, overheads and computer projections).

The author(s) must submit a written request to the Royal Society of Chemistry for any use other than those specified above.

All cases of republication/reproduction must be accompanied by an acknowledgement of first publication of the work by the Royal Society of Chemistry, the wording of which depends on the journal in which the article was published originally. The acknowledgement should also include a hyperlink to the article on the Royal Society of Chemistry website.

The author also has some rights concerning the deposition of the whole article.

REFERENCES

1. Hess-Kosa, K., Indoor air quality: sampling methodologies. 2010: CRC Press.
2. Hettiarachchi, E., et al., Mineralogy controlled dissolution of uranium from airborne dust in simulated lung fluids (SLFs) and possible health implications. Environmental Science & Technology Letters, 2019. **6**(2): p. 62-67.
3. Hettiarachchi, E., et al., The fate of inhaled uranium-containing particles upon clearance to gastrointestinal tract. Environmental Science: Processes & Impacts, 2022. **24**(8): p. 1257-1266.
4. Salinas, V., et al., Characterization and toxicity analysis of lab-created respirable coal mine dust from the Appalachians and Rocky Mountains regions. Minerals, 2022. **12**(7): p. 898.
5. Baldo, C., et al., Iron from coal combustion particles dissolves much faster than mineral dust under simulated atmospheric acidic conditions. Atmospheric Chemistry and Physics, 2022. **22**(9): p. 6045-6066.
6. Beer, C., et al., A systematic review of occupational exposure to coal dust and the risk of interstitial lung diseases. European Clinical Respiratory Journal, 2017. **4**(1): p. 1264711.
7. Chen, H., et al., Coal fly ash as a source of iron in atmospheric dust. Environmental Science & Technology, 2012. **46**(4): p. 2112-2120.
8. Al-Khashman, O.A., Heavy metal distribution in dust, street dust and soils from the work place in karak industrial estate, jordan. Atmospheric Environment, 2004. **38**(39): p. 6803-6812.
9. Khademi, H., et al., Environmental impact assessment of industrial activities on heavy metals distribution in street dust and soil. Chemosphere, 2019. **217**: p. 695-705.
10. Ordonez, A., et al., Distribution of heavy metals in the street dusts and soils of an industrial city in northern spain. Archives of Environmental Contamination and Toxicology, 2003. **44**(2): p. 0160-0170.
11. Kastury, F., E. Smith, and A.L. Juhasz, a critical review of approaches and limitations of inhalation bioavailability and bioaccessibility of metal (loid) s from ambient particulate matter or dust. Science of the Total Environment, 2017. **574**: p. 1054-1074.
12. Stine, K.E. and T.M. Brown, Principles of toxicology. 2015: CRC Press.
13. Thiébault, C., et al., Uranium induces apoptosis and is genotoxic to normal rat kidney (nrk-52e) proximal cells. Toxicological Sciences, 2007. **98**(2): p. 479-487.

14. Fubini, B. and C.O. Arean, Chemical aspects of the toxicity of inhaled mineral dusts. Chemical Society Reviews, 1999. **28**(6): p. 373-381.

15. Ghio, A.J., et al., Biological effects of desert dust in respiratory epithelial cells and a murine model. Inhalation Toxicology, 2014. **26**(5): p. 299-309.

16. Mahurpawar, M., Effects of heavy metals on human health. International journal of research - granthaalayah, 2015. **530**: p. 1-7.

17. McPherson, M.J., Subsurface ventilation and environmental engineering. 2012: Springer Science & Business Media.

18. Colinet, J., C.N. Halldin, and J. Schall, Best practices for dust control in coal mining. 2021.

19. Scaggs, M.L., Development and implementation of a standard methodology for respirable coal mine dust characterization with thermo-gravimetric analysis. 2016, Virginia Tech.

20. Jenkins, M.E. and A.H. Schroeder, a brief history of New Mexico. 1974: UNM Press.

21. Stearns, D.M., et al., Uranyl acetate induces hprt mutations and uranium–DNA adducts in Chinese hamster ovary em9 cells. Mutagenesis, 2005. **20**(6): p. 417-423.

22. Pereira, S., et al., Genotoxicity of uranium contamination in embryonic zebrafish cells. Aquatic Toxicology, 2012. **109**: p. 11-16.

23. Hsieh, P. and K. Yamane, DNA mismatch repair: molecular mechanism, cancer, and ageing. Mechanisms of Ageing and Development, 2008. **129**(7-8): p. 391-407.

24. Schneider, J., et al., ATM gene mutations in former uranium miners of sdag wismut: a pilot study. Oncology Reports, 2007. **17**(2): p. 477-482.

25. Periyakaruppan, A., et al., Uranium induces oxidative stress in lung epithelial cells. Archives of toxicology, 2007. **81**(6): p. 389-395.

26. Orona, N. and D. Tasat, Uranyl nitrate-exposed rat alveolar macrophages cell death: influence of superoxide anion and TNF α mediators. Toxicology and Applied Pharmacology, 2012. **261**(3): p. 309-316.

27. Organization, W.H., Hazard prevention and control in the work environment: Airborne Dust. 2002.

28. Nousiainen, T., Optical modeling of mineral dust particles: a review. Journal of Quantitative Spectroscopy and Radiative Transfer, 2009. **110**(14-16): p. 1261-1279.

29. Sarver, E., C. Keles, and M. Rezaee, Beyond conventional metrics: comprehensive characterization of respirable coal mine dust. International Journal of Coal Geology, 2019. **207**: p. 84-95.

30. Walton, W., et al., The effect of quartz and other non-coal dusts in coal workers' pneumoconiosis. Part I: Epidemiological Studies. Inhaled Particles, 1975. **4**: p. 669-690.

31. Kuempel, E.D., Occupational exposure to respirable Coal Mine Dust. 1995.

32. Douglas, A., et al., Dust exposure, dust recovered from the lung, and associated pathology in a group of british coalminers. Occupational and Environmental Medicine, 1986. **43**(12): p. 795-801.

33. Pandey, J.K., et al., Characterization of respirable dust exposure of different category of workers in jharia coalfields. Arabian Journal of Geosciences, 2017. **10**(7): p. 1-10.

34. Zosky, G.R., et al., Coal workers' pneumoconiosis: An Australian perspective. The Medical Journal of Australia, 2016. **204**(11): p. 414-418.

35. Sellaro, R., E. Sarver, and D. Baxter, A standard characterization methodology for respirable coal mine dust using SEM-EDX. Resources, 2015. **4**(4): p. 939-957.

36. Sarver, E., et al., Mineralogic analysis of respirable dust from 24 underground coal mines in four geographic regions of the united states, in A105. Silica, inorganic dust, and mining. 2020, American Thoracic Society. p. A2635-A2635.

37. Johann-Essex, V., C. Keles, and E. Sarver, A computer-controlled sem-edx routine for characterizing respirable coal mine dust. Minerals, 2017. **7**(1): p. 15.

38. Vassilev, S.V. and C.G. Vassileva, Geochemistry of coals, coal ashes and combustion wastes from coal-fired power stations. Fuel Processing Technology, 1997. **51**(1-2): p. 19-45.

39. Vassilev, S.V., et al., Phase-mineral and chemical composition of coal fly ashes as a basis for their multicomponent utilization. 1. Characterization of feed coals and fly ashes☆. Fuel, 2003. **82**(14): p. 1793-1811.

40. Vassilev, S.V. and C.G. Vassileva, Methods for characterization of composition of fly ashes from coal-fired power stations: A critical overview. Energy & Fuels, 2005. **19**(3): p. 1084-1098.

41. Fernandez-Turiel, J., et al., Mobility of heavy metals from coal fly ash. Environmental Geology, 1994. **23**(4): p. 264-270.

42. Ram, L.C., et al., Leaching behavior of lignite fly ash with shake and column tests. Environmental Geology, 2007. **51**(7): p. 1119-1132.

43. Sarode, D.B., et al., Extraction and leaching of heavy metals from thermal power plant fly ash and its admixtures. Polish Journal of Environmental Studies, 2010. **19**(6): p. 1325-1330.

44. Asic, A., et al., Chemical toxicity and radioactivity of depleted uranium: the evidence from in-vivo and in-vitro studies. Environmental Research, 2017. **156**: p. 665-673.

45. Briner, W., The toxicity of depleted uranium. International Journal of Environmental Research and Public Health, 2010. **7**(1): p. 303-313.

46. Monleau, M., et al., Distribution and genotoxic effects after successive exposure to different uranium oxide particles inhaled by rats. Inhalation Toxicology, 2006. **18**(11): p. 885-894.

47. Jiang, G.C. and M. Aschner, Depleted uranium, in handbook of toxicology of chemical warfare agents. 2015, Elsevier. p. 447-460.

48. Medina, S., et al., Exposures to uranium and arsenic alter intraepithelial and innate immune cells in the small intestine of male and female mice. Toxicology and Applied Pharmacology, 2020. **403**: p. 115155.

49. Frelon, S., et al., The chemical speciation of uranium in water does not influence its absorption from the gastrointestinal tract of rats. Chemical Research in Toxicology, 2005. **18**(7): p. 1150-1154.

50. Breton, J., et al., Ecotoxicology inside the gut: impact of heavy metals on the mouse microbiome. BMC Pharmacology and Toxicology, 2013. **14**(1): p. 1-11.

51. Chi, L., et al., Sex-specific effects of arsenic exposure on the trajectory and function of the gut microbiome. Chemical Research in Toxicology, 2016. **29**(6): p. 949-951.

52. Chi, L., et al., The effects of an environmentally relevant level of arsenic on the gut microbiome and its functional metagenome. Toxicological Sciences, 2017. **160**(2): p. 193-204.

53. Tsiaoussis, J., et al., Effects of single and combined toxic exposures on the gut microbiome: current knowledge and future directions. Toxicology Letters, 2019. **312**: p. 72-97.

54. Cleveland, D., J.E. Hinck, and J.S. Lankton, Elemental and radionuclide exposures and uptakes by small rodents, invertebrates, and vegetation at active and post-production uranium mines in the Grand Canyon watershed. Chemosphere, 2021. **263**: p. 127908.

55. National Academies of Sciences, E. and Medicine, Monitoring and sampling approaches to assess underground coal mine dust exposures. 2018.

56. Rubasinghege, G., et al., Simulated atmospheric processing of iron oxyhydroxide minerals at low pH: roles of particle size and acid anion in iron dissolution. Proceedings of the National Academy of Sciences, 2010. **107**(15): p. 6628-6633.

57. Ingall, E.D., et al., Enhanced iron solubility at low pH in global aerosols. Atmosphere, 2018. **9**(5): p. 201.

58. Wiederhold, J.G., et al., Iron isotope fractionation during proton-promoted, ligand-controlled, and reductive dissolution of goethite. Environmental Science & Technology, 2006. **40**(12): p. 3787-3793.

59. Rubasinghege, G. and V.H. Grassian, Photochemistry of adsorbed nitrate on aluminum oxide particle surfaces. The Journal of Physical Chemistry A, 2009. **113**(27): p. 7818-7825.

60. Cwiertny, D.M., M.A. Young, and V.H. Grassian, Chemistry and photochemistry of mineral dust aerosol. Annual Review of Physical Chemistry, 2008. **59**: p. 27-51.

61. Shelley, R.U., et al., Regional trends in the fractional solubility of Fe and other metals from North Atlantic aerosols (GEOTRACES cruises GA01 and GA03) following a two-stage leach. Biogeosciences, 2018. **15**(8): p. 2271-2288.

62. Ito, A. and Z. Shi, Delivery of anthropogenic bioavailable iron from mineral dust and combustion aerosols to the ocean. Atmospheric Chemistry and Physics, 2016. **16**(1): p. 85-99.

63. Cwiertny, D.M., et al., Characterization and acid-mobilization study of iron-containing mineral dust source materials. Journal of Geophysical Research: Atmospheres, 2008. **113**(D5).

64. Fu, H., et al., Photoreductive dissolution of Fe-containing mineral dust particles in acidic media. Journal of Geophysical Research: Atmospheres, 2010. **115**(D11).

65. Shi, Z., et al., Iron dissolution kinetics of mineral dust at low pH during simulated atmospheric processing. Atmospheric Chemistry and Physics, 2011. **11**(3): p. 995-1007.

66. Ito, A., G. Lin, and J.E. Penner, Radiative forcing by light-absorbing aerosols of pyrogenetic iron oxides. Scientific Reports, 2018. **8**(1): p. 1-11.

67. Rathod, S.D., et al., A mineralogy-based anthropogenic combustion-iron emission inventory. Journal of Geophysical Research: Atmospheres, 2020. **125**(17): p. e2019JD032114.

68. Ito, A., et al., Ocean fertilization by pyrogenic aerosol iron. npj Climate and Atmospheric Science, 2021. **4**(1): p. 1-20.

69. Jickells, T. and C.M. Moore, The importance of atmospheric deposition for ocean productivity. Annual Review of Ecology, Evolution, and Systematics, 2015. **46**: p. 481-501.

70. Jickells, T., et al., Global iron connections between desert dust, ocean biogeochemistry, and climate. Science, 2005. **308**(5718): p. 67-71.

71. Kanakidou, M., S. Myriokefalitakis, and K. Tsigaridis, Aerosols in atmospheric chemistry and biogeochemical cycles of nutrients. Environmental Research Letters, 2018. **13**(6): p. 063004.

72. Mahowald, N.M., et al., Observed 20th century desert dust variability: impact on climate and biogeochemistry. Atmospheric Chemistry and Physics, 2010. **10**(22): p. 10875-10893.

73. Shi, Z., et al., Impacts on iron solubility in the mineral dust by processes in the source region and the atmosphere: A review. Aeolian Research, 2012. **5**: p. 21-42.

74. Wang, R., et al., Sources, transport and deposition of iron in the global atmosphere. Atmospheric Chemistry and Physics, 2015. **15**(11): p. 6247-6270.

75. Chen, H. and V.H. Grassian, Iron dissolution of dust source materials during simulated acidic processing: the effect of sulfuric, acetic, and oxalic acids. Environmental Science & Technology, 2013. **47**(18): p. 10312-10321.

76. Veranth, J.M., et al., Mössbauer spectroscopy indicates that iron in an aluminosilicate glass phase is the source of the bioavailable iron from coal fly ash. Chemical Research in Toxicology, 2000. **13**(3): p. 161-164.

77. Baker, A. and T. Jickells, Mineral particle size as a control on aerosol iron solubility. Geophysical Research Letters, 2006. **33**(17).

78. Journet, E., et al., Mineralogy as a critical factor of dust iron solubility. Geophysical

Research Letters, 2008. **35**(7).

79. Cwiertny, D.M., et al., Surface chemistry and dissolution of α-FeOOH nanorods and microrods: Environmental implications of size-dependent interactions with oxalate. The Journal of Physical Chemistry C, 2009. **113**(6): p. 2175-2186.
80. Shi, Z., et al., Formation of iron nanoparticles and increase in iron reactivity in mineral dust during simulated cloud processing. Environmental Science & Technology, 2009. **43**(17): p. 6592-6596.
81. Schroth, A.W., et al., Iron solubility driven by speciation in dust sources to the ocean. Nature Geoscience, 2009. **2**(5): p. 337-340.
82. Hettiarachchi, E., et al., Iron dissolution and speciation in atmospheric mineral dust: Metal-metal synergistic and antagonistic effects. Atmospheric Environment, 2018. **187**: p. 417-423.
83. Hettiarachchi, E., O. Hurab, and G. Rubasinghege, Atmospheric processing and iron mobilization of ilmenite: Iron-containing ternary oxide in mineral dust aerosol. The Journal of Physical Chemistry A, 2018. **122**(5): p. 1291-1302.
84. Hettiarachchi, E. and G. Rubasinghege, Mechanistic study on iron solubility in atmospheric mineral dust aerosol: roles of titanium, dissolved oxygen, and solar flux in solutions containing different acid anions. ACS Earth and Space Chemistry, 2020. **4**(1): p. 101-111.
85. Yadav, V.K., et al., Variations and similarities in structural, chemical, and elemental properties on the ashes derived from the coal due to their combustion in open and controlled manner. Environmental Science and Pollution Research, 2021. **28**(25): p. 32609-32625.
86. Kursun Unver, I. and M. Terzi, Distribution of trace elements in coal and coal fly ash and their recovery with mineral processing practices: A review. Journal of Mining and Environment, 2018. **9**(3): p. 641-655.
87. Sahoo, P.K., et al., Recovery of metals and other beneficial products from coal fly ash: A sustainable approach for fly ash management. International Journal of Coal Science & Technology, 2016. **3**(3): p. 267-283.
88. Luo, C., et al., Combustion iron distribution and deposition. Global Biogeochemical Cycles, 2008. **22**(1).
89. Li, W. and L. Shao, Transmission electron microscopy study of aerosol particles from the brown hazes in northern China. Journal of Geophysical Research: Atmospheres, 2009. **114**(D9).
90. Chin, M. and R. Kahn, Atmospheric aerosol properties and climate impacts. Vol. 2. 2009: US Climate Change Science Program.
91. Penner, J.E., et al., Aerosols, their direct and indirect effects, in Climate change 2001: the scientific basis. Contribution of working group I to the third assessment report of the intergovernmental panel on climate change. 2001, Cambridge University Press. p. 289-348.

92. Usher, C.R., A.E. Michel, and V.H. Grassian, Reactions on mineral dust. Chemical Reviews, 2003. **103**(12): p. 4883-4940.

93. Tang, M., et al., Heterogeneous reactions of mineral dust aerosol: implications for tropospheric oxidation capacity. Atmospheric Chemistry and Physics, 2017. **17**(19): p. 11727-11777.

94. Kameda, T., et al., Mineral dust aerosols promote the formation of toxic nitropolycyclic aromatic compounds. Scientific Reports, 2016. **6**(1): p. 1-10.

95. Wilson, S.A., USGS certificate of analysis; coal, lower Bakerstown CLB-1. 1997, USGS Eastern Energy Resources Team.

96. Stucki, J., The quantitative assay of minerals for Fe^{2+} and Fe^{3+} using 1, 10-phenanthroline: ii. A photochemical method. Soil Science Society of America Journal, 1981. **45**(3): p. 638-641.

97. Hughes, M.E. and L.J. Waite, Health in household context: living arrangements and health in late middle age. Journal of Health and Social Behavior, 2002. **43**(1): p. 1.

98. Erdei, E., et al., Elevated autoimmunity in residents living near abandoned uranium mine sites on the Navajo Nation. Journal of Autoimmunity, 2019. **99**: p. 15-23.

99. Ferrario, D., L. Gribaldo, and T. Hartung, Arsenic exposure and immunotoxicity: a review including the possible influence of age and sex. Current Environmental Health Reports, 2016. **3**(1): p. 1-12.

100. Wilson, A., et al., Mine-site derived particulate matter exposure exacerbates neurological and pulmonary inflammatory outcomes in an autoimmune mouse model. Journal of Toxicology and Environmental Health, Part A, 2021. **84**(12): p. 503-517.

101. Alpofead, J.A.H., C.M. Davidson, and D. Littlejohn, A novel two-step sequential bioaccessibility test for potentially toxic elements in inhaled particulate matter transported into the gastrointestinal tract by mucociliary clearance. Analytical and Bioanalytical Chemistry, 2017. **409**(12): p. 3165-3174.

102. Martin, R., et al., Health effects associated with inhalation of airborne arsenic arising from mining operations. Geosciences, 2014. **4**(3): p. 128-175.

103. Smith, J., et al., A study of aerosol deposition and clearance from the human nasal passage. Annals of Occupational Hygiene, 2002. **46**(suppl_1): p. 309-313.

104. Guney, M., et al., Lung bioaccessibility of As, Cu, Fe, Mn, Ni, Pb, and Zn in fine fraction (< 20 μm) from contaminated soils and mine tailings. Science of the Total Environment, 2017. **579**: p. 378-386.

105. Marques, M.R., R. Loebenberg, and M. Almukainzi, Simulated biological fluids with possible application in dissolution testing. Dissolution Technologies, 2011. **18**(3): p. 15-28.

106. McGuigan, M.A., 21 - Chronic poisoning: trace metals and others, in Goldman's Cecil Medicine (Twenty Fourth Edition), L. Goldman and A.I. Schafer, Editors. 2012, W.B. Saunders: Philadelphia. p. 88-95.

107. Krauskopf, K.B. and D.K. Bird, Introduction to geochemistry. Vol. 721. 1967: McGraw-Hill New York.

108. Zychowski, K.E., et al., Respirable uranyl-vanadate-containing particulate matter derived from a legacy uranium mine site exhibits potentiated cardiopulmonary toxicity. Toxicological Sciences, 2018. **164**(1): p. 101-114.

109. Parkhurst, D.L. and C. Appelo, Description of input and examples for PHREEQC version 3—a computer program for speciation, batch-reaction, one-dimensional transport, and inverse geochemical calculations. US Geological Survey Techniques and Methods, 2013. **6**(A43): p. 497.

110. Sun, H., Association of soil selenium, strontium, and magnesium concentrations with Parkinson's disease mortality rates in the USA. Environmental Geochemistry and Health, 2018. **40**(1): p. 349-357.

111. Brown, R.D., Geochemistry and transport of uranium-bearing dust at Jackpile mine, Laguna, New Mexico. 2017, New Mexico Institute of Mining and Technology.

112. Zhu, J.-H., et al., Selective colorimetric and fluorescent quenching determination of uranyl ion via its complexation with curcumin. Spectrochimica Acta Part A: Molecular and Biomolecular Spectroscopy, 2016. **159**: p. 146-150.

113. Wilton, T., Uranium deposits at the Cebolleta project, Laguna mining district, Cibola County, New Mexico. New Mexico Geological Society, 2017. **39**: p. 1-10.

114. Kogianni, E., A. Kouras, and C. Samara, Indoor concentrations of $PM_{2.5}$ and associated water-soluble and labile heavy metal fractions in workplaces: implications for inhalation health risk assessment. Environmental Science and Pollution Research, 2021. **28**(42): p. 58983-58993.

115. Chen, L.C. and M. Lippmann, Effects of metals within ambient air particulate matter (PM) on human health. Inhalation Toxicology, 2009. **21**(1): p. 1-31.

116. Mercer, R.R., et al., The fate of inhaled nanoparticles: detection and measurement by enhanced dark-field microscopy. Toxicologic Pathology, 2018. **46**(1): p. 28-46.

117. Wang, Z., et al., Ligand-promoted photoreductive dissolution of goethite by atmospheric low-molecular dicarboxylates. The Journal of Physical Chemistry A, 2017. **121**(8): p. 1647-1656.

118. Perdrial, N., et al., Uranium speciation in acid waste-weathered sediments: The role of aging and phosphate amendments. Applied Geochemistry, 2018. **89**: p. 109-120.

119. Gonzalez-Estrella, J., et al., Effect of bicarbonate, calcium, and pH on the reactivity of As (V) and U (VI) mixtures. Environmental Science & Technology, 2020. **54**(7): p. 3979-3987.

120. Guibal, E., C. Roulph, and P. Le Cloirec, Uranium biosorption by a filamentous fungus Mucor miehei pH effect on mechanisms and performances of uptake. Water Research, 1992. **26**(8): p. 1139-1145.

121. Harmon, M.E., et al., Residential proximity to abandoned uranium mines and serum inflammatory potential in chronically exposed Navajo communities. Journal of

Exposure Science & Environmental Epidemiology, 2017. **27**(4): p. 365-371.

122. Avasarala, S., et al., Effect of bicarbonate and oxidizing conditions on U (IV) and U (VI) reactivity in mineralized deposits of New Mexico. Chemical Geology, 2019. **524**: p. 345-355.

123. Alstadt, V.J., J.D. Kubicki, and M.A. Freedman, Competitive adsorption of acetic acid and water on kaolinite. The Journal of Physical Chemistry A, 2016. **120**(42): p. 8339-8346.

124. Taha, M., et al., Uranium sorption from commercial phosphoric acid using kaolinite and metakaolinite. Journal of Radioanalytical and Nuclear Chemistry, 2018. **317**(2): p. 685-699.

125. Doi, A., et al., Specificity and affinity of multivalent ions adsorption to kaolinite surface. Applied Clay Science, 2020. **190**: p. 105557.

126. Shekarian, Y., et al., Respirable coal mine dust: a review of respiratory deposition, regulations, and characterization. Minerals, 2021. **11**(7): p. 696.

127. Trechera, P., et al., Mineralogy, geochemistry and toxicity of size-segregated respirable deposited dust in underground coal mines. Journal of Hazardous Materials, 2020. **399**: p. 122935.

128. Brown, J.S., et al., Thoracic and respirable particle definitions for human health risk assessment. Particle and Fibre Toxicology, 2013. **10**(1): p. 1-12.

129. Shangguan, Y., et al., Mineralogical and geochemical variations from coal to deposited dust and toxicity of size-segregated respirable dust in a blasting mining underground coal mine in Hunan Province, South China. International Journal of Coal Geology, 2021. **248**: p. 103863.

130. Nesterova, A., et al., Endocrine, nutritional, and metabolic diseases. Disease Pathways: An Atlas of Human Disease Signaling Pathways, 2019. **1**: p. 121-218.

131. dos S Antao, V., et al., Rapidly progressive coal workers' pneumoconiosis in the United States: geographic clustering and other factors. Occupational and Environmental Medicine, 2005. **62**(10): p. 670-674.

132. Rahimi, E., Investigation of respirable coal mine dust (RCMD) and respirable crystalline silica (RCS) in the us underground and surface coal mines. 2020: New Mexico Institute of Mining and Technology.

133. Shekarian, Y., et al., An analysis of contributing mining factors in coal workers' pneumoconiosis prevalence in the United States coal mines, 1986–2018. International Journal of Coal Science & Technology, 2021. **8**(6): p. 1227-1237.

134. Kuempel, E., et al., Pulmonary inflammation and crystalline silica in respirable coal mine dust: dose response. Journal of Biosciences, 2003. **28**(1): p. 61-69.

135. Fairley, N., et al., Systematic and collaborative approach to problem solving using X-ray photoelectron spectroscopy. Applied Surface Science Advances, 2021. **5**: p. 100112.

136. Blume, R., et al., Characterizing graphitic carbon with X-ray photoelectron spectroscopy: a step-by-step approach. ChemCatChem, 2015. **7**(18): p. 2871-2881.

137. Moeini, B., et al., Definition of a new (Doniach-Sunjic-Shirley) peak shape for fitting asymmetric signals applied to reduced graphene oxide/graphene oxide XPS spectra. Surface and Interface Analysis, 2022. **54**(1): p. 67-77.

138. Pelfrêne, A., et al., In vitro investigations of human bioaccessibility from reference materials using simulated lung fluids. International Journal of Environmental Research and Public Health, 2017. **14**(2): p. 112.

139. Warr, L.N., IMA–CNMNC approved mineral symbols. Mineralogical Magazine, 2021. **85**(3): p. 291-320.

140. Whitney, D.L. and B.W. Evans, Abbreviations for names of rock-forming minerals. American Mineralogist, 2010. **95**(1): p. 185-187.

141. Singh, G.B. and K.V. Subramaniam, Quantitative XRD study of amorphous phase in alkali activated low calcium siliceous fly ash. Construction and Building Materials, 2016. **124**: p. 139-147.

142. Skibsted, L.H., J. Risbo, and M.L. Andersen, Chemical deterioration and physical instability of food and beverages. 2010: Elsevier.

143. Lin, S., et al., A study on the FTIR spectra of pre- and post-explosion coal dust to evaluate the effect of functional groups on dust explosion. Process Safety and Environmental Protection, 2019. **130**: p. 48-56.

144. Southwick, J.G., Solubility of silica in alkaline solutions: implications for alkaline flooding. Society of Petroleum Engineers Journal, 1985. **25**(06): p. 857-864.

145. Jaishankar, M., et al., Toxicity, mechanism and health effects of some heavy metals. Interdisciplinary Toxicology, 2014. **7**(2): p. 60.

146. Becaria, A., A. Campbell, and S. Bondy, Aluminum as a toxicant. Toxicology and Industrial Health, 2002. **18**(7): p. 309-320.

147. Yokel, R.A., The toxicology of aluminum in the brain: a review. 2000.

148. Inan, E.E. and A. Ayaz, Is aluminum exposure a risk factor for neurological disorders? 2018.

149. Jeffery, E., et al., Systemic aluminum toxicity: effects on bone, hematopoietic tissue, and kidney. Journal of Toxicology and Environmental Health Part A, 1996. **48**(6): p. 649-666.

150. Cecala, A.B., et al., Best practices for dust control in metal/nonmetal mining. 2010.

151. Papanikolaou, G. and K. Pantopoulos, Iron metabolism and toxicity. Toxicology and Applied Pharmacology, 2005. **202**(2): p. 199-211.

152. Huang, X., Iron overload and its association with cancer risk in humans: evidence for iron as a carcinogenic metal. Mutation Research/Fundamental and Molecular Mechanisms of Mutagenesis, 2003. **533**(1-2): p. 153-171.

153. Sebastiani, G. and K. Pantopoulos, Disorders associated with systemic or local iron

overload: from pathophysiology to clinical practice. Metallomics, 2011. **3**(10): p. 971-986.

154. Fishbane, S., A. Mathew, and N.D. Vaziri, Iron toxicity: relevance for dialysis patients. Nephrology Dialysis Transplantation, 2014. **29**(2): p. 255-259.

155. Sukiennicki, G.M., et al., Iron levels, genes involved in iron metabolism and antioxidative processes and lung cancer incidence. PLOS one, 2019. **14**(1): p. e0208610.

156. Pietrangelo, A., Mechanism of iron toxicity. Iron Chelation Therapy, 2002: p. 19-43.

157. Chanvorachote, P. and S. Luanpitpong, Iron induces cancer stem cells and aggressive phenotypes in human lung cancer cells. American Journal of Physiology-Cell Physiology, 2016. **310**(9): p. C728-C739.

158. Kuang, Y. and Q. Wang, Iron and lung cancer. Cancer Letters, 2019. **464**: p. 56-61.

159. Raha, S., et al., Is copper beneficial for COVID-19 patients? Medical Hypotheses, 2020. **142**: p. 109814.

160. Gaetke, L.M., H.S. Chow-Johnson, and C.K. Chow, Copper: toxicological relevance and mechanisms. Archives of Toxicology, 2014. **88**(11): p. 1929-1938.

161. Hong, Y.-j., et al., Progress in the research of the toxicity effect mechanisms of heavy metals on freshwater organisms and their water quality criteria in China. Journal of Chemistry, 2020. **2020**.

162. Zamberlan, D., et al., Copper decreases associative learning and memory in Drosophila melanogaster. Science of the Total Environment, 2020. **710**: p. 135306.

163. Ouni, S., et al., Toxicity and effects of copper oxide nanoparticles on cognitive performances in rats. Archives of Environmental & Occupational Health, 2020. **75(**7): p. 384-394.

164. Taylor, A.A., et al., Critical review of exposure and effects: implications for setting regulatory health criteria for ingested copper. Environmental Management, 2020. **65**(1): p. 131-159.

165. Royer A, S.T., Copper Toxicity. StatPearls [Internet]. Treasure Island (FL): StatPearls Publishing, 2022.

166. Campbell, A., D. Hamai, and S.C. Bondy, Differential toxicity of aluminum salts in human cell lines of neural origin: implications for neurodegeneration. Neurotoxicology, 2001. **22**(1): p. 63-71.

167. Shaw, C. and L. Tomljenovic, Aluminum in the central nervous system (CNS): toxicity in humans and animals, vaccine adjuvants, and autoimmunity. Immunologic Research, 2013. **56**(2): p. 304-316.

168. Mailloux, R.J., J. Lemire, and V.D. Appanna, Hepatic response to aluminum toxicity: dyslipidemia and liver diseases. Experimental Cell Research, 2011. **317**(16): p. 2231-2238.

169. Frisardi, V., et al., Aluminum in the diet and Alzheimer's disease: from current epidemiology to possible disease-modifying treatment. Journal of Alzheimer's Disease, 2010. **20**(1): p. 17-30.

170. Arias, J.A., et al., Effects of Glomus deserticola inoculation on Prosopis: enhancing chromium and lead uptake and translocation as confirmed by X-ray mapping, ICP-OES and TEM techniques. Environmental and Experimental Botany, 2010. **68**(2): p. 139-148.

171. Tarrago, O. and M. Brown, Case studies in environmental medicine (CSEM) lead toxicity. Agency for Toxic Substances and Disease Registry, 2017.

172. Romero-Estévez, D., et al., Distribution, contents, and health risk assessment of cadmium, lead, and nickel in bananas produced in Ecuador. Foods, 2019. **8**(8): p. 330.

173. Järup, L., Hazards of heavy metal contamination. British Medical Bulletin, 2003. **68**(1): p. 167-182.

174. Anttila, A., et al., Excess lung cancer among workers exposed to lead. Scandinavian Journal of Work, Environment & Health, 1995: p. 460-469.

175. Kumar, S., et al., Effect of automobile exhaust on the distribution of trace elements and its modulation following Fe, Cu, and Zn supplementation. Biological Trace Element Research, 1991. **31**(1): p. 51-62.

176. Wong, O. and F. Harris, Cancer mortality study of employees at lead battery plants and lead smelters, 1947–1995. American Journal of Industrial Medicine, 2000. **38**(3): p. 255-270.

177. Liu, C.-M., et al., Protective role of quercetin against lead-induced inflammatory response in rat kidney through the ROS-mediated MAPKs and NF-κB pathway. Biochimica et Biophysica Acta (BBA)-General Subjects, 2012. **1820**(10): p. 1693-1703.

178. Lundström, N.-G., et al., Cumulative lead exposure in relation to mortality and lung cancer morbidity in a cohort of primary smelter workers. Scandinavian Journal of Work, Environment & Health, 1997: p. 24-30.

179. Russell, R., et al., Dietary reference intakes for vitamin A, vitamin K, arsenic, boron, chromium, copper, iodine, iron, manganese, molybdenum, nickel, silicon, vanadium, and zinc. A report of the panel on micronutrients, subcommittees on upper reference levels of nutrients and of interpretation and uses of dietary reference intakes, and the standing committee on the scientific evaluation of dietary reference intakes food and nutrition board Institute of medicine, 2001: p. 797.

180. Amata, R., et al., Toxicological profile for strontium. 2004.

181. Gupta, D.K. and C. Walther, Behaviour of strontium in plants and the environment. 2018: Springer.

182. Martin, K.R., Silicon: the health benefits of a metalloid. Interrelations between essential metal ions and human diseases, 2013: p. 451-473.

183. Rondanelli, M., et al., Silicon: A neglected micronutrient essential for bone health.

Experimental Biology and Medicine, 2021. **246**(13): p. 1500-1511.

184. Gillette-Guyonnet, S., S. Andrieu, and B. Vellas, The potential influence of silica present in drinking water on Alzheimer's disease and associated disorders. The Journal of Nutrition, Health & Aging, 2007. **11**(2): p. 119.

185. Birchall, J., et al., Acute toxicity of aluminium to fish eliminated in silicon-rich acid waters. Nature, 1989. **338**(6211): p. 146-148.

186. Cuciureanu, R., et al., Assessment of daily aluminum intake by food consumption. Revista Medico-Chirurgicala a Societatii de Medici si Naturalisti din Iasi, 2000. **104**(3): p. 107-112.

187. González-Weller, D., et al., Dietary intake of barium, bismuth, chromium, lithium, and strontium in a Spanish population (Canary Islands, Spain). Food and Chemical Toxicology, 2013. **62**: p. 856-868.

188. Miedico, O., et al., Lead, cadmium and mercury in canned and unprocessed tuna: six-years monitoring survey, comparison with previous studies and recommended tolerable limits. Journal of Food Composition and Analysis, 2020. **94**: p. 103638.

189. Hallett, S., F. Toro, and J.V. Ashurst, Physiology, tidal volume. 2018.

190. Flenady, T., T. Dwyer, and J. Applegarth, Accurate respiratory rates count: So should you! Australasian Emergency Nursing Journal, 2017. **20**(1): p. 45-47.

191. Vanhee, D., et al., Cytokines and cytokine network in silicosis and coal workers' pneumoconiosis. European Respiratory Journal, 1995. **8**(5): p. 834-842.

192. Song, Y., et al., Effects of chemical composition on the lung cell response to coal particles: Implications for coal workers' pneumoconiosis. Respirology, 2022.

193. Zhang, Y., et al., Extracellular histones promote pulmonary fibrosis in patients with coal workers' pneumoconiosis. Journal of Occupational and Environmental Medicine, 2019. **61**(2): p. 89-95.

194. Qi, X.-M., et al., Pneumoconiosis: current status and future prospects. Chinese Medical Journal, 2021. **134**(08): p. 898-907.

195. Ahn, H.S., et al., The Evaluation of IL-8 in the Serum of Pneumoconiotic patients. Tuberculosis and Respiratory Diseases, 1996. **43**(6): p. 945-953.

196. Lee, J.S., J.H. Shin, and B.-S. Choi, Serum levels of IL-8 and ICAM-1 as biomarkers for progressive massive fibrosis in coal workers' pneumoconiosis. Journal of Korean Medical Science, 2015. **30**(2): p. 140-144.

197. Donaldson, K., et al., Contrasting bronchoalveolar leukocyte responses in rats inhaling coal mine dust, quartz, or titanium dioxide: effects of coal rank, airborne mass concentration, and cessation of exposure. Environmental Research, 1990. **52**(1): p. 62-76.

198. Lin, W.-C. and M.B. Fessler, Regulatory mechanisms of neutrophil migration from the circulation to the airspace. Cellular and Molecular Life Sciences, 2021. **78**(9): p. 4095-4124.

199. Rosales, C., Neutrophils at the crossroads of innate and adaptive immunity. Journal of Leukocyte Biology, 2020. **108**(1): p. 377-396.

200. DeLight, N. and H. Sachs, Pneumoconiosis, in StatPearls [Internet]. 2021, StatPearls Publishing.

201. Mlika, M., R. Adigun, and B.S. Bhutta, Silicosis, in StatPearls [Internet]. 2022, StatPearls Publishing.

202. Rivas-Santiago, B.T., et al., Immunological role of epithelial cells of the lung. Revista del Instituto Nacional de Enfermedades Respiratorias, 2005. **18**(4): p. 321-326.

203. Ates, I., et al., Possible effect of gene polymorphisms on the release of TNFα and IL1 cytokines in coal workers' pneumoconiosis. Experimental and Toxicologic Pathology, 2011. **63**(1-2): p. 175-179.

204. Lassalle, P., et al., Abnormal secretion of interleukin-1 and tumor necrosis factor α by alveolar macrophages in coal worker's pneumoconiosis: comparison between simple pneumoconiosis and progressive massive fibrosis. Experimental Lung Research, 1990. **16**(1): p. 73-80.

205. Castranova, V. and V. Vallyathan, Silicosis and coal workers' pneumoconiosis. Environmental Health Perspectives, 2000. **108**(suppl 4): p. 675-684.

206. Borm, P.J., et al., Spontaneous and stimulated release of tumor necrosis factor-alpha(TNF) from blood monocytes of miners with coal workers' pneumoconiosis. American Journal of Respiratory and Critical Care Medicine, 1988. **138**(6): p. 1589-1594.

207. Lee, J.S., et al., Blood levels of IL-Iβ, IL-6, IL-8, TNF-α, and MCP-1 in pneumoconiosis patients exposed to inorganic dusts. Toxicological Research, 2009. **25**(4): p. 217-224.

208. Slavov, E., et al., Correlation between TNF-alpha and IL-12p40-containing cytokines in silicosis. Toxicology and Industrial Health, 2010. **26**(8): p. 479-486.

209. Kim, K.A., et al., Tumor necrosis factor-α gene promoter polymorphism in coal workers' pneumoconiosis. Molecular and Cellular Biochemistry, 2002. **234**(1): p. 205-209.

210. Wang, M., et al., Associations of IL-4, IL-4R, and IL-13 gene polymorphisms in coal workers' pneumoconiosis in China: a case-control study. PLOS One, 2011. **6**(8): p. e22624.

211. Davis, G.S., L.M. Pfeiffer, and D.R. Hemenway, Expansion of interferon-γ–producing lung lymphocytes in mouse silicosis. American Journal of Respiratory Cell and Molecular Biology, 1999. **20**(4): p. 813-824.

212. Ferreira, T.P.T., et al., IL-13 immunotoxin accelerates resolution of lung pathological changes triggered by silica particles in mice. The Journal of Immunology, 2013. **191**(10): p. 5220-5229.

213. Cohen, C., et al., Accelerated silicosis with mixed-dust pneumoconiosis in a hard-metal grinder. Journal of Occupational and Environmental Medicine, 1999: p. 480-485.

214. Hamza, T., J.B. Barnett, and B. Li, Interleukin 12 a key immunoregulatory cytokine in infection applications. International Journal of Molecular Sciences, 2010. **11**(3): p. 789-806.

215. Fahy, J.V. and B.F. Dickey, Airway mucus function and dysfunction. New England Journal of Medicine, 2010. **363**(23): p. 2233-2247.

216. Azam, S. and D.P. Mishra, Effects of particle size, dust concentration and dust-dispersion-air pressure on rock dust inertant requirement for coal dust explosion suppression in underground coal mines. Process Safety and Environmental Protection, 2019. **126**: p. 35-43.

217. Luo, Y., D. Wang, and J. Cheng, Effects of rock dusting in preventing and reducing intensity of coal mine explosions. International Journal of Coal Science & Technology, 2017. **4**(2): p. 102-109.

218. Man, C. and K. Teacoach, How does limestone rock dust prevent coal dust explosions in coal mines? Mining Engineering, 2009. **61**(9): p. 69.

219. Huang, Q. and R. Honaker, Recent trends in rock dust modifications for improved dispersion and coal dust explosion mitigation. Journal of Loss Prevention in the Process Industries, 2016. **41**: p. 121-128.

220. Boyd, P.W., et al., Mesoscale iron enrichment experiments 1993-2005: synthesis and future directions. Science, 2007. **315**(5812): p. 612-617.

221. Rose, A.L. and T.D. Waite, Kinetic model for Fe (II) oxidation in seawater in the absence and presence of natural organic matter. Environmental Science & Technology, 2002. **36**(3): p. 433-444.

222. Gankanda, A. and V.H. Grassian, Nitrate photochemistry on laboratory proxies of mineral dust aerosol: wavelength dependence and action spectra. The Journal of Physical Chemistry C, 2014. **118**(50): p. 29117-29125.

223. Sipilä, M., et al., The role of sulfuric acid in atmospheric nucleation. Science, 2010. **327**(5970): p. 1243-1246.

224. Simpson, W.R., et al., Tropospheric halogen chemistry: Sources, cycling, and impacts. Chemical Reviews, 2015. **115**(10): p. 4035-4062.

225. Borgatta, J., et al., Comparative evaluation of iron leach from different sources of fly ash under atmospherically relevant conditions. Environmental Chemistry, 2016. **13**(5): p. 902-912.

226. Choo, T.K., et al., Mechanisms underpinning the mobilization of iron and magnesium cations from Victorian Brown coal fly ash. Energy & Fuels, 2014. **28**(6): p. 4051-4061.

227. Mozgawa, W., et al., Investigation of the coal fly ashes using IR spectroscopy. Spectrochimica Acta Part A: Molecular and Biomolecular Spectroscopy, 2014. **132**: p. 889-894.

228. Blissett, R. and N. Rowson, A review of the multi-component utilisation of coal fly ash. Fuel, 2012. **97**: p. 1-23.

229. Yao, Z., et al., A comprehensive review on the applications of coal fly ash. Earth-Science Reviews, 2015. **141**: p. 105-121.

230. Toledano, D.S. and V.E. Henrich, Kinetics of SO_2 adsorption on photoexcited α-Fe_2O_3. The Journal of Physical Chemistry B, 2001. **105**(18): p. 3872-3877.

231. Nakata, K. and A. Fujishima, TiO_2 photocatalysis: Design and applications. Journal of Photochemistry and Photobiology C: Photochemistry Reviews, 2012. **13**(3): p. 169-189.

232. Guo, Q., et al., Fundamentals of TiO_2 photocatalysis: concepts, mechanisms, and challenges. Advanced Materials, 2019. **31**(50): p. 1901997.

233. Chen, H., C.E. Nanayakkara, and V.H. Grassian, Titanium dioxide photocatalysis in atmospheric chemistry. Chemical Reviews, 2012. **112**(11): p. 5919-5948.

234. Blesa, M.A., et al., The interaction of metal oxide surfaces with complexing agents dissolved in water. Coordination Chemistry Reviews, 2000. **196**(1): p. 31-63.

235. Xiong, L.-B., et al., Ti??+ in the surface of titanium dioxide: generation, properties and photocatalytic application. Journal of Nanomaterials, 2012. **2012**.

236. Zhang, J. and Y. Nosaka, Mechanism of the OH radical generation in photocatalysis with TiO_2 of different crystalline types. The Journal of Physical Chemistry C, 2014. **118**(20): p. 10824-10832.

CHEMISTRY & PHOTOCHEMISTRY OF AIRBORNE INDUSTRIAL DUST: HUMAN HEALTH & ENVIRONMENTAL IMPLICATIONS

by

Milton Chandra Das